NONLINEAR CONTROL AND APPLICATION OF POWER ELECTRONICS BOOST CONVERTERS

by

Yaser Mohammadian Roshan

M.Sc., Sharif University of Technology, Tehran, Iran, 2008

B.Sc., Ferdowsi University of Mashhad, Mashhad, Iran, 2005

A THESIS SUBMITTED IN PARTIAL FULFILLMENT
OF THE REQUIREMENTS FOR THE DEGREE OF

Doctor of Philosophy

in the
School of Mechatronic Systems Engineering
Faculty of Applied Sciences

SIMON FRASER UNIVERSITY
Fall 2014

APPROVAL

Name:	Yaser Mohammadian Roshan
Degree:	Doctor of Philosophy
Title of Thesis:	Nonlinear Control and Application of Power Electronics Boost Converters
Examining Committee:	Dr. Kevin Oldknow Chair
	Dr. Mehrdad Moallem, Senior Supervisor Professor, Mechatronic Systems Engineering
	Dr. Ahmad Rad, Supervisor Professor, Mechatronic Systems Engineering
	Dr. Farid Golnaraghi, Supervisor Professor, Mechatronic Systems Engineering
	Dr. Jiacheng (Jason) Wang, Internal Examiner, Assistant Professor, Mechatronic Systems Engineering
	Dr. Alireza Bakhshai, External Examiner Associate Professor, Queens University
Date Approved:	July 21, 2014

Partial Copyright Licence

Abstract

In this thesis, we investigate the development of novel control schemes for single and three phase boost converters operated in different modes of conduction. Study is conducted on development of controllers based on the nonlinear dynamic characteristics of the converters and characteristics such as nonminimum phase behavior in boost converters that give rise to control challenges. The control strategies are further applied to certain areas in sustainable energy systems including maximum power point tracking of photovoltaic (PV) panels, load current control of power converters, and energy regenerative suspension in vehicular systems.

To this end, the analytical behavior of a boost converter is studied and utilized to design nonlinear controllers to control the input resistive behavior of the converter. The performance of proposed controllers are verified through simulations and experiments on single stage converters. Finally, the design of a feedback control system for input resistance control of a three-phase bidirectional converter is studied. A sliding mode controller is utilized in an application involving energy regeneration for a mechanical suspension system. A permanent magnet machine and a linear vibration generator are utilized along with the proposed control strategy to achieve regenerative damping in a proof-of-concept suspension system. The simulation and experimental results verify that the proposed controller can successfully provide desired damping for mechanical vibrations while storing the vibration energy in battery.

Index Terms—Boost converters, Continuous conduction mode, Discontinuous conduction mode, Maximum power point tracking, Non-minimum phase systems, Energy regeneration.

To my loving companion, Samaneh.

"An expert is a person who has made all the mistakes that can be made in a very narrow field"

Niels Bohr

Acknowledgments

First and foremost I would like to express my special appreciation and thanks to my advisor Professor Mehrdad Moallem, who have been a tremendous mentor for me. I would like to thank you for encouraging my research and for allowing me to grow as a research scientist. Your advice on both research as well as on my career have been priceless. I would also like to thank my examining committee members, Professor Ahmad Rad, Professor Farid Golnaraghi, Dr. Jason Wang, and Dr. Alireza Bakhshai for serving as my committee members. I would especially like to thank my colleagues Ali Shagerdmootaab, Sepehr Attarchi, Farzad Hamidi, and M. Mehdi Naserimojarad at Motion and Power Electronic Control Laboratory in Simon Fraser University, whom I have had the pleasure to work with.

A special thanks to my family. Words cannot express how grateful I am to my mother-in law, father-in-law, my mother, and father for all of the sacrifices that you've made on my behalf. Your prayer for me was what sustained me thus far. At the end I would like express appreciation to my beloved wife Samaneh Khakshour who was always my support in the moments when there was no one to answer my queries.

Contents

List of Tables

List of Figures

Chapter 1

Introduction

1.1 Motivation of Research

Power converters are electronic systems associated with the conversion of electrical power from one form to another. These systems are used in power levels from milliwatts to megawatts and various forms such as AC to DC converters, DC to DC converters, DC to AC converters, and AC to AC converters [1, 2]. Although, these converters have been investigated extensively, their efficiency and control system robustness may still need improvement. Designing a control system to achieve higher robustness extends the converter useful life, while higher efficiency results in a reduction of environmental impacts because of a reduction of the wasted power and decreasing the cost of energy dissipated in the system [3].

Switched Mode Power Converters (SMPC), are the most common power converters, as they can be controlled easily by controlling the timing of the electronic switches as "On" and "Off". They can also be switched at high frequencies, resulting in high-power efficiency. SMPCs operational concept is simply described as storing energy temporarily in an active element and releasing it to the load at a different voltage [4].

In energy harvesting applications, where energy is recycled from a source in the environment, one of the most common power converters is the boost converter. Boost, or “step-up” converter, is a type of power converter which utilizes an inductor to store the energy from the input in a specific amount of time. It will then connect the input source to the output through the inductor, which results in releasing the stored energy at the same time. As a result, the output voltage will be greater than the input voltage. The nonlinearity of a

boost converter due to the existence of the power switches result in significant difficulties in obtaining the mathematical models in a closed analytical form; hence, making the control problem more challenging. Considering these issues, complex control techniques have been proposed for these converters in literature [5]-[13].

Depending on the power level of the application, switched mode boost converters are often operated in two modes of operation. For low-power applications, these converters are often operated in the Discontinuous Conduction Mode (DCM), whereas the Continuous Conduction Mode (CCM) is utilized in high power applications [14], [15]. In either modes of operation, controlling the current of the source and load is important depending on the application type. For example, controlling the input source current is useful in renewable energy sources and energy harvesting circuits such as Maximum Power Point Tracking (MPPT) of Photovoltaic (PV) modules [16]-[22], or energy regeneration for vehicle suspension systems [23], [24]. Also, load current control is important in various applications such as dimming control of LED drivers [25] and series regulated switching converters used as power loads [26].

1.2 Background and Overview of the Present State of Technology

Operation and control of boost converters have been studied in previous works [5]-[15]. The works on boost converter control are mainly concerned with either controlling its input/output characteristics for specific applications, or overcoming the internal behavior of the converter itself, to extend its controllability and robustness, specifically for load current control. In this thesis we study two aspects in control of boost converters,namely the input behavior of the boost converter and load current control, as discussed in the remainder of this section.

1.2.1 Input Behavior Control of the Boost Converter

In boost power converters, the input current does not inherently follow the input voltage. Hence, Power Factor Correction (PFC) controllers for boost converters have been studied in previous works [27]-[32]. The constant switching frequency PFC converters can be used either in the CCM or DCM based on the power level of the application [33]. In [34], a

single-phase PFC was presented which eliminates the disadvantages of conventional boost-type PFCs such as high switching frequencies, high voltage drop in series path of power flow, switching losses, and high EMI interference. In [35], a pseudo-CCM boost PFC converter was proposed with its corresponding control strategy presented in [33]. A review of active PFC techniques for high-power applications was addressed in [36]. An enhanced current loop controller was discussed in [37] which discusses the design of a boost PFC converters for DCM and CCM operations. Digital control of a boost PFC converters for DCM and CCM operations was addressed in [38]. A simple digital current control scheme was proposed in [39] using input current shaping to achieve fast response.

The above works have mainly discussed boost power converters based on the assumption of using sinusoidal inputs and currents with known input frequencies. However, to achieve maximum power absorption in cases involving random power sources such as wind or wave, with time varying input amplitude and frequency, enforcing a resistive behavior at the input of the boost converter regardless of the input waveform is desirable. To this end, a new scheme for modeling the converter input resistance was presented in [40]-[42], in which boost converters, operating in DCM and CCM, were studied accompanied by the control strategy, respectively.

However, based on the dynamics of the application, and the source which is connected to the boost converter, the control technique may have an impact on the quality of the power transfer. Therefore, in this work, two specific applications have been chosen in the area of renewable energy sources and energy harvesting, to demonstrate the effectiveness of the developed control approaches.

Maximum Power Estimation and Tracking in Photovoltaic (PV) Modules

One of the common applications of boost power converter is in photovoltaic systems, where the amount of power generated through a module is highly dependent on the characteristics of the power converter circuit. Therefore, controlling the input characteristics of the power converter (boost converter in this case), plays an important role in harvesting the maximum amount of power from the module.

The efficiency of energy conversion of a PV module depends mainly on environmental conditions. In particular, the Power-Voltage (P-V) characteristic of a PV module is highly nonlinear and time-varying, which changes with atmospheric conditions such as radiance and temperature. Hence, MPPT controllers are required in PV systems to continuously tune the

system operating point so that it extracts maximum power from the module [43].

Several MPPT techniques have been developed in the literature for MPPT of a single PV module as discussed in [44]. The algorithms for these MPPT methods can be divided into two groups [45]. The first group of methods is based on voltage feedback in which a predetermined reference voltage is compared with the PV module voltage in a feedback loop. The feedback methods enable one to choose a desirable operating point for unknown or varying load conditions. The controllers also need to avoid energy inefficiencies such that the reference voltage is able to change due to varying environmental conditions.

For instance, in [46] the authors propose a Radial Basis Function Network (RBFN) to adjust the reference voltage of a MPPT control system. In this paper, a stand-alone hybrid power system is addressed which consists of solar power, wind power, and a diesel engine. This system includes an intelligent power controller to acheive fast and stable response for power control. This controller consists of a RBFN and an improved Elman Neural Network (ENN) for MPPT. RBFN is responsible for MPPT of the solar system while ENN controls the pitch angle of wind turbine. Other examples using this method can be found in [47] and [48], where the voltage at MPP is approximated as a fraction of the open circuit voltage of the module as

$$V_{MPP} \approx k_1 V_{OC} \tag{1.1}$$

where k_1 is a constant of proportionality. The value of k_1 is usually estimated based on different factors reported between 0.71 and 0.78. This value is affected by irradiance and temperature levels. In these methods, which are called *Fractional Open-Circuit Voltage* [44], the value of V_{OC} is measured periodically by momentarily disconnecting the power converter from the module. The temporary loss of power which is the result of this method of measurement has been compensated in [47] by using pilot cells. The above concept has been used in [49] to design an MPPT controller based on an estimation of the value of k_1.

The method of fractional open-circuit voltage has also been extended to *Fractional Short-Circuit Current* to estimate the current at MPP with a fraction of PV module short circuit current [50]. Using this estimation, the PV module current can be controlled to achieve the desired current as follows

$$I_{MPP} \approx k_2 I_{SC} \tag{1.2}$$

where k_2 is a constant of proportionality. As before, the value of k_2 should also be determined beforehand experimentally which is generally estimated between 0.78 and 0.92.

The second group of methods are power feedback methods based on calculating the PV module generated power by sensing voltage and/or current and utilizing them for tracking the MPP. Among these algorithms, *Hill-Climbing/Perturb and Observe (P&O)* and *Incremental Conductance (IncCond)* are the most popular algorithms which have been utilized in previous works (see e.g., [51] and [44]). The P&O technique is based on injecting high-frequency small-amplitude perturbations in the system to detect the direction of power variation [52]. In the hill-climbing method the perturbation is applied in the duty ratio of the power converter, while in the P&O method the perturbation is in the operating voltage of PV module. As perturbing the duty ratio of power converter will eventually perturb the PV module voltage, the fundamental concept of these two methods are the same. The P-V curve of the PV module in Figure 1.1 demonstrates basics of these two methods. In the voltage-power curve P_1, if an increase in voltage decreases the power of the module (e.g., moving from A to B), the perturbation should be reversed. Otherwise, with an increases in power (e.g., moving from B to A), the perturbation should be kept the same to reach MPP. This concept can be extended for reducing the voltage as well. Figure 1.1 also illustrates that these methods can fail under rapidly changing atmospheric conditions [44]. If during the transition from A to B, the irradiance faces a rapid change, which results in changing the curve to P_2, the operating point will move to C. As the power is increasing, the perturbation will be kept the same, while the operating point is diverging from the MPP.

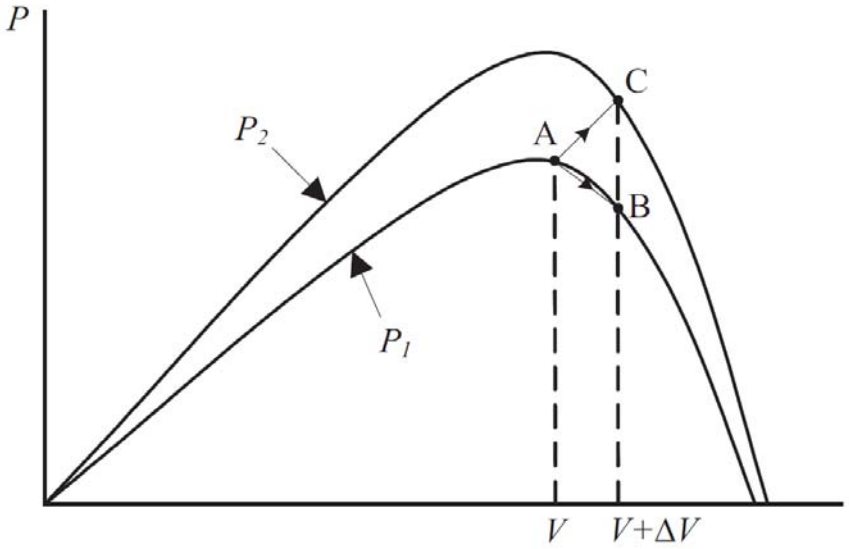

Figure 1.1: Hill-climbing and P&O methods [44].

In these methods, after a transient time the operating point will oscillate around the MPP. These oscillations can be avoided by reducing the step size of changing the perturbations. However, reducing the step size results in reducing the MPPT speed. This conflict has been addressed in the literature (e.g., [53]) by using variable step sizes.

The Incremental Conductance technique has been widely used due to its ease of implementation and high tracking efficiency. This method is based on the fact that the instantaneous conductance of a PV module with a negative sign is equal to the incremental conductance of it at MPP [54]. The above method can be demonstrated by considering the following

$$\frac{dP}{dV} = \frac{d(IV)}{dV} = I + V\frac{dI}{dV} \tag{1.3}$$

Since at the MPP, the variations of the power with respect to voltage, $\frac{dP}{dV}$, is equal to zero, (1.3) can be written as

$$\frac{\Delta V}{\Delta I} = -\frac{V}{I} \tag{1.4}$$

where $\frac{dI}{dV}$ in (1.3) is approximated by $\frac{\Delta I}{\Delta V}$.

In this method, the MPP can be tracked by comparing the instantaneous and incremental conductances of the module, and changing the reference voltage V_{ref}, where the reference voltage is the desired voltage of the PV module. This algorithm has been demonstrated in Figure 1.2 [44].

In the IncCond method, when the MPP is reached, there will be no more oscillations around that point. Thus, this method is more advantageous because of the elimination of the continuous oscillation around the optimal operating point [55]. However, a major drawback is the difficulty in choosing the step size of the reference voltage, which has been addressed in the literature (e.g., [56]).

Beside the conventional methods for MPPT control, intelligent control algorithms have been introduced to this area, such as neural networks controllers [46], [57]. The drawback of using neural networks is their need to be trained beforehand. Also, their functionality are degraded over time if they are not periodically trained.

Fuzzy logics has been used for MPPT control because of their ease of implementation using microcontrollers [58]. These controllers demonstrate well performance under rapidly changing conditions.

In this research, an identification method for MPP is proposed, followed by a novel MPPT approach, in which the MPP is achieved with a high tracking efficiency.

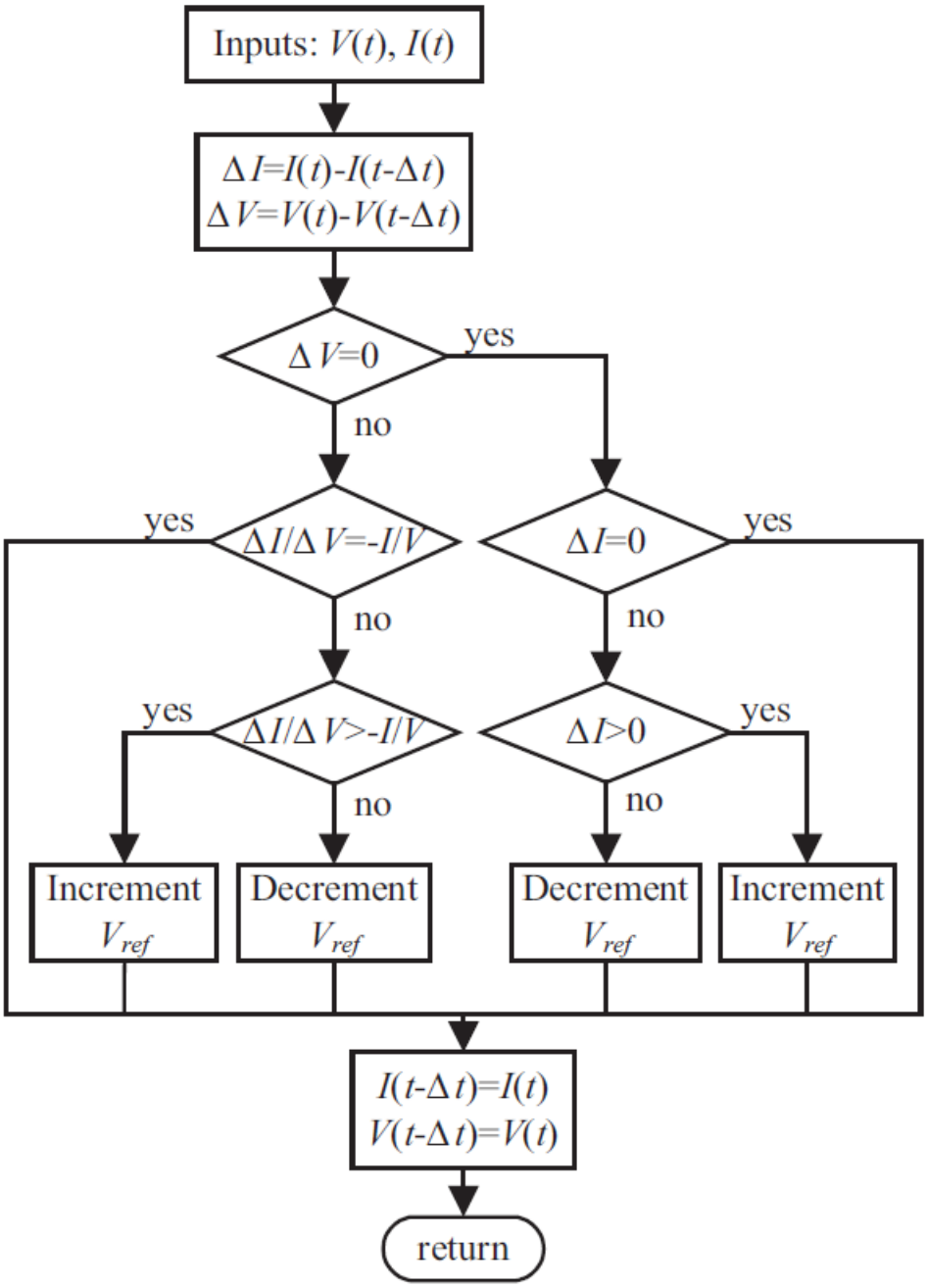

Figure 1.2: Incremental conductance method algorithm [44].

Regenerative Suspension

Another recent application of the boost power converter is in regenerative suspension systems. The idea is to create a damping effect by storing the wasted vibration energy of vehicle suspension system. This effect can be created by proper control for the input characteristics of the power converter.

The suspension system installed between a vehicle's chassis and wheels is a dynamic system comprised of spring and dampers to effectively attenuate the transfer of road vibrations to the vehicle body. The system provides *ride comfort*, while keeping the wheel in contact with road at all times, i.e. *road handling* [59]. Two main components of these systems are springs and dampers, which have the responsibility of absorbing and releasing the energy and dissipating the vibration energy, respectively [60]. Suspension systems are categorized as passive, active, and semi-active systems [61]. In the passive suspension, the damping coefficient is constant, with its magnitude obtained by a trade-off between ride comfort and road handling. In active suspension, an actuator is used to exert opposite forces and overcome the vibrations. However, active suspension has disadvantages such as higher power consumption and cost, larger equipment, and the need for complex controllers [62]. Another drawback of the active suspension systems is the possibility of becoming unstable if the controller fails [63]. On the contrary, the semi-active approach enables the suspension system to change its damping coefficient continuously, i.e. *Continuously Varying Damper (CVD)* [64], due to its flexible structure, while remaining stable by acting as a pure passive damper if the controller fails.

Among proposed approaches for designing semi-active suspension systems such as skyhook, ground-hook, and hybrid strategies, skyhook control is highly utilized, because of its ease of realization and better performance [65]. Existing works in realization of skyhook suspension systems can be categorized as methods which dissipate the suppressed energy into heat, and those which recycle the damping energy intro electric charge to be stored in a battery, i.e. *regenerative systems* [66]. In the first category, hydraulic and Magneto-Rheological (MR) dampers are the most common choices [64, 67, 68]. The later one has advantages such as small size and fast response time, but it is more complex from the control perspective. Thus, regenerative systems can be used to control the damping coefficient of the system while storing the vibration energy by utilizing an electrical circuitry. The proposed methods

for regenerative systems, mostly include the usage of linear or rotary electromagnetic mechanisms in the energy conversion stage. Compared to the rotary machines, tubular linear machines can generate more force with better linear accuracy, while avoiding the use of a linear-to-rotary motion conversion system [69]- [71]. However, in high-power applications, where the space and cost is important, the choice of rotary machines is more justified [72].

Most of the semi-active suspension systems reported in the literature emphasize on design considerations for developing the linear machine for specific applications [69]-[70], or utilize simple control strategies for a single-phase boost converter [69], [71]. However, in vehicular systems, the amount of damping forces are relatively high; therefore, the need for a three-phase converter design and control has yet to be satisfied for this types of applications. In [72], the control strategy for a three-phase boost converter applied to a regenerative suspension system is discussed, in which the converter is operated in DCM. However, as operating in CCM enables the transfer of higher powers from the shock-absorber to the storage system, designing a proper technique to work in CCM is very important. This system is analyzed in this research, and a control strategy is designed to overcome the mentioned problems.

1.2.2 Load Current Control of the Boost Converter

In DCM operation, the boost converter system is minimum-phase due to the non-existence of Right Half-Plane (RHP) zeros in the transfer function from the input duty cycle to the output voltage/current. Consequently, the feedback system is less prone to instability issues when compared to DCM operation where the boost converter is non-minimum phase. In high-power applications, a boost converter may be operated in CCM. However, due to its Non-Minimum Phase (NMP) characteristic, regulation of the output load current and voltage pose control challenges [73]-[79]. In [73], the NMP behavior of a boost converter facing uncertainties and sudden changes in operating conditions was studied. It is well known that feedback control of non-minimum phase systems is challenging due to the instability of the system internal dynamics [80], [81]. There have been continuous efforts to design novel control strategies to improve performance of boost power converters [82]. Previous works have studied cascade control [73], H_∞ control [83], interleaved converters [84], synergetic control [85], and passivity-based control [76]. The above approaches are generally complex in hardware and control algorithms. For instance, additional inputs have to be introduced as in [84], or complex controllers may be required [83], which in turn may pose stability and

robustness issues. Moreover, most of the previous works have utilized linear or piece-wise linear models for the boost converter [73, 82], which may affect the accuracy and performance of the control system.

In this research, the concept of output re-definition has been utilized, which involves defining a new minimum-phase output that is reasonably close to the desired load current; yet resulting in a minimum-phase system. Controlling the re-defined output would be less difficult due to the minimum phase characteristic of the system and would lead to a more robust controller. The aforementioned method was originally presented in [74] and has been utilized in under-actuated mechanical systems including tip-position tracking control of structurally flexible robots [86], end-point force control of a flexible arm [87], and attitude control of flexible spacecrafts [88]. Due to under-actuation, all the above systems exhibit unstable internal dynamics and non-minimum phase characteristics. A major challenge in utilizing the method of output re-definition is finding a proper output. To this end, extension of the output re-definition concept to a boost power electronics converter is the subject of the present work. Achieving a minimum-phase characteristic would improve the feedback loop stability and robustness at the cost of introducing larger tracking errors, which can be alleviated by a proper choice of the re-defined output.

1.3 Summary of Contributions and Outline of This Dissertation

Controlling the boost converter input/output behavior is related to the type of application in hand. Therefore, for each specific application, the control strategy for the boost converter should be modified to enhance the performance of the overall system. To achieve proper performance and alleviate nonlinear and/or non-minimum phase issues of the boost converter, the idea presented in this dissertation is to analyze boost converter behavior in different modes of operation, and design a control strategy for each mode through nonlinear feedback control approaches. In this regard, the contributions of this thesis are summarized as follows:

1.3.1 Chapter 2: Input Behavior Control of Boost Converters

This chapter lays the groundwork upon which the rest of the research was founded. First, the boost converter circuit and its different modes of operation are introduced. The analytical closed-form solutions of the boost converter are discussed in Discontinuous Conduction Mode (DCM) and Continuous Conduction Mode (CCM). The analytical expression for the converter model is addressed based on the complete mathematical model of the converter, averaged model, and simplified model. Simulation results in this section demonstrate the accuracy of the models, specially while operating in CCM. A nonlinear feedback control approach is proposed to control the input behavior of the converter either in DCM or CCM modes of operation. Simulation results are presented to demonstrate the effectiveness of the proposed control strategies. The results of this chapter are used in Chapter 3 as a control framework for tracking the maximum power point of photovoltaic modules. The outcomes of research presented in this chapter were published in [89].

1.3.2 Chapter 3: MPPT of PV Modules Utilizing Boost Converter Input Control

The modeling approach and controller design strategy developed in Chapter 2, is used in this chapter to perform maximum power point tracking for photovoltaic modules. First, the electrical characteristics of the PV module is presented. Then, the effect of controlling the input behavior of the boost converter on MPPT is analyzed. The control strategy is verified by simulation of a novel modified incremental conductance control method. In order to perform MPPT control, the maximum power point identification is very important. Therefore, two real-time identification methods are proposed in this chapter utilizing the knowledge of PV operating condition. The first one utilizes an approximation method; while the second one utilizes Lambert W-Function to find the MPP of a PV module under variable operating conditions. The results of the identification methods along with the proposed controller are presented in this chapter along with simulation and experimental evaluations. The outcomes of research presented in this chapter were published in [41], [49], [55], and [90].

1.3.3 Chapter 4: Non-Minimum Phase Load Current Control in a Boost Converter

Due to the non-minimum phase behavior of the boost converter operating in CCM, output control of the boost converter is a challenging issue from a control theory perspective. In this chapter load current control is addressed. A nonlinear feedback-based controller is developed to alleviate the non-minimum phase problem by using the concept of output-redefinition. Another controller is proposed for the converter to operate in DCM. The two controllers are then combined. The resulting system contains a global controller to be used as load current controller for boost converters, regardless of their mode of operation. Simulation and experimental results of the proposed strategy demonstrate the effectiveness of the controller in terms of speed and accuracy. The outcomes of the research presented in this chapter were published in [40] and [42].

1.3.4 Chapter 5: Three-Phase Bidirectional Converter in Regenerative Suspension

In this chapter, the dynamics 3-phase bidirectional converter is analyzed. A sliding mode controller is proposed to shape the input waveforms of the converter based on desired characteristics of regenerative suspension systems. To this end, the control system is simulated when used with a linear permanent magnet machine to demonstrate its performance in damping vibrations while storing the vibration energy into a battery. The power electronic system and controller are implemented by utilizing a rotary permanent magnet machine through a two-leg linear to rotary conversion mechanism to verify the performance of the system. Experimental results demonstrate the accuracy of the proposed control system to act as a variable resistor; hence, variable damper, for the regenerative suspension system. The outcomes of research presented in this chapter are submitted to [91] and [92].

1.3.5 Chapter 6: Summary, Conclusions, and Suggestions for Future Works

The research work accomplished in this thesis is summarized in this chapter. Based on the theoretical, simulation, and experimental studies, general conclusions concerning the outcome of this thesis are provided along with suggestions for future work.

Chapter 2

Input Behavior Control of Boost Converters

In this chapter, the analytical closed-form solution of a boost type DC-DC switching power converter is analyzed in continuous and discontinuous conduction modes of operation. The models are simplified using circuit averaging technique. The solutions are then verified by simulating a boost converter circuit. Using the simulation results the accuracy of the simplified models are evaluated. In section 2.4, controlling the input behavior of the boost converter in DCM and CCM is addressed. The developed controllers are evaluated by simulation results in this section. The proposed controllers are used in Chapter 3 to track the maximum power point of a single PV module.

2.1 Boost Converter Circuit

Figure 2.1 illustrates the general structure of a DC/DC boost converter. Here it is assumed that the converter is connected to a constant voltage load with voltage v_b (e.g., a battery). Thus, the output voltage is considered constant during a switching period. Figure 2.2 depicts a simplified model of a lead-acid battery [94], which includes the constant voltage source v_B, and an internal resistance r. Based on the value of the duty cycle d, and the ratio of input and output voltages of the converter, i.e. v_i and v_b, respectively, the converter can operate in either Discontinuous Conduction Mode (DCM) or Continuous Conduction Mode (CCM)

as follows [95]

$$\begin{aligned} d &< 1 - \frac{v_i}{v_b} && DCM \\ d &\geq 1 - \frac{v_i}{v_b} && CCM \end{aligned} \tag{2.1}$$

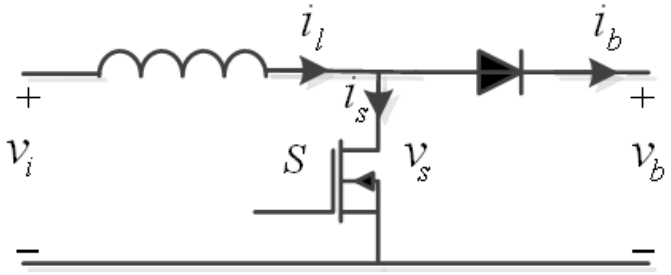

Figure 2.1: Boost converter circuit.

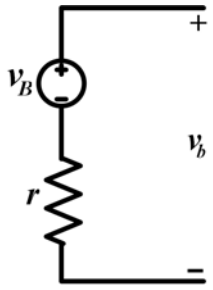

Figure 2.2: Battery simplified model.

In both modes, the inductor is charged during the switch ON period. During the switch OFF period, the inductor is discharged in the battery through the diode. In DCM, the inductor will be discharged completely before the start of the next switching cycle, while in CCM, the inductor current does not have adequate time to discharge completely in the battery. The inductor current and voltage and the output current of the converter in both modes are depicted in Figures 2.3a and 2.3b, respectively.

2.2 Analytical Closed-Form Solution of Boost Converter

In this section, the closed-form solution of the boost converter equations is derived. First, the boost converter response will be analyzed with the battery internal resistance, and then

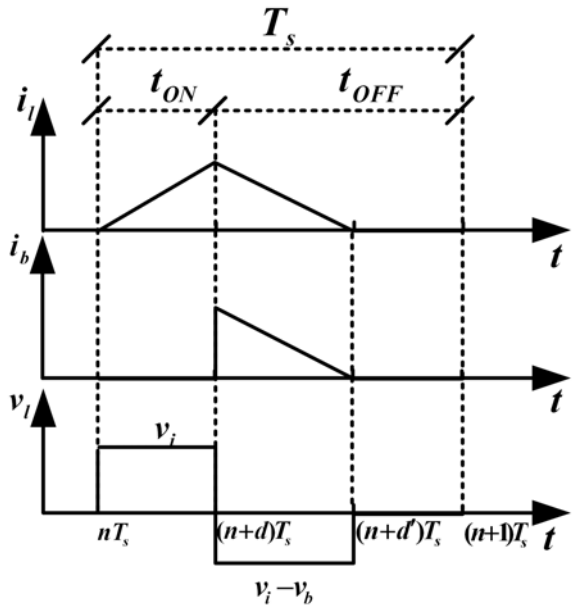

(a)

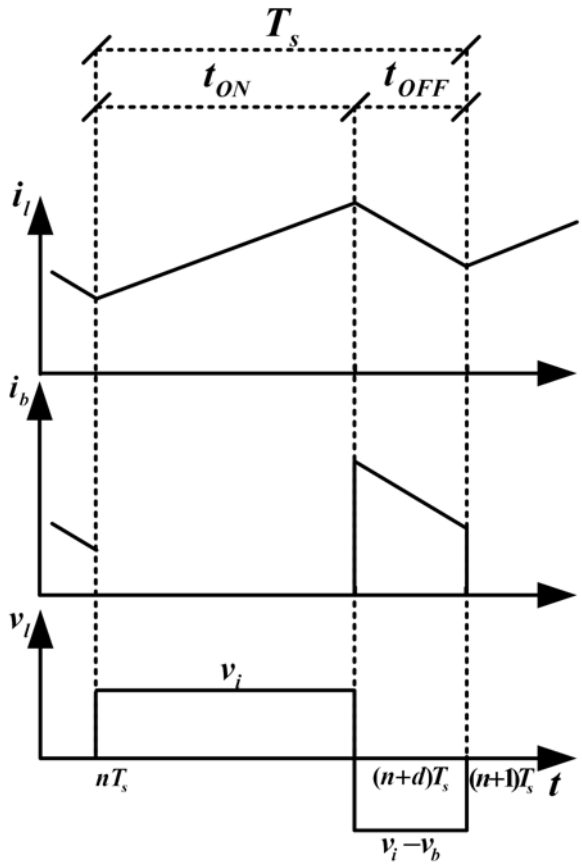

(b)

Figure 2.3: Boost converter signals (a) DCM mode. (b) CCM mode.

the model will be simplified by considering a very small resistance. The solution will be analyzed in both DCM and CCM modes. The average model of the system is then derived to control the input behavior of the converter.

To derive the analytical closed-form solution of the converter, following [93] a method based on Laplace and Z transforms is used. From the analysis of the boost converter during ON and OFF time, the following differential equation can obtained.

$$v_i = L\frac{di_l}{dt} + f(t)(v_b + ri_l) \tag{2.2}$$

where

$$f(t) = \sum_{n=0}^{\infty} [u(t - t_{ON} - nT_s) - u(t - T_s - nT_s)] \tag{2.3}$$

in which $u(t)$ is the step function. To solve (2.2), the following change of variables is performed

$$t = (n + m)T_s, n = 0, 1, ..., 0 \leq m < 1 \tag{2.4}$$

where n is a discrete variable corresponding to the switching periods passed, and m is a continuous variable ranging between 0 and 1. With this change of variables, the mathematical model of the system can be defined as follows

$$\frac{di_{l,n}}{dm} = \begin{cases} \frac{T_s}{L}v_{i,n}, & 0 \leq m < \frac{t_{ON}}{T_s} \\ \frac{T_s}{L}(v_{i,n} - v_b) - \frac{rT_s}{L}i_l, & \frac{t_{ON}}{T_s} \leq m < 1 \end{cases} \tag{2.5}$$

where $i_{l,n}(0) = i_{l0,n}$, and $i_{l,n}(\frac{t_{ON}}{T_s}) = i_{l1,n}$, and $v_{i,n}$ is the input voltage in switching cycle n, which is assumed to be constant in each switching cycle.

Using the Laplace transform method, (2.5) can be solved as follows

$$i_{l,n}(m) = \begin{cases} i_{l0,n}u(m) + \frac{T_s v_{i,n} m}{L}, & 0 \leq m < \frac{t_{ON}}{T_s} \\ \left(i_{l1,n} - \frac{v_{i,n} - v_b}{r}\right) e^{-\frac{r(mT_s - t_{ON})}{L}} + \frac{v_{i,n} - v_b}{r}, & \frac{t_{ON}}{T_s} \leq m < 1 \end{cases} \tag{2.6}$$

Given that the inductor current is continuous, the sequence $i_{l1,n}$ can be evaluated from the sequence $i_{l0,n}$ as follows

$$\lim_{m \to (\frac{t_{ON}}{T_s})^-} i_{l,n}(m) = \lim_{m \to (\frac{t_{ON}}{T_s})^+} i_{l,n}(m) \Rightarrow i_{l1,n} = i_{l0,n} + \frac{t_{ON} v_{i,n}}{L} \tag{2.7}$$

Equations (2.6) and (2.7) contain the unknown sequence of the initial conditions for each period of switching. Analytical closed form expressions of these sequences can be obtained by using the z-transform method. Since $i_l(t)$ is a continuous function, the following relationship have to be satisfied at the switching instants $t = nT_s$:

$$\begin{aligned}
&\lim_{m\to 1^-} i_{l,n}(m) = \lim_{m\to 0^+} i_{l,n+1}(m) \\
&\Rightarrow i_{l0,n+1} = \left(i_{l1,n} - \frac{v_{i,n} - v_b}{r}\right) e^{-\frac{r}{L}(T_s - t_{ON})} + \frac{v_{i,n} - v_b}{r} \\
&\Rightarrow i_{l0,n+1} = \left(i_{l0,n} + \frac{t_{ON} v_{i,n}}{L} - \frac{v_{i,n} - v_b}{r}\right) e^{-\frac{r}{L} t_{OFF}} + \frac{v_{i,n} - v_b}{r} \qquad (2.8)
\end{aligned}$$

Equation (2.8) can be solved by means of the z-transform. Using $\mathcal{Z}\{i_{l0,n}\} = I_{l0}(z)$, and $\mathcal{Z}\{i_{l0,n+1}\} = zI_{l0}(z) - zi_{l0,0}$, we can re-write (2.8) as

$$\begin{aligned}
I_{l0}(z) &= \frac{z}{z - e^{-\frac{r}{L} t_{OFF}}} i_{l0,0} \\
&+ \frac{z}{(z-1)\left(z - e^{-\frac{r}{L} t_{OFF}}\right)} \\
&\quad \left[\left(\frac{v_{i,n} t_{ON}}{L} - \frac{v_{i,n} - v_b}{r}\right) e^{-\frac{r}{L} t_{OFF}} + \frac{v_{i,n} - v_b}{r}\right] \qquad (2.9)
\end{aligned}$$

Using (2.9), the steady state values of the unknown sequences can be found using the final value theorem of the z-transform as

$$\begin{aligned}
i_{l0,ss} &= \lim_{z\to 1}(z-1) I_{l0}(z) \\
&= \left(\frac{1}{1 - e^{-\frac{r}{L} t_{OFF}}} - 1\right) \frac{v_{i,n} t_{ON}}{L} + \frac{v_{i,n} - v_b}{r} \qquad (2.10)
\end{aligned}$$

Hence

$$\begin{aligned}
I_{l0}(z) &= \frac{z}{z - e^{-\frac{r}{L} t_{OFF}}} i_{l0,0} \\
&+ \frac{z}{(z-1)\left(z - e^{-\frac{r}{L} t_{OFF}}\right)} \left(1 - e^{-\frac{r}{L} t_{OFF}}\right) i_{l0,ss} \qquad (2.11)
\end{aligned}$$

The complete solution can be found by using the inverse z-transform of (2.11), i.e.,

$$i_{l0,n} = e^{-\frac{r}{L} t_{OFF} n} i_{l0,0} + i_{l0,ss}\left(1 - e^{-\frac{r}{L} t_{OFF} n}\right) u(n-1) \qquad (2.12)$$

The final closed-form solution of the boost converter can be written by substituting (2.12) and (2.7) into (2.6) as follows

$$i_{l,n}(m)=\begin{cases} e^{-\frac{r}{L}t_{OFF}{}^n}i_{l0,0}+i_{l0,ss}\left(1-e^{-\frac{r}{L}t_{OFF}{}^n}\right)u(n-1)u(m) & \\ \quad +\frac{T_s v_{i,n}m}{L}, & 0\le m<\frac{t_{ON}}{T_s} \\ \left(e^{-\frac{r}{L}t_{OFF}{}^n}i_{l0,0}+i_{l0,ss}\left(1-e^{-\frac{r}{L}t_{OFF}{}^n}\right)u(n-1)\right. & \\ \quad \left.+\frac{t_{ON}v_{i,n}}{L}-\frac{v_{i,n}-v_b}{r}\right)e^{-\frac{r(mT_s-t_{ON})}{L}}+\frac{v_{i,n}-v_b}{r}, & \frac{t_{ON}}{T_s}\le m<1 \end{cases} \tag{2.13}$$

2.2.1 Mathematical Model for Boost Converter Operating in DCM

The relations in section 2.2 describe the analytical closed-form solution of a boost converter regardless of the operating area. When the converter operates in DCM, the inductor current falls to zero before the switch is turned ON again. From a mathematical point of view, this means $i_{l0,n}=0,\forall n$. Therefore, the inductor current in DCM can be written as a special case of (2.13) as

$$i_{l,n}(m)=\begin{cases} \frac{T_s v_{i,n}m}{L}, & 0\le m<\frac{t_{ON}}{T_s} \\ \left(\frac{t_{ON}v_{i,n}}{L}-\frac{v_{i,n}-v_b}{r}\right)e^{-\frac{r(mT_s-t_{ON})}{L}}+\frac{v_{i,n}-v_b}{r}, & \frac{t_{ON}}{T_s}\le m<\frac{\mu}{T_s} \\ 0, & \frac{\mu}{T_s}\le m<1 \end{cases} \tag{2.14}$$

where μ is the time where the inductor current reaches zero. The value of μ can be evaluated from equating the second part of (2.14) to zero. If the value of r has been assumed negligible with respect to the other terms, and using the L'Hopital's rule, the value of μ can be found from

$$\mu=\frac{v_b t_{ON}}{(v_b-v_{i,n})} \tag{2.15}$$

Equation (2.14) can be re-written in the following simplified form.

$$i_{l,n}(m)=\begin{cases} \frac{T_s v_{i,n}m}{L}, & 0\le m<\frac{t_{ON}}{T_s} \\ \frac{t_{ON}v_{i,n}}{L}+\frac{v_{i,n}-v_b}{L}(mT_s-t_{ON}), & \frac{t_{ON}}{T_s}\le m<\mu \\ 0, & \mu\le m<1 \end{cases} \tag{2.16}$$

In DCM mode, the inductor current will reach zero at the end of each switching cycle. Therefore, the inductor current changes in each cycle is zero. However, using the averaging method [95], [96], the average value of the inductor current can be derived as follows

$$<i_l>_n=\frac{t_{ON}^2}{2LT_s}\left(\frac{v_b v_{i,n}}{v_b-v_{i,n}}\right) \tag{2.17}$$

Equation (2.17) indicates that the boost converter operated in DCM exhibits the following nonlinear behavior.

$$R_{DCM_n} = \frac{v_{i,n}}{< i_l >_n} = \frac{2LT_s}{t_{ON}^2}\left(1 - \frac{v_{i,n}}{v_b}\right) \tag{2.18}$$

From (2.18), the resistance varies based upon the operating condition and parameters of the converter and switching characteristics. This resistance is related to the power transferred through the converter to the DC link, which is referred to as *effective resistor* [96]. Using a proper controller, one can regulate the effective resistance to a desired value, for example to achieve maximum power transfer. This concept is utilized in the following sections for maximum power point tracking of solar modules.

2.2.2 Average Model for Boost Converter Operating In CCM

An averaging method is used [96] to find the averaged values of $\frac{di_l}{dt}$ and the inductor current i_l, in one switching cycle. The average variations in the inductor current is given by

$$\begin{aligned} \frac{di_l}{dt}|_n &= \frac{i_{l0,n+1} - i_{l0,n}}{T_s} \\ &= \frac{1}{T_s}\left(\left(i_{l0,n} + \frac{t_{ON}v_{i,n}}{L} - \frac{v_{i,n} - v_b}{r}\right)e^{-\frac{r}{L}t_{OFF}} + \frac{v_{i,n} - v_b}{r} - i_{l0,n}\right) \end{aligned} \tag{2.19}$$

Also, the average value of the inductor current is given by

$$\begin{aligned} < i_l >_n &= \frac{1}{2T_s}\left(i_{l0,n} + i_{l0,n}t_{ON} + \frac{t_{ON}v_{i,n}}{L}T_s\right. \\ &+ \left. t_{OFF}\left(i_{l0,n} + \frac{t_{ON}v_{i,n}}{L} - \frac{v_{i,n} - v_b}{r}\right)e^{-\frac{r}{L}t_{OFF}} + t_{OFF}\left(\frac{v_{i,n} - v_b}{r}\right)\right) \end{aligned} \tag{2.20}$$

where $< . >$ denotes the average value of the signal in one switching cycle, and n denotes the number of switching period.

2.2.3 Simplified Analytic Model for Boost Converter Working in CCM

Assuming that the internal resistance of the battery is close to zero, (2.21) can be written in each sampling period as follows

$$i_{l,n}(m) = \begin{cases} \frac{T_s v_{i,n} m}{L} + \frac{n v_{i,n} T_s}{L} - \frac{n v_b}{L}t_{OFF}, & 0 \le m < \frac{t_{ON}}{T_s} \\ \frac{v_{i,n} - v_b}{L}(mT_s - t_{ON}) + \frac{t_{ON}v_{i,n}}{L} + \frac{n v_{i,n} T_s}{L} - \frac{n v_b}{L}t_{OFF}, & \frac{t_{ON}}{T_s} \le m < 1 \end{cases} \tag{2.21}$$

Note that in deriving (2.21), the input voltage is considered to be constant, i.e., $v_{i,n} = v_{i,n-1}$. If the input voltage is a multi-frequency signal (the frequencies should be much less than the switching frequency so that the input voltage can be considered constant in one switching cycle), the term $nv_{i,n}$ will change to $\sum_{k=0}^{n-1} v_{i,k}$. For calculating the average values of the inductor current, one can use the L'Hopital's rule and calculate the limits of (2.19) and (2.20) when r approaches zero. Using this rule, and by performing some algebraic manipulations, the average value of the inductor current deviations and the inductor current itself are as follows

$$\frac{di_l}{dt}|_n = \frac{v_{i,n}}{L} - \frac{v_b t_{OFF}}{LT_s} \tag{2.22}$$

$$< i_l >_n = i_{l0,n} + \frac{T_s}{2L}\left(v_{i,n} - \frac{t_{OFF}^2}{T_s^2} v_b\right) \tag{2.23}$$

2.3 Simulation of the Boost Converter Operating in CCM Mode

In the previous section, the analytical closed-form solution of a boost converter operating under either DCM or CCM was derived. The results of section 2.2.1 were simulated and confirmed in [97]. In this section, the boost converter operating in CCM is simulated and the results are compared with the closed-form solution.

A Simulink model of the proposed control system was developed using the SimPowerSystems toolbox in the Matlab/Simulink environment. The data for the simulated circuit are chosen as follows:

- Inductor, L, $0.1mH$,
- Battery voltage, v_B, $7V$,
- Battery Internal Resistance, r, 0.07Ω,
- Switching Frequency, f_s, $2KHz$.

To verify the accuracy of CCM analytical closed-form solution, a boost converter was simulated along with an input voltage of $v_i = 2 + sin(100\pi t)$. Figures 2.4a and 2.4b present waveforms for i_l and $\frac{di_l}{dt}$, respectively. In these figures, the dashed line demonstrates the value which is obtained from the averaging method, i.e. (2.19) and (2.20). The solid line demonstrates the results of the simulation. These figures indicate that there is a good match

between the results obtained using the averaging method and the actual system. Also, Fig. 2.4a includes the magnified inductor current, with the dashed line representing the average value of the solid line.

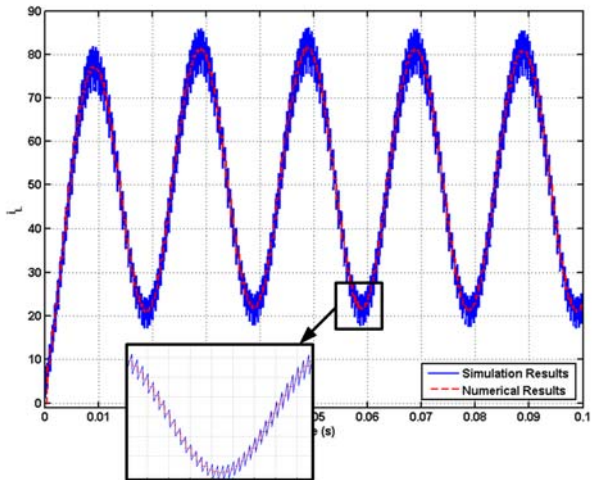

(a)

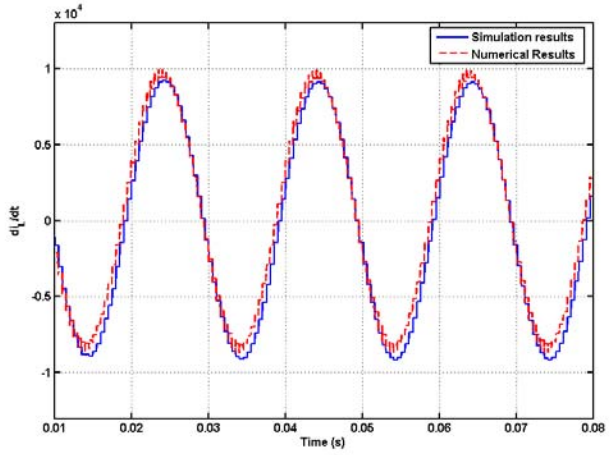

(b)

Figure 2.4: Results of $v_i = 2 + sin(100\pi t)$ (a) Inductor current. (b) Inductor current variations.

Figure 2.5 represents the inductor current for the case of constant input voltage $v_i = 2V$. This figure also illustrates a close match between the results of the averaging method simulation (dashed line) and numerical simulation of the circuit (solid line) when the input

is a constant voltage.

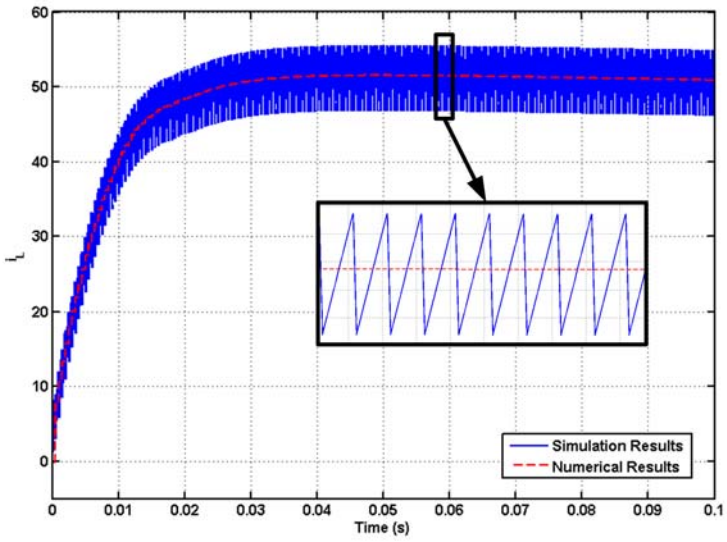

Figure 2.5: Inductor current ($v_i = 2V$).

2.4 Input Behavior Control for Boost Converter

Input behavior of the boost DC/DC converter in both DCM and CCM are described in (2.18) and (2.22), respectively. In this section, two controllers are designed to control the boost converter input behavior based on the above operation modes.

2.4.1 Boost Converter Operating in DCM

In [97], an input resistance controller for the boost converter was presented for operation in DCM. Figure 2.6, depicts the proposed controller blocks to achieve the desired input resistance. In this system, the duty cycle of the converter is calculated using the control law, $u = \frac{2L}{D_1^2 T_s}$. After applying a linearization term, a PID controller is utilized to regulate the input resistance. Since the desired input of the controller is the maximum power point of the PV module, which would change as a function of time, a feedforward control input is used to compensate the desired input variations. Using the feedforward path, the control

system can enhance its convergence speed, at the cost of increasing the steady state error. The error can then be reduced by increasing the integrator coefficient. Further analysis of the proposed feedback controller demonstrates that with a feedforward gain equal to one, and as long as PID coefficients satisfy the following

$$(K_p + 1)^2 \geq 4K_iK_d \tag{2.24}$$

where K_p, K_i, and K_d are PID proportional, integral, and derivative coefficients, respectively, then the error would exponentially converge to zero.

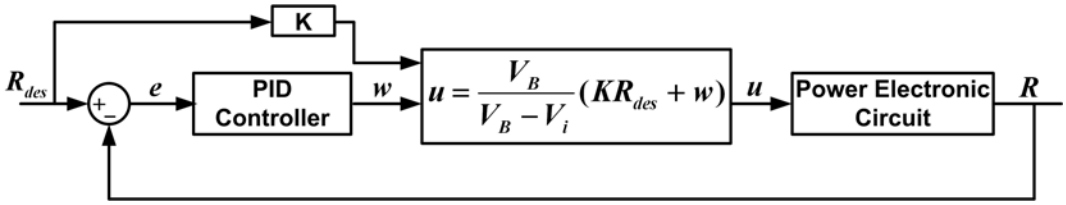

Figure 2.6: Proposed controller structure.

The proposed controller was implemented on a PV module using a dSPACE system which will be discussed in section 3.

2.4.2 Boost Converter Operating in CCM

Based on (2.22), d can be chosen as a suitable control parameter with L and T_s kept constant. Now, let us define the control input u as follows

$$u = 1 - d \tag{2.25}$$

Assuming that the input voltage of the converter can be measured independently in each switching period, the control objective is to minimize the error term

$$e = i_d - i_L = G_d v_i - i_L \tag{2.26}$$

where i_d and G_d are the desired input current and desired conductance at the input of the converter, respectively. Therefore, i_L can be written as

$$i_L = G_d v_i - e \tag{2.27}$$

Based on (2.22) and (2.27), and by performing some algebraic manipulations, one can define control law based on feedback linearization method as follows

$$u = \frac{1}{v_B}\left(v_i - LG_d\frac{dv_i}{dt} - LK_ie\right) \tag{2.28}$$

where K_i is the integrator gain of the controller. Figure 2.7 depicts the proposed controller structure. In this system, the error formula can be derived as

$$e + K_i \int e dt = 0 \tag{2.29}$$

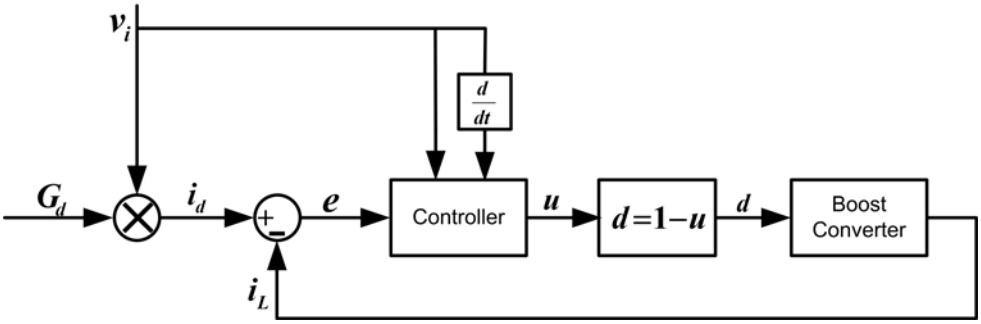

Figure 2.7: Proposed controller structure.

Equation (2.29) indicates that in the proposed controller structure, error would exponentially converge to zero. Therefore, the control input determined by controller for attaining resistive behavior at the converter input, can be generated by using a PWM signal with duty cycle d.

Simulation results

To verify the performance of the proposed controller, the controller designed in section 2.4.2 is simulated in the Matlab/Simulink environment using the circuit parameters reported in section 2.3. From (2.22), the input voltage and current of a boost converter in CCM operation exhibit an inductive relationship. Figure 2.8 illustrates this relationship, which clearly shows the 90 degrees phase difference between these two signals. Therefore, the proposed controller is utilized to achieve a desired resistive behavior by controlling the duty cycle of PWM signals.

Figure 2.9a, illustrates the relationship between input current and voltage of the converter after applying the proposed controller. In this simulation, the input voltage is chosen as $v_i = 3+sin(100\pi t)$, while the desired conductance G_d is chosen as $10S$. This figure illustrates that there is no phase difference between these two signals, and the ratio between them is

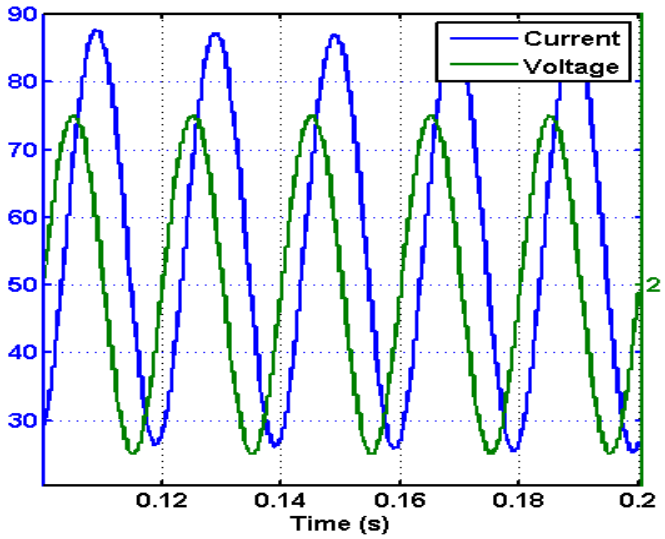

Figure 2.8: Input voltage and inductor current in a boost converter, in CCM operation with a fixed duty cycle value.

equal to the value of G_d. Unlike DCM operation, where the desired resistance is achievable based on a fixed duty cycle [97], in CCM operation the duty cycle should change periodically to regulate the input current. This fact is demonstrated in Fig. 2.9b.

The proposed controller is also able to regulate the input current when a multi-frequency input source is used in which a time varying amplitude with frequencies sufficiently lower than the switching frequency (e.g. at least 10 times). In such a case, the input voltage can be considered constant during each switching period. To verify this, the input source is changed to a multi-frequency input with varying amplitude. Figures 2.10a and 2.10b demonstrate the performance of the proposed controller with respect to this input source.

2.5 Conclusion

In this chapter, an analytical closed-form solution of a boost-type DC-DC converter describing its input characteristics was derived. The model was analyzed and simplified using mathematical techniques for both DCM and CCM. Based on the model, nonlinear feedback controllers were designed to achieve resistive input behavior for input signals with multiple

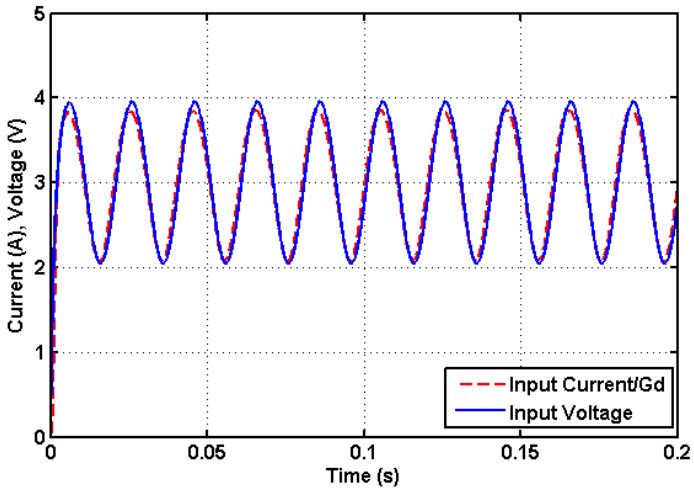

(a)

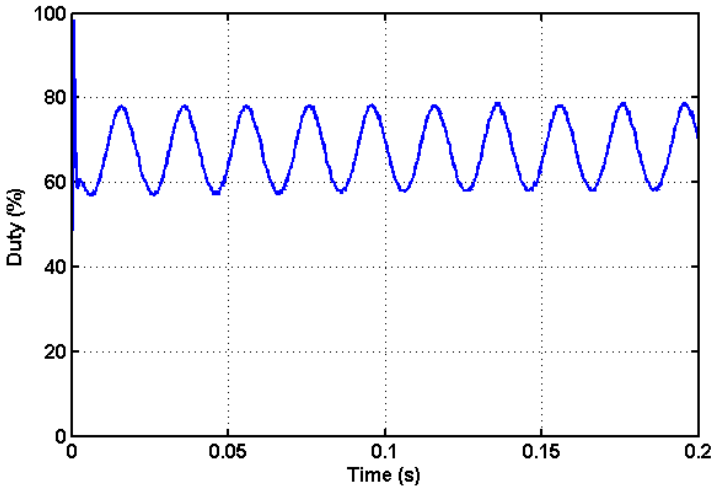

(b)

Figure 2.9: Results for $v_i = 3 + sin(100\pi t)$ (a) Input voltage and current. (b) Duty cycle of the PWM signals.

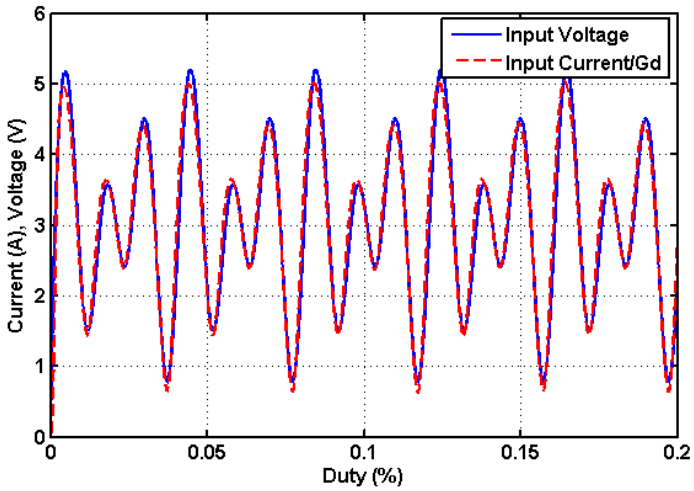

(a)

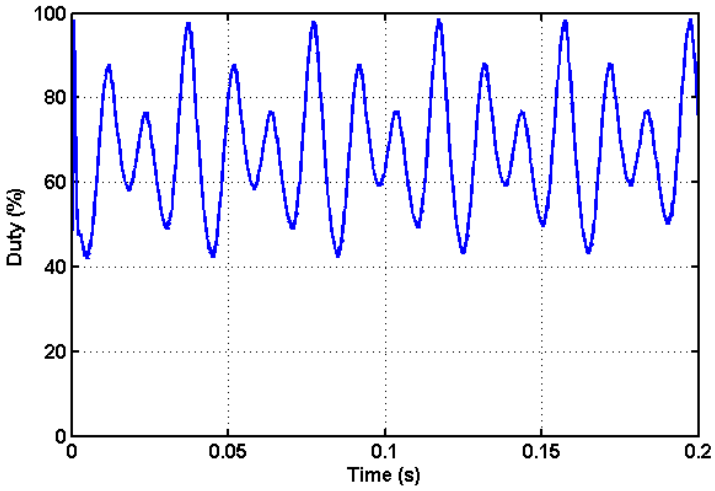

(b)

Figure 2.10: Results for multi-frequency input with varying amplitude (a) Input voltage and current. (b) Duty cycle of the PWM signals.

frequencies, depending on the converter's mode of operation. The closed-form model of the converter can be utilized to obtain the control law for achieving a desired resistive behavior in the input of the converter, i.e., shaping the input waveforms of the converter. Furthermore, performance of the converter using a nonlinear feedback controller was demonstrated through simulation studies. The results verify that the controller can provide a resistive behavior between input current and voltage for arbitrary waveforms. This method can be applied for maximum power transfer from renewable energy sources such as photovoltaic module or regenerative suspension systems, which is the subject of next chapters.

Chapter 3

Maximum Power Point Tracking of Photovoltaic Modules Utilizing Boost Converter Input Resistance Control

Maximum power point tracking for a PV module would allow one to achieve desired operating points in face of varying temperature profiles and irradiation levels. In this chapter, we describe how to achieve this objective by controlling the operating point of the PV module through controlling the input resistance of the boost converter. To this end, a control technique based on a modification of the incremental conductance algorithm is presented by taking into consideration the pseudo-resistive input behavior of boost converter in the discontinuous conduction mode. The proposed method regulates the input resistance of the converter to a desired value, determined by the PV characteristics, to achieve maximum power conversion. The method can be extended to other types of converters such as buck and buck-boost. Furthermore, two estimation techniques to obtain the desired level of PV resistance at the MPP are presented that can provide the desired operating point of the module to the feedback controller in real-time. The performance of the proposed methods are verified by simulation and experimental studies.

3.1 Equivalent Model of a Photovoltaic Module

A PV array consists of a large number of p-n junction diodes, referred to as cells, that can convert light energy into electricity. The equivalent circuit model of a single PV cell is illustrated in Figure 3.1. In this model, the current source is driven by light. The mathematical expression of this model is given by [98] as follows

$$I = I_{PH} - I_s \left(e^{\frac{V+IR_s}{nV_T}} - 1 \right) - \frac{V + IR_s}{R_{sh}} \tag{3.1}$$

where I, V denote the output current and voltage, respectively; I_{PH}, I_s represent the solar induced and diode saturation currents, respectively; R_s, R_{sh} represent the series and shunt resistors, respectively; n is the diode ideality factor; and V_T the thermal voltage.

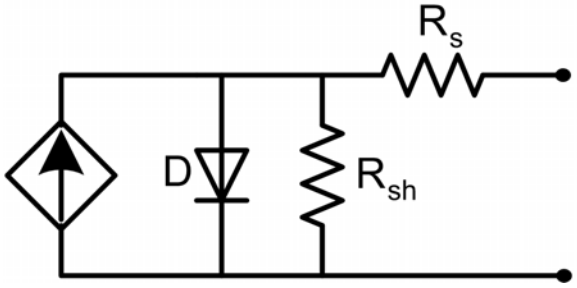

Figure 3.1: Generalized model of the solar cell.

A typical PV module consists of N_p parallel strings and N_s series cells in each string. Figure 3.2 illustrates a typical PV module consisting of N_s series solar cells in each string and N_p parallel strings. An ideal PV module has a very high equivalent shunt resistance. In practice, for silicon or polysilicon PV cells, this resistance can be neglected [99]. This model can be further simplified by neglecting the series and shunt resistors as follows

$$I = N_p I_{PH} - N_p I_s \left(e^{\frac{V}{nN_s V_T}} - 1 \right) \tag{3.2}$$

3.1.1 Electrical Characteristics of a PV Module

Figure 3.3 illustrates the characteristics of a PV module under different irradiance levels (from $750\frac{W}{m^2}$ to $1250\frac{W}{m^2}$). Referring to this figure, the output characteristics of the module are drastically affected by the irradiance level. Also, the output power level has a highly

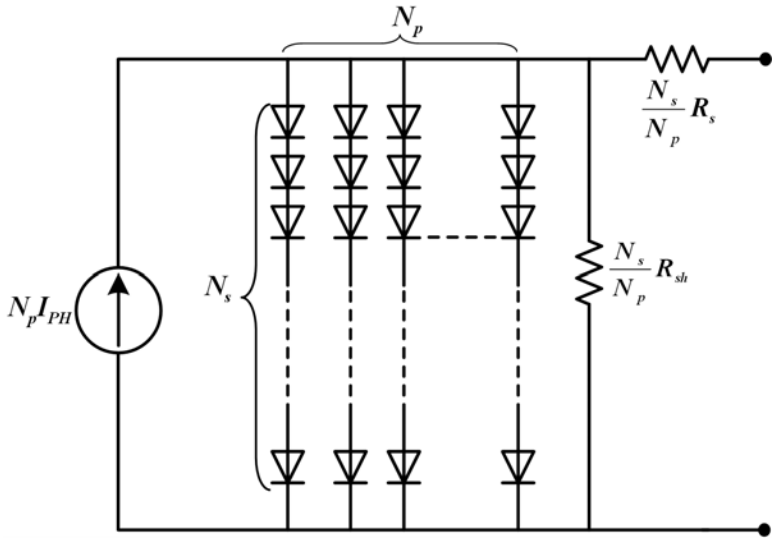

Figure 3.2: General model of a PV module.

nonlinear relationship with irradiation. Each voltage-power curve of the PV module has a maximum at a certain voltage. The nonlinear PV characteristics make the MPPT problem complex. Hence robust MPP tracking, plays a key role in maximizing the utilization of the PV module.

3.2 Controlling the PV Module Operating Point

Let us consider the case when a PV module is connected to a battery, or a DC link, through a boost converter as depicted in Figure 3.4. Assuming that the duty cycle of the switch is such that the converter operates in the DCM, the duty cycle should remain within a certain boundary.

The maximum power point tracking algorithm for the PV module should be able to achieve the desired operating points in face of varying temperature profiles and irradiation levels. Figure 3.5 illustrates the principle of operation of the controller to regulate the operating point of the PV module. The intersection of the PV curve and the load line of the converter determines the operating point of the PV. Therefore, controlling the input resistance of the converter, results in controlling the operating point of the PV module connected to the input of the converter. Ability to change the slope of the load line, i.e. value of resistance, enables us to change the PV module operating point in real time.

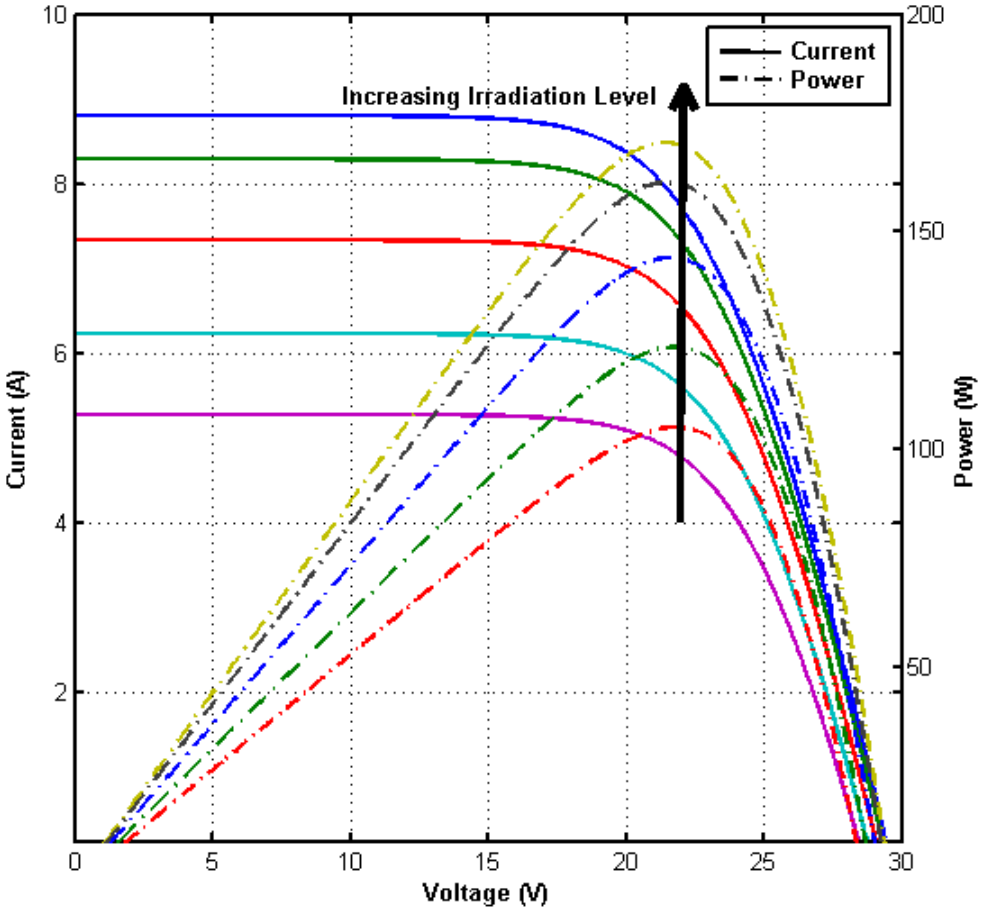

Figure 3.3: PV characteristics curve for different irradiance levels (from $750\frac{W}{m^2}$ to $1250\frac{W}{m^2}$).

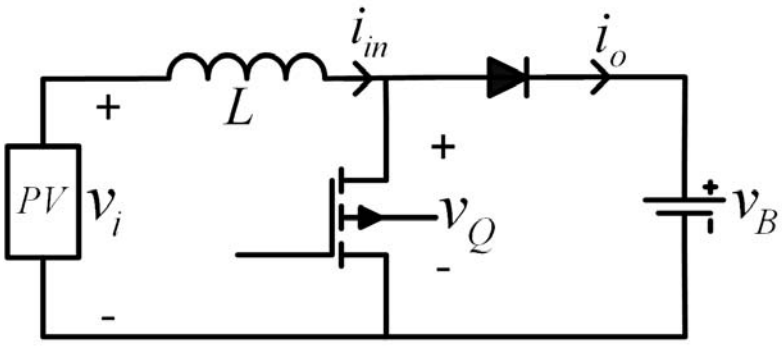

Figure 3.4: Connection of PV to the battery using boost converter.

Figure 2.6 depicts the proposed controller blocks to achieve the desired operating point of the PV. The controller design approach was discussed in section 2.4.1. This controller is utilized to set the operating point of the PV module based on the requirements of the MPPT algorithm.

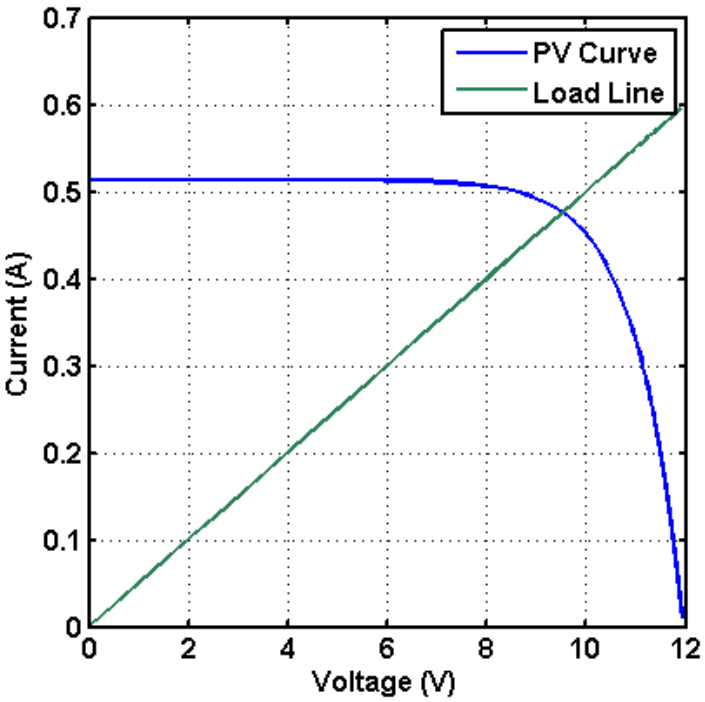

Figure 3.5: Controlling the operating point of the PV module.

3.3 Modified Incremental Conductance Method

The main purpose of a MPPT controller is to find the voltage which maximizes the output power of the PV. The incremental conductance method is based on setting the derivative of the power-voltage curve is equal to zero [100]. Thus, using $P = V.I$, we have

$$\frac{dP}{dV} = 0 \Rightarrow I + V.\frac{dI}{dV} = 0 \Rightarrow -\frac{V}{I} = \frac{dV}{dI} \tag{3.3}$$

From (3.3), it follows that the MPP can be reached if the instantaneous resistance, i.e. $\frac{V}{I}$, is equal to the incremental resistance, i.e. $\frac{dV}{dI}$, with a negative sign. In the modified

incremental conductance approach, we re-formulate the above scheme as a feedback control problem where the error between the input resistance of the converter and the incremental resistance of the PV should approach zero at the maximum power point. Figure 3.6 illustrates the structure of the electronic hardware and the MPPT system. The output voltage and current of the PV and the battery voltage are used in the controller to determine an appropriate value for the duty cycle of PWM switching for the boost converter. As noted before, the proposed modification to the incremental conductance approach is to control the input resistance of the power converter such that it converges to the incremental conductance of the PV module.

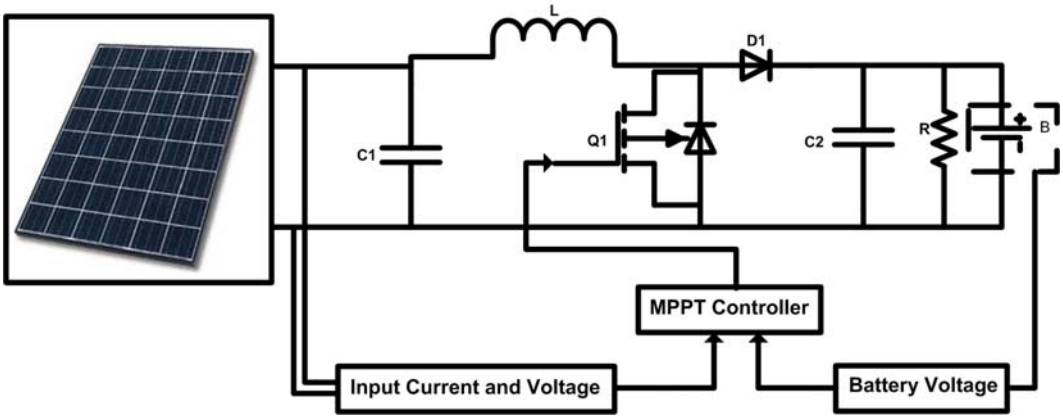

Figure 3.6: Structure of the MPPT system.

3.3.1 Simulation Results

A Simulink model of the proposed MPPT algorithm was developed in the MATLAB/Simulink environment. Tables 3.1 and 3.2 demonstrate the parameters of the photovoltaic module and the circuit, respectively. To evaluate performance of the controller, the simulation module was subjected to different irradiation levels. The PV was subjected to abrupt changes in irradiation around an average irradiation level for a sunny day ($1000W/m^2$). Each irradiation will result in a different MPPT, as depicted in Figure 3.7. The PID coefficients K_P, K_I and K_D, were selected as 1.1, 0.5, and 0.5, respectively. Also, the gain K (see Figure 2.6) of the desired input feedforward was chosen as 100. These gains were chosen by trial and error to achieve acceptable performance in terms of error in the incremental and input resistances.

Figure 3.7 illustrates the output power of the PV module under the proposed MPPT

Table 3.1: Photovoltaic module parameters.

Parameter	**Value**
I_L	$7.34A$
I_1	$10^{-6}A$
I_1	$10^{-6}A$
R_s	$0.01ohms$
R_{sh}	$100ohms$
n	1.5
V_T	$25.7mV$

Table 3.2: Circuit parameters.

Parameter	**Value**
Battery	Lead-acid, 30V
Inductance (L)	$105uH$
Converter input capacitance	$500uF$
Converter output capacitance	$600uF$
Switching Frequency	$2KHz$

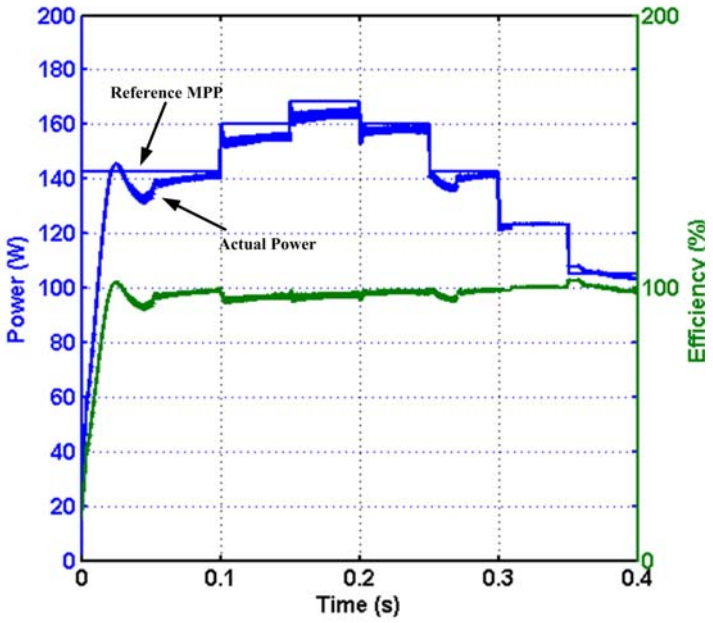

Figure 3.7: Output power of photovoltaic module versus the actual maximum power, and the tracking efficiency.

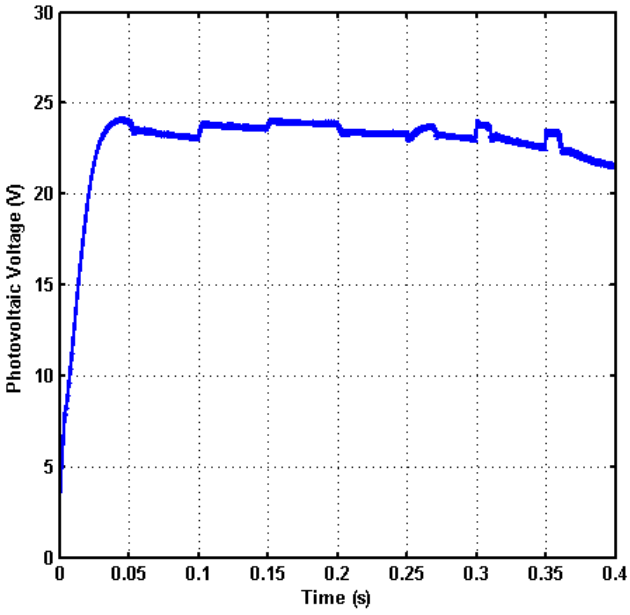

Figure 3.8: Output voltage of photovoltaic module.

controller. Also, the actual maximum power of the module and the tracking efficiency are illustrated in this Figure. Figure 3.7 illustrates performance of the closed-loop controller. Besides, Figure 3.8 represent the photovoltaic module output voltage. This figure demonstrates that the MPP voltage will remain almost constant in different irradiations. This fact can also be observed from Figure 3.3, where the MPP occurs at an almost constant voltage regardless of the irradiation level. Also, Figure 3.9 illustrates the relative error performance of the controller. This figure demonstrates that the error is less than 2.5% during the operation. Figure 3.10 illustrates the magnified relative error of the feedback controller system, to demonstrate its changes. As it can be observed from this figure, error will change at the beginning of each change in irradiation level, but the feedback controller manages to regulate the error.

Furthermore, Table 3.3 provides output power and tracking efficiency data under rapid changes in the ambient temperature. The tracking efficiency is computed as follows,

$$\eta = \frac{P_{PVout}}{P_{MPP}} \times 100 \tag{3.4}$$

where P_{PVout} is the power reached by using the MPPT controller, while P_{MPP} is the expected maximum power output.

Simulation results in Figure 3.7 show that a significant improvement in the speed of convergence (in the order of a few milli-seconds) is achieved using the proposed strategy when compared to previously published works in this area (e.g., [100], [101],and [102]). The results also indicate that the proposed method is robust against sudden changes ambient conditions such as irradiation and temperature.

Table 3.3: MPPT controller performance at different temperatures.

Temperature (C)	P_{MPP} (W)	P_{PVout} (W)	η
45	129	126	97.7%
35	137	135	98.6%
25	144	142	98.7%
15	151	150	99.4%
5	158	157	99.4%

The proposed method exhibits a relatively high tracking efficiency between 97% and 100%, over a wide irradiation range. Furthermore, the average error in finding the MPP of the

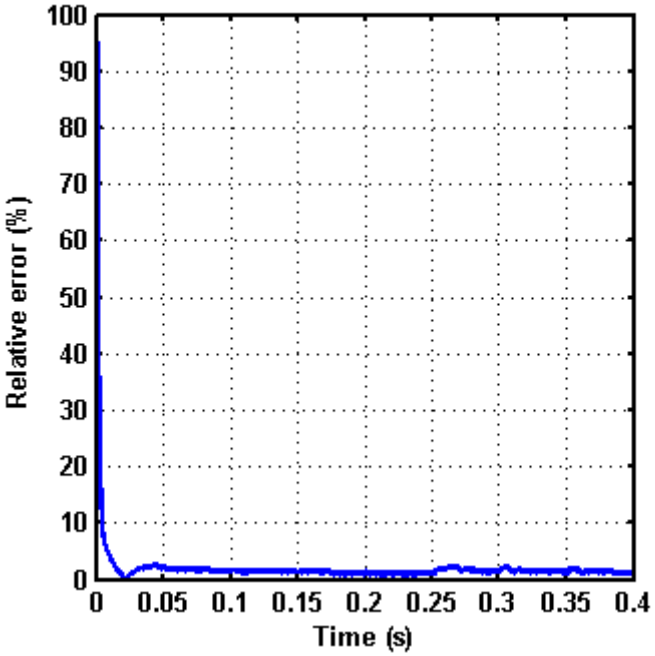

Figure 3.9: Controller performance error..

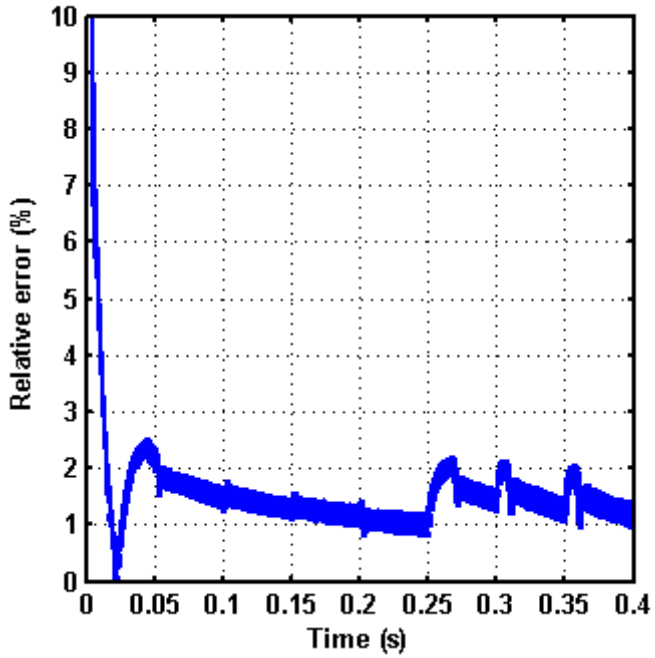

Figure 3.10: Controller performance error (magnified).

photovoltaic module is less than 1% for different irradiation levels and ambient temperatures. The efficiency under different conditions is above 97% which is robust to abrupt changes in operating conditions. The conventional incremental conductance method is a simple and efficient approach in commonly used MPPT algorithms. Recent works on the variable step incremental conductance algorithms have generally reported high efficiencies [101, 103]. However, common problems using these approaches are the convergence time and steady state oscillations when approaching the maximum power point. In Figure 3.7, the changes in steady state power is less than 1% compared to variations of about 10% in [100].

3.4 Real-Time Identification Utilizing Maximum Power Point Approximation

The results of section 3.2 demonstrate that a PV module system can be operated at a desired operating point using a proper controller. In a practical situation, this technique can be used to track the MPP of a PV module. To do so, a real-time identification algorithm was developed to identify the PV curve and determine the MPP as described in the following. During the first stage, the PV curve relationship, equation (3.2), is identified. This identification is based on the knowledge of the structure of the PV module and also an approximation of the PV module parameters. In the typical PV module utilized in this work, the solar cells are connected in series with each other to increase the output voltage, i.e. $N_p = 1$ in (3.2). For a given temperature, the values of parameters of I_s and nN_sV_T are constant for each PV module, which can be approximated using the Curve Fitting Toolbox of Matlab software. In this study, we operated the PV module under different irradiance conditions and recorded the values of module currents and voltages. Using the Curve Fitting Toolbox, the parameters of I_s and nN_sV_T were identified at room temperature and and the mathematical model of the PV was built to yield the following model

$$I = I_{PH} - C_1\left(e^{\frac{V}{C_2}} - 1\right) \tag{3.5}$$

where both C_1 and C_2 are known parameters. Note that the ambient temperature can affect the above PV model. However, low-cost temperature sensors can be used to modify the coefficients in the above model, which can be further written as

$$I = I_{PH} - C_1(T)\left(e^{\frac{V}{C_2(T)}} - 1\right) \tag{3.6}$$

where T is the ambient temperature (in $^{\circ}C$). The terms $C_1(T)$ and $C_2(T)$ are described as [98]

$$C_1(T) = I_s(T) = I_{s,ref}\left(\frac{T}{T_{ref}}\right) \tag{3.7}$$

$$C_2(T) = nN_sV_T(T) = nN_s\left(\frac{k(T+273.15)}{q}\right) \tag{3.8}$$

where $I_{s,ref}$ is the diode saturation current in T_{ref} (which is normally $25^{\circ}C$), k is the Boltzmann constant, and q is the magnitude of the electrical charge on the electron.

During the operation of the MPPT system, the PV module's I_{PH}, will be changing according to the ambient irradiance level. Therefore, a real-time system should be able to analyze the changes in PV module current and voltage and approximate the value of I_{PH} in each control cycle. Using the measured values, the value of I_{PH} is calculated based on (3.6). Using this value, the open circuit voltage of the PV module, V_{OC}, is expressed as

$$V_{OC} = nN_sV_Tln\left(\frac{I_{PH}}{I_s}+1\right) = C_2(T)ln\left(\frac{I_{PH}}{C_1(T)}+1\right) \tag{3.9}$$

In the next step, the value of the PV desired resistance at the MPP should be determined and fed to the controller. Empirical studies have shown that the MPP usually occurs at approximately $0.77V_{OC}$ [44]. Using this voltage, the current at MPP is calculated as follows

$$I_{MPP} = I_{PH} - C_1(T)\left(\left(\frac{I_{PH}+C_1(T)}{C_1(T)}\right)^{0.77}-1\right) \tag{3.10}$$

Hence, the desired input resistance of the boost converter is set to the value of the resistance at MPP given by

$$\begin{aligned} R_{des} &= \frac{0.77V_{OC}}{I_{MPP}} \\ &= \frac{0.77C_2(T)ln\left(\frac{I_{PH}+C_1(T)}{C_1(T)}\right)}{I_{PH}-C_1(T)\left(\left(\frac{I_{PH}+C_1(T)}{C_1(T)}\right)^{0.77}-1\right)}. \end{aligned} \tag{3.11}$$

By controlling the resistance derived in (3.11), the MPP of the PV module can be tracked in real-time. In the following section, the results of the experiment of the performance of the designed MPPT controller is analyzed.

Table 3.4: Implemented circuit and PV module parameters.

Parameter	Value
PV short circuit current, I_{SC}	$8.20A$
PV open circuit voltage, V_{OC}	$14.75V$
Lead Acid Battery, V_B	$36V$
Inductance, L	$100uH$
Converter input capacitance	$5mF$
Converter output capacitance	$0.5mF$
Switching frequency	$2KHz$

3.4.1 Experimental Results

Description of the Setup

The proposed MPPT control system was implemented for operation with the *DAY4-48MC* PV module using a boost converter, with the data listed in Table 3.4. The setup built for doing the experiments is depicted in Figure 3.11. In this setup, the irradiance is generated using Halogen lamps to allow making instantaneous changes in the irradiation levels. The position and distance of the lamps is set to have the module surface insolation as uniform as possible in the laboratory conditions. Reaching the nominal MPP of the module requires relatively high power levels to be applied to the Halogen lamps. In this setup, four $500W$ lamps were used. The irradiance of these lamps are lower than the maximum irradiance for the PV module to reach its nominal maximum power. Furthermore, increasing the number of lamps was not practical due to space limitations. Thus, the maximum achievable power output of the PV module using the implemented setup is lower than its nominal maximum power. To implement the controller, a dSPACE system (DSP1104) was used. The controller was built in the Matlab/Simulink environment with the C code generated for the DSP processor using the Mathworks Real-Time Workshop Toolbox. The dSPACE system and power electronics circuit are depicted in Figure 3.12. Also, the overall control system block diagram is indicated in Figure 3.13, which is comprised of the PV module, boost converter, battery, and the controller. In this setup, energy is extracted from the PV module is fed to the converter which is used to charge the battery. The control system regulates the energy flow in such a way that the maximum power can be extracted from the PV module under

varying irradiation levels.

Figure 3.11: Experimental laboratory setup. The irradiance is simulated using Halogen lamps.

Operating Point Control

The control system was tested for two different conditions. First, controlling the operating point of the PV module was investigated, in which the input resistance of the converter was set to 10 Ω. At this operating point, the PV module operates in its current source region. The irradiation level was also changed instantaneously during the operation. In the next step, the resistance was set to 60 Ω (voltage source region) and the transient response of the

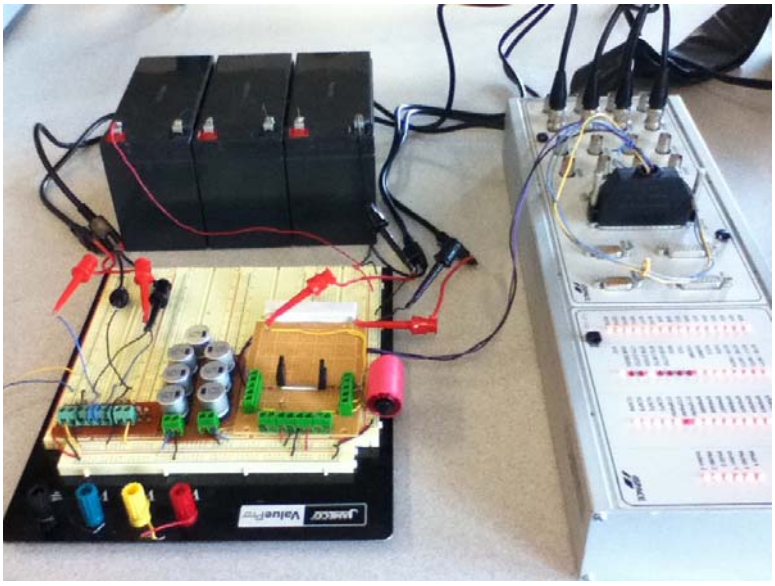

Figure 3.12: Implemented circuit and the dSPACE system.

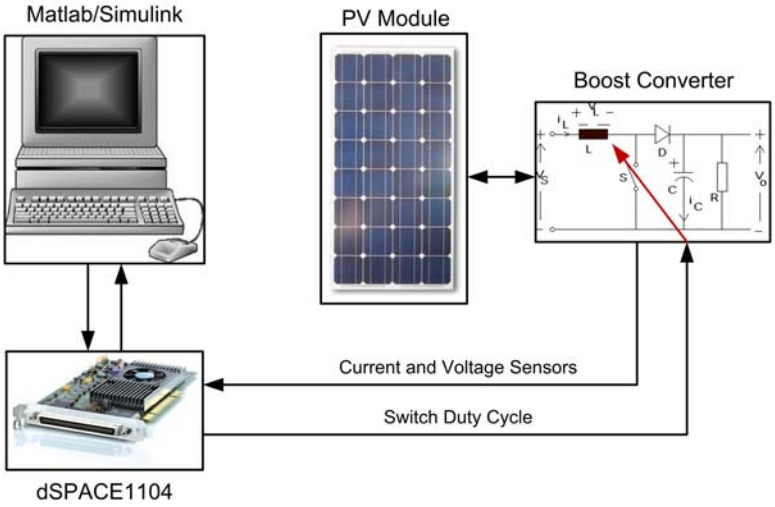

Figure 3.13: Overall control system diagram.

controller system was obtained. Figure 3.14 demonstrates the results of setting the desired resistance as 10 Ω. Figure 3.14a demonstrates the anticipated changes in the PV voltage and current based on two different irradiations with a fixed load line. Figures 3.14b and 3.14c demonstrate the changes in PV module current and voltage due to changes in the ambient conditions. As it is anticipated, both voltages and currents are changing, but the resistance of the PV module (Figure 3.14d) remains constant. Figure 3.14e demonstrate the changes in the controller output (duty cycle). From (2.18), a decrement in the PV module voltage (while other parameters are constant), results in an increment in duty cycle. Finally, Figure 3.14f demonstrates the changes in the V module current and voltage when the irradiation changes. This figures illustrates that, regardless of the changes in the ambient condition, the PV module operating point will always remain on a pre-defined load line.

Figure 3.15 demonstrates the results when the desired resistance is set to 60 Ω. With this resistance, the PV module system will work in the voltage source region. The results of this experiment illustrate the performance of the controller during the transient conditions.

Implementation of the Proposed MPPT Method

To implement the proposed MPPT method, the first step is to identify the PV module parameters using sampled data and the Curve Fitting Toolbox of Matlab software. Figure 3.16a illustrates the sampled voltages and currents of the module under two different laboratory conditions. Figure 3.16b illustrates the curves fitted based on experimental data. The PV module can thus be modeled as follows

$$I = I_{PH} - 4.7525 \times 10^{-5} \left(e^{\frac{V}{1.374}} - 1 \right) \tag{3.12}$$

which is the same as (3.5) with known C_1 and C_2 parameters. The ambient temperature is assumed to be equal to T_{ref}. To test the performance of the controller, an instantaneous change in the irradiation is applied to the system at time 1.53 seconds. This change, results in 60% decrease in the short circuit current of the PV module.

Figure 3.17 depicts the results obtained using the proposed controller. Figures 3.17a and 3.17b illustrate the PV module power and current (their experimental and theoretical values), which indicate that the controller can compensate the sudden changes in ambient conditions and can successfully track the MPP of the system in about 0.7 seconds (with the error of less than 5%), which is fast enough compared to similar works such as [103], [101]. Figure 3.17c demonstrates the anticipated values of the operating point under different irradiations levels.

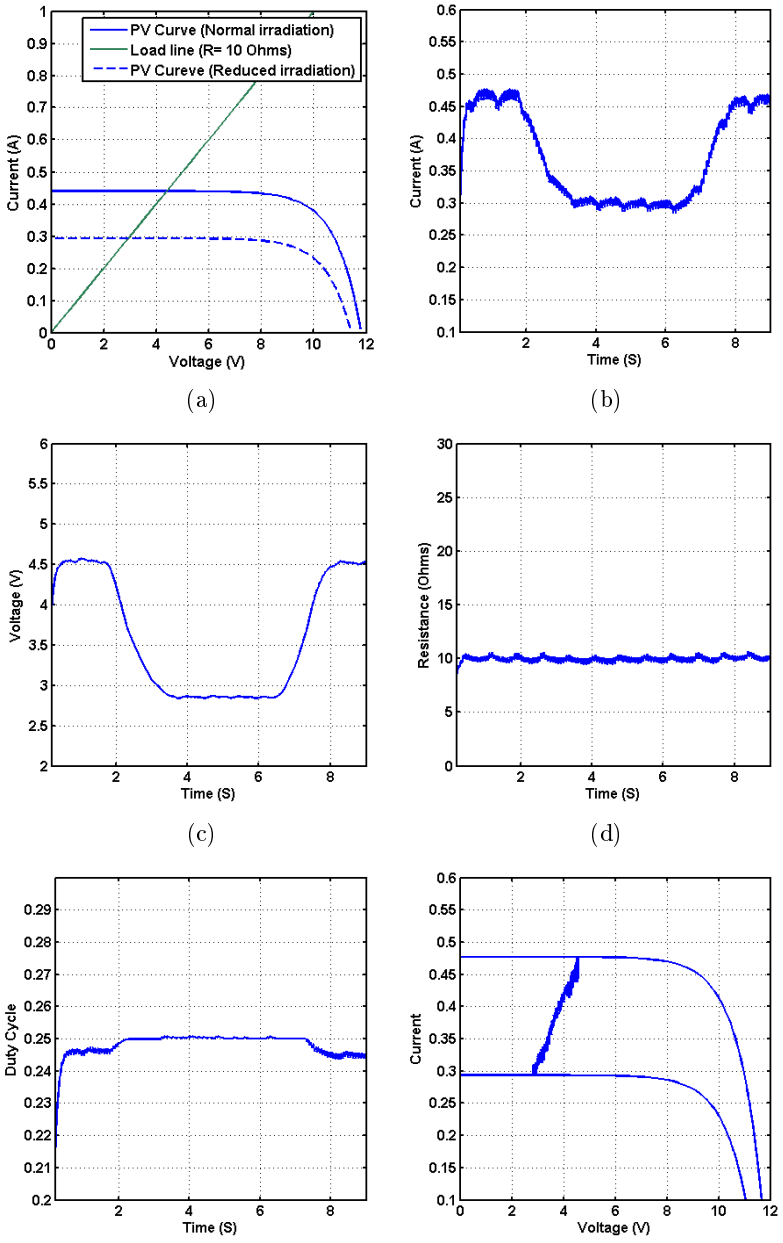

Figure 3.14: Results of controlling the operating point of the PV module (a) Load line for resistance of 10 *Ohms* and PV curves for two different irradiations (b) Output current of the PV module (c) Output voltage of the PV module (d) Converter input resistance (e) Duty cycle of the converter (f) Changes in PV voltage and current.

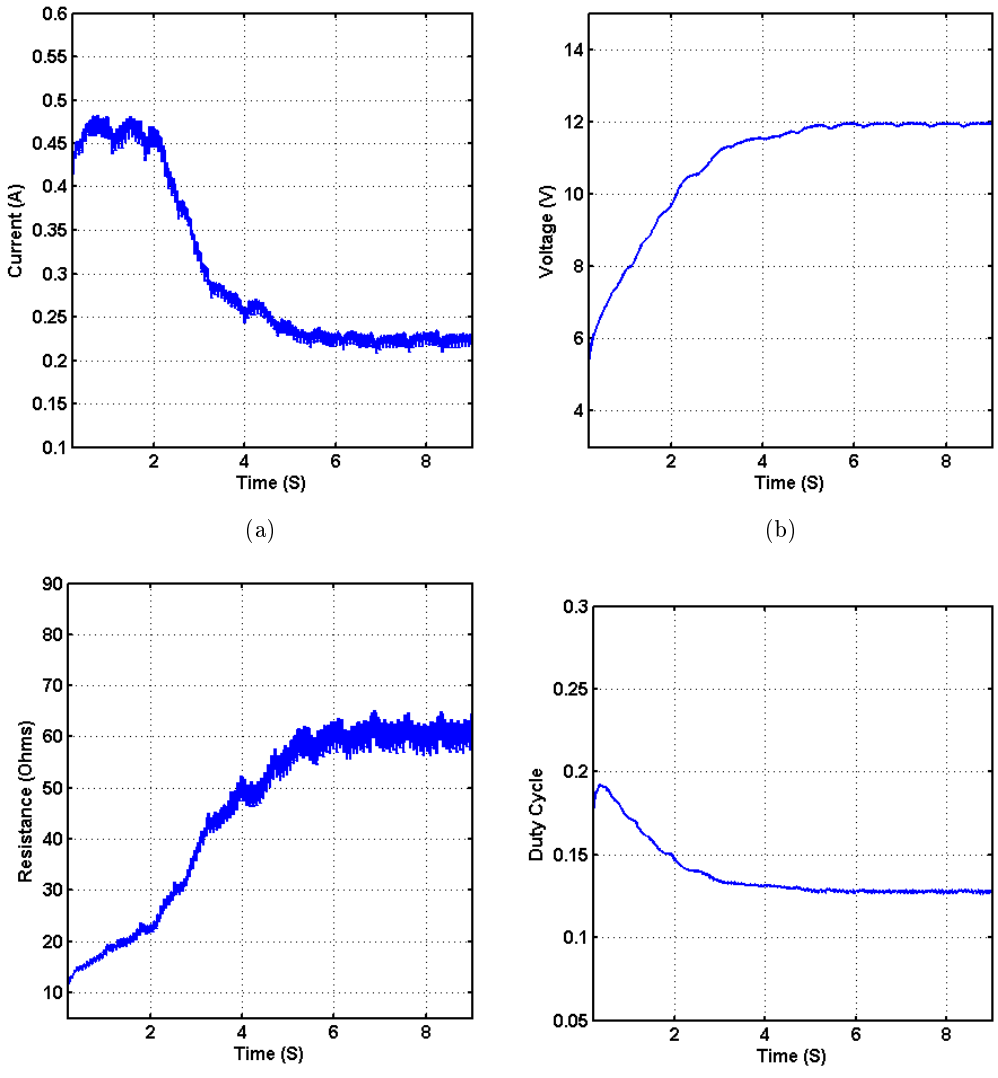

Figure 3.15: Transient response of the control system (a) PV module current (b) PV module voltage (c) Converter input resistance (d) Duty cycle of the converter.

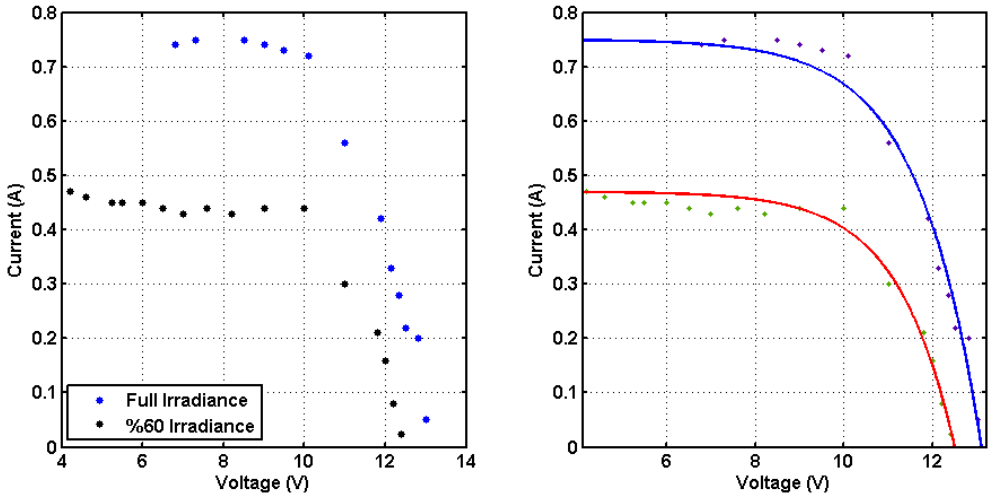

(a) (b)

Figure 3.16: (a) Sampled data for curve fitting (b) Results of the Curve Fitting Toolbox of Matlab.

Figure 3.17d demonstrates the actual values of the desired operating point. Finally, Figures 3.17e and 3.17f illustrate the I-V and P-V diagrams of the controlled PV power system, which demonstrate no chattering in the operating point path and good MPPT accuracy (compared to methods discussed in [104]).

3.5 Real-Time MPP Identification Utilizing the Lambert W-Function

In this section, the identification method has been enhanced, to determine the MPP based on real-time sensory data. Similar to the previous method, during the first stage, the PV curve is identified based on a knowledge of the parameters of the PV module given by the manufacturer datasheet and PV module's mathematical model. The manufacturer data at certain points, referred to as *remarkable points* by [105], can be used in the identification step. Also, similar to the last approach, we assume the number of parallel PV cells as one, i.e., $N_p = 1$. For a given temperature, the parameters I_s, nN_sV_T, and R_s are constant, which can be approximated using the available information on *remarkable points*. The values of short circuit current I_{SC}, open circuit voltage V_{OC}, MPP current I_{MPP}, and MPP voltage

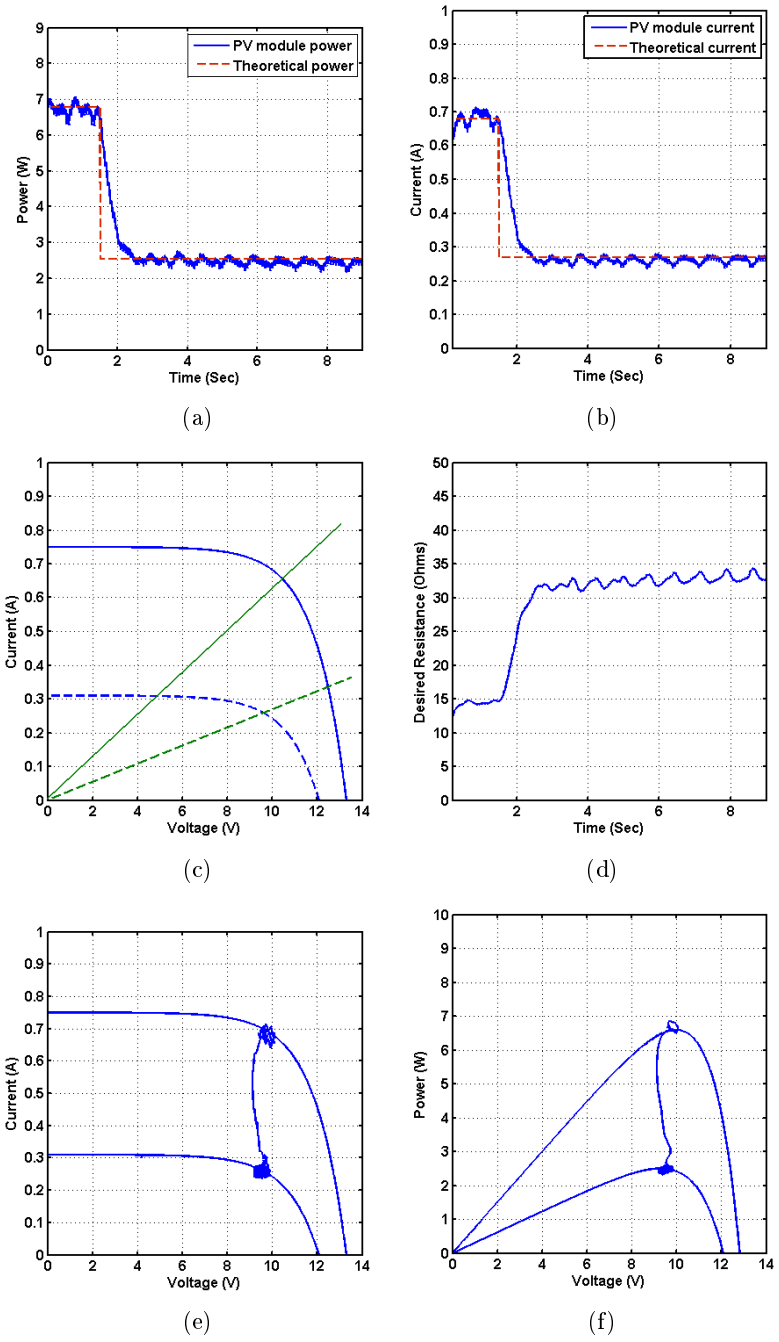

Figure 3.17: Results of the proposed MPPT methods (a) Output power of the PV module (b) Output current of the PV module (c) PV module and desired load line curves in two different irradiance levels (d) Desired resistance identification result (e) Changes in PV voltage and current (f) Changes in PV voltage and power.

V_{MPP}, are given in the manufacturer's datasheet for every PV module. Based on these values, a mathematical model of the module can be constructed at a nominal temperature. However, the modeling accuracy is dependent on the accuracy of the PV module data such as I_{SC} or V_{OC}. For instance, degradation of these values with respect to time, i.e., aging phenomena, will have a negative impact on the accuracy of the PV model. [106] shows that for a typical PV module, in a four year period, the I_{SC} and V_{OC} change by -7.6% and -1.6%, respectively. Based on the above data, the ratio $\frac{V_{MPP}}{V_{OC}}$ would decrease, whereas R_{MPP} would increase by 4% in 4 years.

Under the short circuit condition ($V = 0$), the value of I_{SC} can be found as follows

$$I_{SC} = I_{PH} - I_s \left(e^{KI_{SC}R_s} - 1\right) \tag{3.13}$$

in which the value of nN_sV_T has been replaced with $\frac{1}{K}$ for simplicity. Note that I_{PH} is the nominal value for which all other measurements are made. The value of I_{PH} is identified in real-time based on the voltage and current measurement of the PV module. Furthermore, under the open circuit condition ($I = 0$) we have

$$I_{PH} = I_s \left(e^{KV_{OC}} - 1\right). \tag{3.14}$$

Using (3.13) and (3.14), the short circuit current can be calculated as

$$I_{SC} = I_s \left(e^{KV_{OC}} - e^{KI_{SC}R_s}\right). \tag{3.15}$$

As the value of R_s is very small (usually less than 1Ω), the value of $e^{KI_{SC}R_s}$ is negligible with respect to $e^{KV_{OC}}$. Therefore

$$I_{SC} = I_s e^{KV_{OC}} \approx I_{PH} \tag{3.16}$$

Using (3.16), and at the maximum power point, (3.2) can be written as

$$I_{MPP} = I_s \left(e^{KV_{OC}}\right) - I_s \left(e^{K(V_{MPP}+I_{MPP}R_s)}\right) \tag{3.17}$$

It is also known that the derivative of power P with respect to voltage V at MPP is zero.

$$\left.\frac{dP}{dV}\right|_{(V_{MPP},I_{MPP})} = 0 \tag{3.18}$$

Using (3.16)-(3.18), and after some algebraic manipulations, the expressions for K, I_s, and R_s are obtained as follows

$$K = \frac{I_{MPP}}{V_{MPP}\left(I_{SC} - I_{MPP}\right)} \tag{3.19}$$

$$I_s = I_{SC} e^{-KV_{OC}} \tag{3.20}$$

$$R_s = \frac{1}{KI_{MPP}} \times \left(ln \left(\frac{I_{SC} - I_{MPP}}{I_s} \right) - KV_{MPP} \right). \tag{3.21}$$

Thus, based on the values of I_{SC}, V_{OC}, I_{MPP}, and V_{MPP}, the values of I_s, K, and R_s can be identified. Using (3.19)-(3.21) and (3.2), one can calculate the value of I_{PH} for each irradiation level, given the PV module's current and voltage measurements. It should be noted that the shunt resistance R_{sh} and ambient temperature can affect the modeling accuracy. However, the proposed MPPT method utilizes the PV module resistance at MPP, which exhibits the least dependency on the shunt resistor and temperature. These dependencies are analyzed in section 3.5.2.

3.5.1 Real-Time MPP Identification

In this section, it is assumed that the model of the PV module is known and the objective is to find the MPP. An analytic approach is presented here to find the PV module resistance at MPP. This resistance will then be used to track the MPP. Based on the model illustrated in Figure 3.18, the value of the PV module resistance R_{pv} can be defined as the summation of the series resistance R_s and the resistance of the nonlinear part of the model denoted by R_{temp}. Since the objective is to find the MPP resistance R_{MPP}, one can neglect R_s and add it later. This assumption is justified based on the value of R_{MPP}, which is usually more than 2Ω, whereas a typical value of R_s is 0.15Ω.

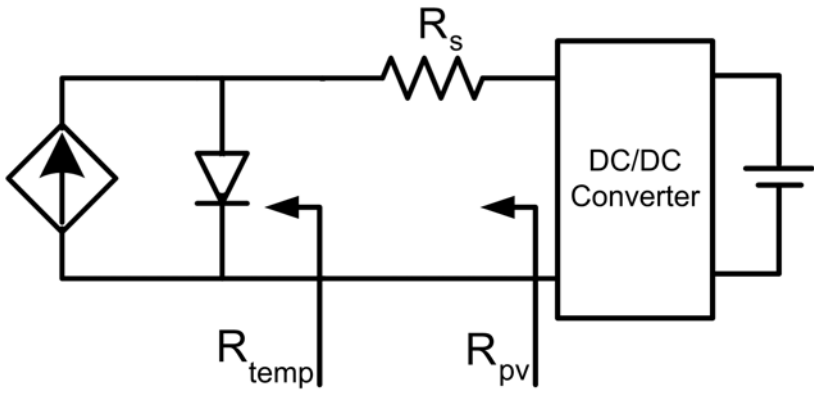

Figure 3.18: Circuit diagram illustrating the resistances R_{pv} and R_{temp}.

Furthermore, at the MPP we have

$$\begin{aligned} P = VI \quad &\rightarrow \quad \left.\frac{dP}{dV}\right|_{MPP} = I_{MPP} + V_{MPP} \left.\frac{dI}{dV}\right|_{MPP} = 0 \\ &\rightarrow \quad R_{MPP} = \frac{V_{MPP}}{I_{MPP}} = \left.\frac{-dV}{dI}\right|_{MPP} \end{aligned} \tag{3.22}$$

Based on the simplified model of the PV module, the value of the incremental resistance $\frac{dV}{dI}$ can be obtained as follows

$$\begin{aligned} V \quad &= \quad \frac{1}{K} ln\left(\frac{I_{PH} - I}{I_s} + 1\right) \\ &\rightarrow \quad \left.\frac{-dV}{dI}\right|_{MPP} = \frac{1}{K} \times \frac{1}{I_{PH} + I_s - I_{MPP}} \end{aligned} \tag{3.23}$$

Replacing $\frac{1}{X} = I_{PH} + I_s - I_{MPP}$ and using Eqs. (3.22) and (3.23) we have

$$R_{MPP} = \frac{X}{K}. \tag{3.24}$$

Furthermore, the value of R_{MPP} can be found from $\frac{V_{MPP}}{I_{MPP}}$ as follows

$$V_{MPP} = \frac{1}{K} ln\left(\frac{I_{PH} + I_s - I_{MPP}}{I_s}\right) = \frac{1}{K} ln\left(\frac{1}{XI_s}\right) \tag{3.25}$$

Hence,

$$R_{MPP} = \frac{V_{MPP}}{I_{MPP}} = \frac{1}{K\left(I_c - \frac{1}{X}\right)} ln\left(\frac{1}{XI_s}\right) \tag{3.26}$$

where $I_c = I_{PH} + I_s$ is a constant value.

Using (3.24) and (3.26) we have

$$e^{I_c X - 1} = \frac{1}{XI_s} \rightarrow \frac{I_s}{e} e^{I_c X} = \frac{1}{X} \tag{3.27}$$

In (3.27), the values of I_c and I_s are known while the value of X is unknown. Solving this equation for X yields R_{MPP} based on (3.24). The solution of this equation can be found based on the Lambert W-Function W, which is a nonlinear inverse function of $f(W) = We^W$ [107]. Thus, the solution of (3.27) can be expressed as

$$X = \frac{1}{I_c} W\left(\frac{eI_c}{I_s}\right) \tag{3.28}$$

where $W(.)$ is the Lambert W-Function.

To find the value of X analytically, one can use the asymptotic formula for the Lambert W-Function given by

$$\begin{aligned} W(z) &= lnz - lnlnz + \sum_{k=0}^{\infty}\sum_{m=0}^{\infty} c_{km}(lnlnz)^{m+1}(lnz)^{-k-m-1} \\ &= L_1 - L_2 + \frac{L_2}{L_1} + \frac{L_2(-2+L_2)}{2L_1^2} + \frac{L_2(6-9L_2+2L_2^2)}{6L_1^3} \\ &+ \frac{L_2(-12+36L_2-22L_2^2+3L_2^3)}{12L_1^4} \\ &+ \frac{L_2(60-300L_2+350L_2^2-125L_2^3+12L_2^4)}{60L_1^5} + O\left[\left(\frac{L_2}{L_1}^6\right)\right] \end{aligned} \tag{3.29}$$

where $L_1 = lnz$ and $L_2 = lnL_1$. The above formula yields reasonably accurate results for $W(z)$ when $z \geq 3$, which is true for our case since $\frac{eI_c}{I_s} \gg 3$. Using (3.28) and (3.24), the optimal operating point given by R_{MPP} can be calculated. In particular, (3.29) can be approximated by its first four terms as follows

$$W(z) = L_1 - L_2 + \frac{L_2}{L_1} + \frac{L_2(-2+L_2)}{2L_1^2} \tag{3.30}$$

which is computationally less expensive than (3.29). A numerical analysis based on the data used in this study, section 3.5.3, indicates that the approximation error in using (3.30) is less than 0.01%.

3.5.2 Sensitivity Analysis

As mentioned in section 3.5, the modeling accuracy of the PV module is dependent on the ambient temperature. Also, the value of the shunt resistor, neglected in deriving the model, may affect the accuracy as well. The sensitivity of the resistance of R_{MPP} is analyzed with respect to these parameters as follows. Figure 3.18 can be updated by adding the shunt resistance R_{sh} between R_s and R_{temp}. Therefore, R_{pv} can be calculated as follows

$$R_{pv} = R_s + R_{sh}||R_{temp} \tag{3.31}$$

Using (3.31), the sensitivity of the R_{pv} with respect to R_{sh} can be calculated as

$$\frac{\partial R_{pv}}{\partial R_{sh}} = \left(\frac{R_{temp}}{R_{sh}+R_{temp}}\right)^2 \approx 0 \tag{3.32}$$

owing to the fact that R_{temp} is negligible with respect to R_{sh} ($1K\Omega$) [105]. Therefore, the change in R_{MPP} due to neglecting R_{sh} is quite small.

Utilizing (3.24) and (3.28), and noting that $I_s \ll I_{PH}$, the value of PV resistance at the maximum power point is given by

$$R_{MPP} = \frac{1}{I_c K} W\left(\frac{eI_c}{I_s}\right) \approx \frac{1}{I_{PH} K} W\left(\frac{eI_{PH}}{I_s}\right) \tag{3.33}$$

from which the power of the PV module at MPP can be obtained as follows

$$P_{MPP} = \frac{I_{PH}}{K} \frac{\left(W\left(\frac{eI_{PH}}{I_s}\right) - 1\right)^2}{W\left(\frac{eI_{PH}}{I_s}\right)} \tag{3.34}$$

In the above equation, the most temperature dependent parameters are K and I_s with dependencies given by

$$K(T) = nN_s V_T = \frac{nN_s \kappa T}{q} \tag{3.35}$$

$$I_s(T) = CT^3 e^{\frac{-qV_g}{\kappa T}} = CT^3 e^{\frac{-V_g}{V_T}} \tag{3.36}$$

where κ is the Boltzmann's constant $1.38 \times 10^{-23} J/K$, T is the ambient temperature in Kelvin, and q is the electron charge $1.6 \times 10^{-19} C$. Also, V_g is the band gap voltage ($1.11 V$), and C is a constant [108].

Note that although I_{PH} is dependent on the temperature, it will not affect the accuracy of the algorithm as it will be calculated in each control cycle using real-time measurements of PV voltage and current.

Using (3.34), the power at MPP can be obtained, which is dependent on the temperature. This dependency can be compensated by using a temperature sensor on the module to modify the values of I_s and K based on (3.35) and (3.36) to reach the maximum accuracy. However, the proposed algorithm has a very low dependency on the temperature. To investigate this relationship, the power of the PV module at each operating point should be obtained. Using (3.2) and $N_P = 1$, let us assume that a resistive behavior has been enforced at the PV module terminals through feedback control regulated at R_{OP}. Hence

$$\alpha V = \beta - e^{\gamma V} \tag{3.37}$$

where $\alpha = \frac{1}{R_{OP} I_s}$, $\beta = \frac{I_{PH}}{I_s}$, and $\gamma = K\left(1 + \frac{R_s}{R_{OP}}\right)$. Solving (3.37) by using the Lambert

W-Function results in

$$V = \frac{\beta}{\alpha} - \frac{W\left(\frac{\gamma e^{\frac{\beta\gamma}{\alpha}}}{\alpha}\right)}{\gamma} \tag{3.38}$$

from which, the power is obtained as

$$P = \frac{V^2}{R_{OP}}. \tag{3.39}$$

Using (3.33), the value of the PV resistance at its MPP, R_{MPP}, can be obtained. However, this value is just valid at the nominal temperature $25°C$. Variations in the PV module temperature result in changes in the value of R_{MPP}. If no temperature sensor is used to compensate this effect (by updating R_{MPP}), the value of R_{OP} will be fixed and equal to R_{MPP} at the nominal temperature, in the whole operating temperature range. The difference between the values given by (3.39) and (3.34) can be used to determine power variations under different temperatures. These variations are shown by simulating the system in the next section. In the case where the temperature variation is very high, or a higher power point tracking accuracy is required, a temperature sensor may be used to improve the accuracy of R_{MPP}. Another possibility is to utilize real-time I-V curve estimation, such as [109], [110], to estimate the MPP regardless of the ambient temperature.

3.5.3 Simulation Results

In this section, a PV module is studied to verify the results of the proposed MPPT technique. The PV module chosen for simulation and experiments is the *DAY4-48MC* manufactured by DAY4 Energy, Burnaby, BC, Canada. The datasheet values for this module are $I_{SC} = 8.20A$, $V_{OC} = 14.75V$, $V_{MPP} = 11.91V$, and $I_{MPP} = 7.77A$, yielding the following model.

$$I = I_{PH} - 1.32 \times 10^{-10}\left(e^{0.5934(V+0.14I)} - 1\right). \tag{3.40}$$

Using the above relation, the MPP was calculated both from simulating the power-voltage curve and finding its maximum numerically. The proposed analytical method was further used under various irradiation conditions with the results shown in Figure 3.19. In this figure, both the optimal operating point resistance (Figure 3.19a), and the PV module MPP (Figure 3.19b), are illustrated and numerical and analytical methods are compared. From this figure, the analytical results demonstrate a perfect match with numerical simulation results, and the error is always less than 0.1%.

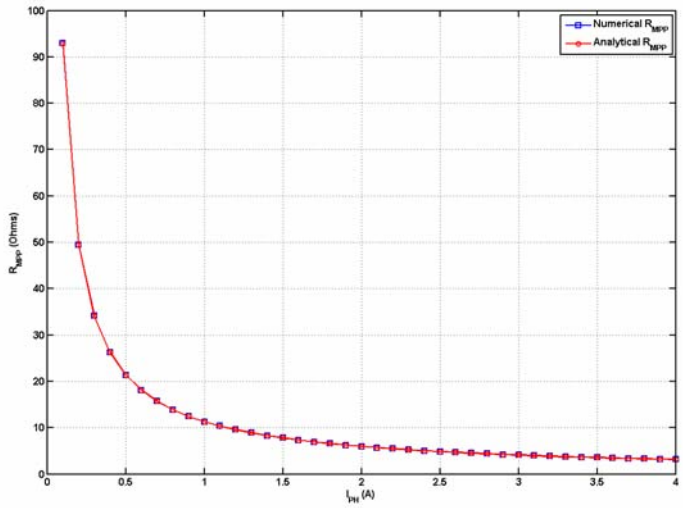

(a)

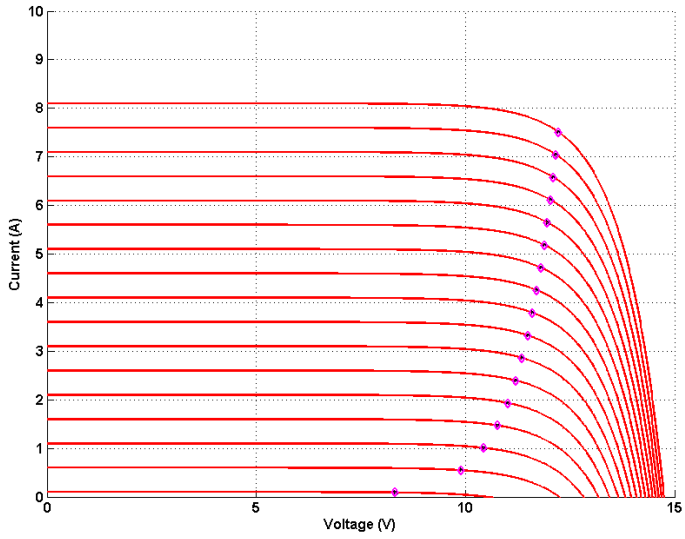

(b)

Figure 3.19: (a) Optimal operating points of the PV module in different irradiations. (b) MPP of PV module in different irradiations (Numerical and analytical methods).

To study the variations of power with respect to the ambient temperature, the module is simulated using the *SimElectronics* toolbox of the Matlab/Simulink software for temperatures between $-10°C$ to $+60°C$. Table 3.5 illustrates the results of tracking the MPP when the desired R_{MPP} is fixed at different temperatures. In this table, err is defined as follows

$$err = \frac{|P_{MPP} - P|}{P_{MPP}} \times 100. \tag{3.41}$$

The results indicate small errors in estimation of MPP for the the specified temperature variations.

Table 3.5: Simulation results indicating the effect of temperature variations.

$Irradiance = 1000\frac{W}{m^2} \rightarrow R_{MPP}\|_{T=25°C} = 1.45\,\Omega$			
$T(°C)$	$P_{MPP}(W)$	$P\|_{R=1.45}$	err
-10	98.8	96.4	2.4%
25	85.27	85.27	0%
60	71.9	70.5	1.9%
$Irradiance = 600\frac{W}{m^2} \rightarrow R_{MPP}\|_{T=25°C} = 2.42\,\Omega$			
$T(°C)$	$P_{MPP}(W)$	$P\|_{R=2.42}$	err
-10	58.9	57.3	2.7%
25	51.58	51.58	0%
60	43.3	42.45	1.9%
$Irradiance = 200\frac{W}{m^2} \rightarrow R_{MPP}\|_{T=25°C} = 7.47\,\Omega$			
$T(°C)$	$P_{MPP}(W)$	$P\|_{R=7.47}$	err
-10	21.10	19.92	2.7%
25	16.23	16.23	0%
60	15.19	14.65	1.9%

Table 3.4 shows the design specification and circuit parameters of the PV module and the DC-DC converter circuit. In the first stage of evaluating the controller performance, the PV model was simulated and subjected to abrupt changes in the irradiation levels. The irradiation changes were applied in time steps of $0.5s$, which were decreased from their maximum value to 13% of the maximum value and then increased back again.

Figure 3.20 illustrates the output power of the PV module under the proposed MPPT controller versus the actual maximum power for each irradiation condition. In Figure 3.20, a

part of the transient performance has been magnified to demonstrate the performance of the controller. The results exhibit a high tracking efficiency (99%), where the tracking efficiency, $\eta_{Tracking}$, is defined as

$$\eta_{Tracking} = \frac{P_{PV}}{P_{MPP}} \times 100 \tag{3.42}$$

in which P_{PV} is the power reached by using the proposed MPPT controller and P_{MPP} is the expected maximum power output.

Besides having a high tracking efficiency, the MPPT controller also achieves a relatively fast tracking speed of less than 0.1 seconds, which is comparable to other reported works, for example, by [111], [112], and [113].

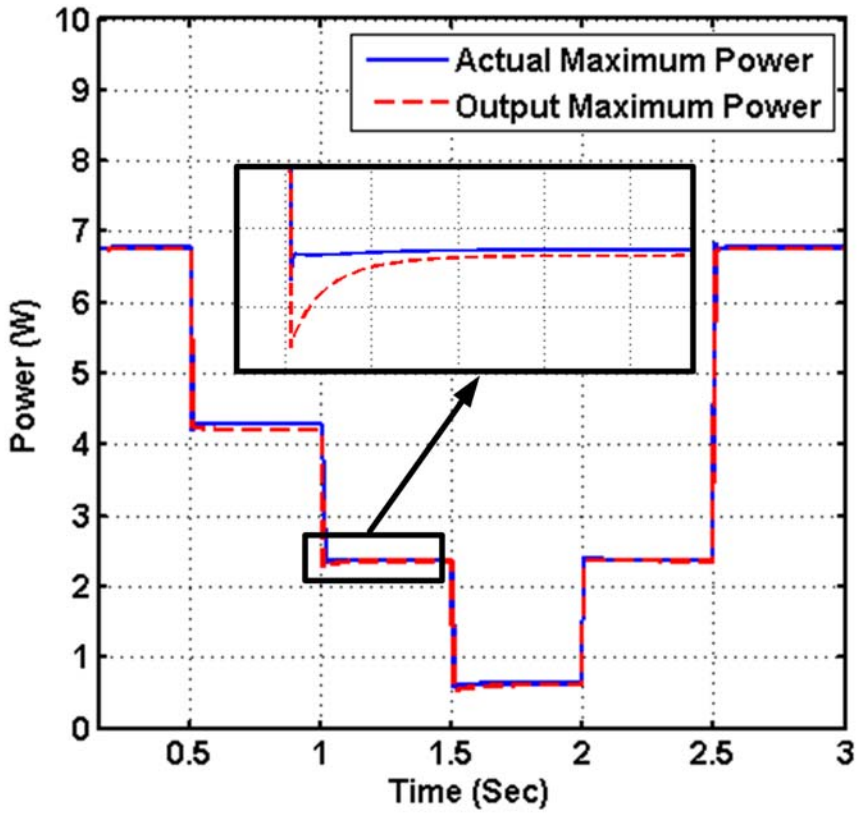

Figure 3.20: Output power of photovoltaic module versus the actual maximum power.

In the second stage of testing the performance, the robustness of the control system under variations in output battery voltage was analyzed. These simulations were done for

both abrupt changes of 5 V every 0.5 seconds, starting from 25 V, or a smooth sinusoidal signal as the battery voltage with the frequency of π rad/sec, amplitude of 20 V and bias of 45 V. Figure 3.21 demonstrate the results of these simulations, where the percentage of the output error is always less than 0.7%. The results state that the proposed method exhibits a high degree of robustness under abrupt and continuous variations in the output voltage. Performance of the proposed controller has yet to be evaluated in an experimental setting as discussed in the next section.

3.5.4 Experimental Results

To investigate the performance of the analytical MPP identification method, the PV module was subjected to various irradiations, and the VI curve of the module were approximated using the Curve Fitting Toolbox of Matlab software. Using these curves, the MPP was calculated numerically. Also, the proposed analytical method was operated on the voltage-current pairs to identify the MPP. The results are illustrated in Figure 3.22. In this figure, the PV module MPP is indicated along with the results using numerical and analytical methods. As illustrated in this figure, the analytical and numerical results for the MPP identification are very close with an error of less than 0.1%. Furthermore, the time consumed for estimation of the MPP was $400\mu s$ when using a $60MHz$ 32-bit microcontroller (TMS320F2802x). This time includes calculation time of I_{PH} and R_{MPP}.

To test the performance of the MPPT controller, an instantaneous change in irradiation level is applied to the system at time 1.3 seconds as in Figure 3.23. This change, results in a 60% decrease in the short circuit current of the PV module. Figure 3.23 depicts the results obtained using the proposed controller. Figure 3.23a illustrates the experimental and theoretical values of PV power, which indicates that the controller can compensate for sudden changes in ambient conditions and can successfully track the MPP of the system in about $0.7s$ (error less than 4%). This speed is fast, while having a reasonable accuracy, compared to similar works of [111]-[114]. Figure 3.23b demonstrates the anticipated values of the operating point under different irradiation levels, and Figure 3.23c demonstrates the actual values of the desired operating points, which is in compliance with the former figure. Finally, Figure 3.23d illustrates the working point of the system projected into P-V characteristics of the controlled PV power system. The results obtained in Figure 3.23d are very similar to the previous identification method. There is no chattering in the path of the working point and good MPPT accuracy is achieved when compared to the results discussed by [115].

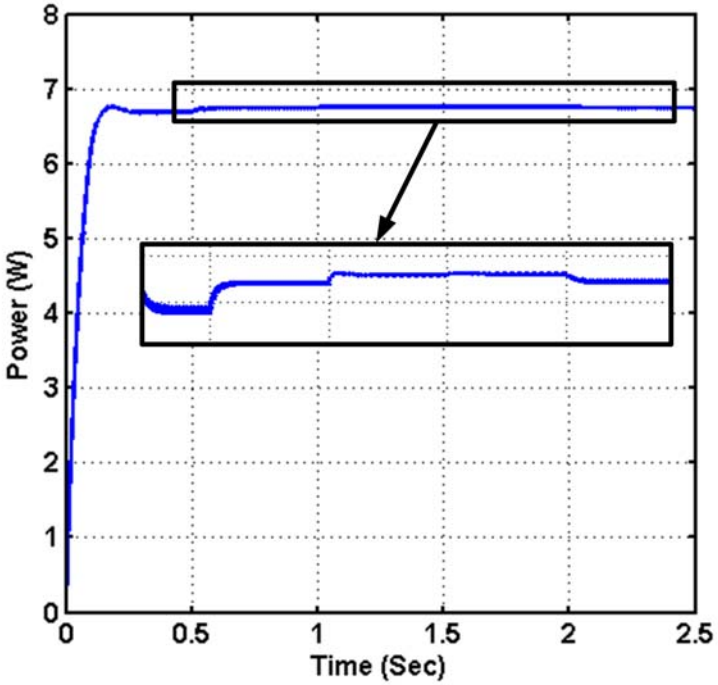

(a)

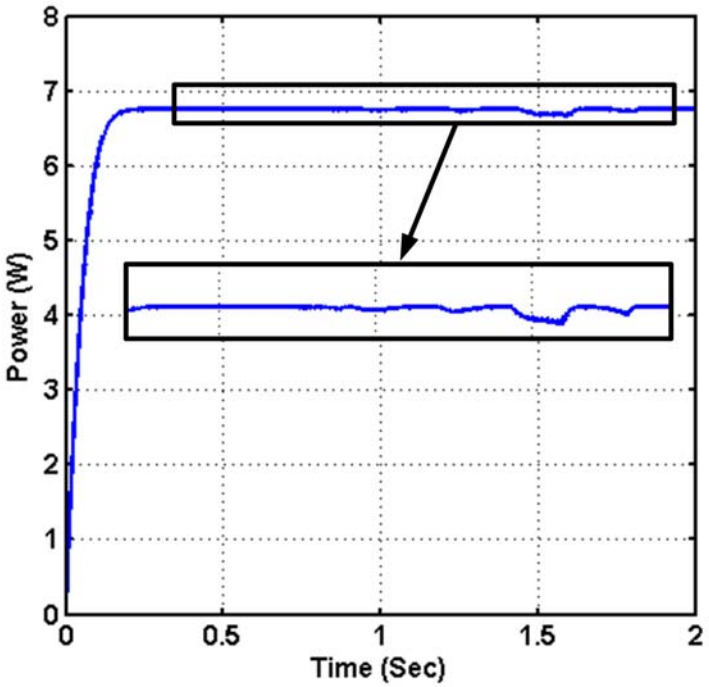

(b)

Figure 3.21: (a) Output power of the PV module under abrupt battery voltage changes. (b) Output power of PV module under sinusoidal battery voltage changes.

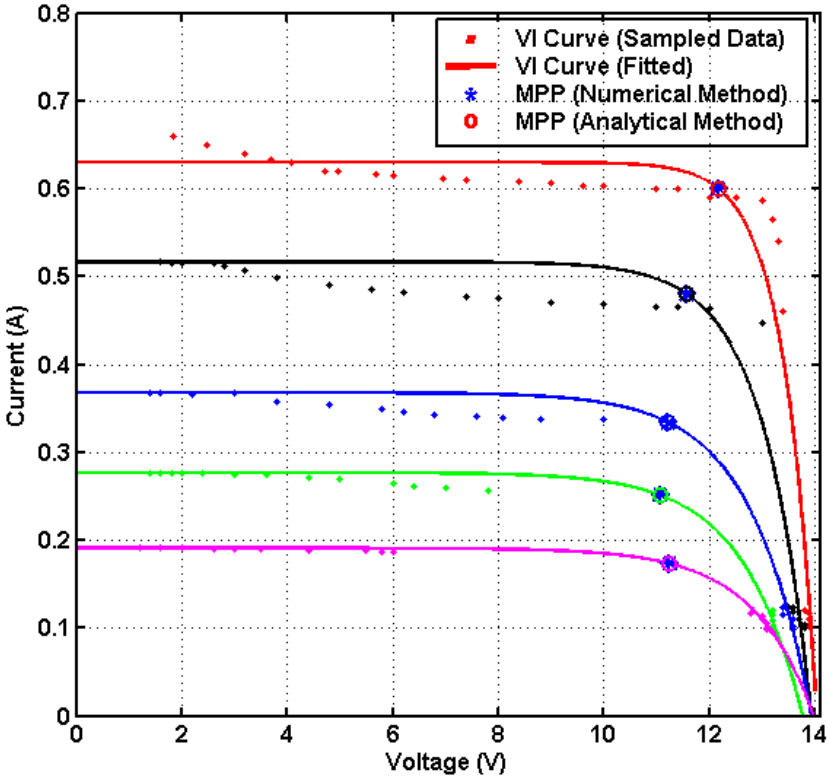

Figure 3.22: MPP of a PV module at different irradiations (numerical and analytical methods).

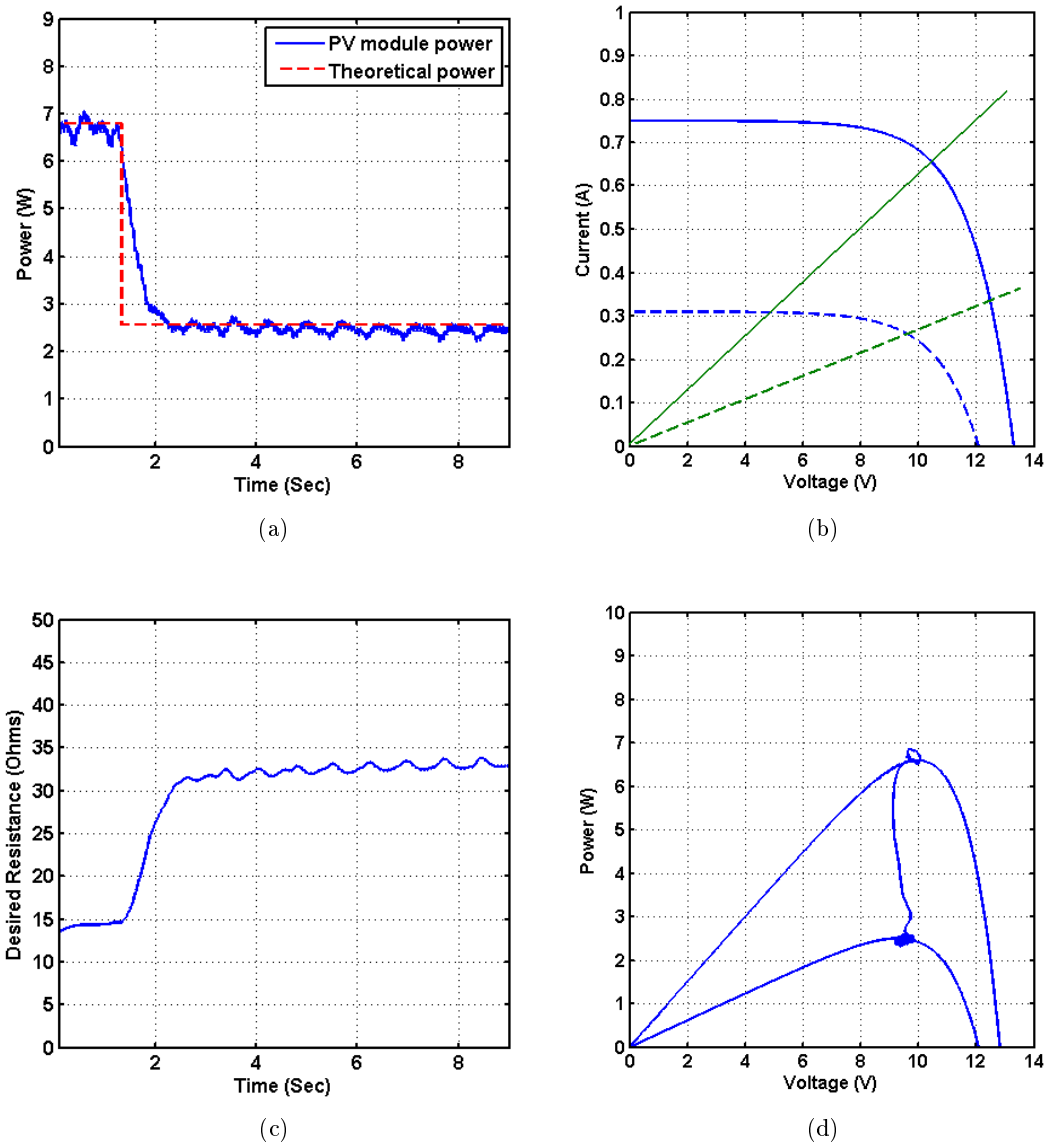

Figure 3.23: Results of the proposed MPPT method (a) Output power of the PV module. (b) PV module and desired load line curves in two different irradiance levels. (c) Desired resistance in different irradiance levels. (d) Changes in PV voltage and power.

3.6 Conclusion

This chapter proposed a number of novel MPPT methods using analytic approaches to identify the MPP of a PV module in real-time. A control scheme was developed to ensure that the MPP of the module is reached based on the pseudo-resistive behavior of the boost converter. The control performance was evaluated using numerical simulations and experiments at different irradiation levels. An average error of less than 1% for simulation and less than 5% for experimental results were achieved for tracking the MPP using the proposed feedback controller, in all of the proposed methods. Simulation and experimental results indicate that higher convergence speeds, minimum variations in the output power, and a higher degree of robustness, regardless of system parameters variations, can be achieved using the proposed controller.

Chapter 4

Control of Non-minimum Phase Load Current in a Boost Converter using Output Re-definition

Control of the output current of a boost type DC-DC converter is challenging due to the non-minimum phase characteristic between the input duty cycle and output load current and the nonlinear dynamics of the converter. This chapter presents a control strategy which utilizes the method of output re-definition combined with a nonlinear control scheme to regulate the output current of the converter when operating in CCM. The *output redefinition* concept relies on defining a new output to make the system minimum phase, or marginally minimum phase, so that a robust controller can be designed. To this end, a nonlinear feedback linearization controller is proposed based on a *circuit averaged* model of the converter. Furthermore, control in the DCM is studied and a switching scheme is presented to regulate the output current of the converter regardless of the operation mode. The control scheme can achieve small regulation errors while providing robustness due to the minimum-phase characteristic of the new output. Numerical simulations and experimental results are presented to evaluate and verify the performance of the proposed control scheme.

4.1 Boost Power Stage Dynamics

Power converters exhibit nonlinear dynamics due to the semiconductor device switching and pulse width modulation (PWM) operation. An *averaged* model of the converter is often utilized in control design [96]. The averaging methods proposed for modeling PWM converters include state-space averaging and circuit averaging. In state-space averaging, one defines the converter states depending on the on-off status of the switches and weighting the relevant linear circuit models. This method has been widely used in the literature, for example in modeling the CCM operation [73]. The second method, referred to as *circuit averaging*, utilized in this paper, is based on the average of the converter signals in a switching cycle. The latter method yields better accuracy by avoiding the approximation involved in the model weighting process [116].

Figure 4.1 depicts a boost converter connected to a resistive load. This figure is similar to the one in Figure 2.1, but the major difference is assuming a load at the output, rather than just a fixed battery voltage. Therefore, the output current control, would be a major challenging issue. The corresponding inductor current, output current, and switch voltage, are depicted in Figure 2.3 when operating in DCM and CCM, respectively. During the switch ON time, the input current can be modeled as

$$\text{ON time: } i_{in} = i_{in}(kT_s) + \frac{1}{L}\int_{kT_s}^{t} v_i \,\mathrm{d}t \tag{4.1}$$

where i_{in} is the inductor L current, v_i is the input voltage of the converter, assumed to be constant in each switching period; and k, T_s are the number of switching periods and the switching period, respectively. As depicted in Figure 2.3, in CCM the current $i_{in}(kT_s)$ has a non-zero value; however, this value is zero in DCM. Using (4.1), the input current is given by

$$i_{in}\left((k+d)T_s\right) = i_{in}(kT_s) + \frac{1}{L} v_i d T_s \tag{4.2}$$

where d is the PWM switching duty cycle.

During the OFF time of the switch, the inductor will start discharging through the load. In the discharge time interval, the input current can be written as

$$\begin{aligned} \text{OFF time: } i_{in} &= i_{in}(kT_s) \\ &+ \frac{1}{L} v_i d T_s + \frac{1}{L}\int_{(k+d)T_s}^{t} (v_i - v_o)\,\mathrm{d}t \end{aligned} \tag{4.3}$$

where v_o is the output voltage. Note that the diode voltage has been neglected in comparison with v_o.

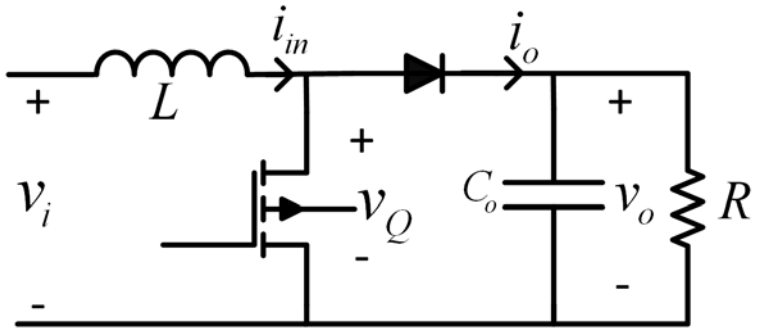

Figure 4.1: Boost converter circuit with an input voltage source.

When the converter operates in DCM, the input current reaches zero at time $(k+d+d')T_s$ as shown in Figure 2.3. This condition can be written as

$$i_{in}\left((k+d+d')T_s\right) = \frac{dT_s}{L}v_i + \frac{d'T_s}{L}(v_i - v_o) = 0. \tag{4.4}$$

Therefore, the value of d' can be calculated as follows

$$d' = \frac{v_i d}{v_o - v_i}. \tag{4.5}$$

In the CCM operation, the input current will not reach zero during the switching period. Hence, its value at the end of period is given by

$$i_{in}\left((k+1)T_s\right) = i_{in}(kT_s) + \frac{T_s}{L}v_i - \frac{(1-d)T_s}{L}v_o. \tag{4.6}$$

Thus, in DCM operation, utilization of (4.1)-(4.5) and the averaging technique [96], yields the average input current as follows

$$< i_{in} >= \frac{1}{2L}v_i d^2 T_s \left(\frac{v_o}{v_o - v_i}\right) \tag{4.7}$$

where $< . >$ denotes the averaged value of the variable. Moreover, the average of the output current can be obtained as

$$< i_o >= \frac{d^2 T_s}{2L}\left(\frac{v_i^2}{v_o - v_i}\right). \tag{4.8}$$

Equation (4.7) shows that, in DCM operation, the input current has a static and nonlinear relationship with the output voltage. A similar behavior exists for the output current given by (4.8). Using (4.1)-(4.6), the average of the output current in CCM operation can be obtained as follows

$$< i_o >= (1-d) < i_{in} > + \frac{d(1-d)T_s}{2L} v_i - \frac{d(1-d)^2 T_s}{2L} v_o. \tag{4.9}$$

Next, let us assume that the output is connected to a general RC load (Figure 4.1). Hence, the output current-voltage relationship is given by

$$< i_o >= C_o \frac{\mathrm{d} < v_o >}{\mathrm{d}t} + \frac{< v_o >}{R}. \tag{4.10}$$

Referring to Figure 4.1, since the conduction time of the diode is $(1-d)T_s$, the average of the switch voltage is given by

$$< v_Q >= (1-d) < v_o > . \tag{4.11}$$

Using (4.11), the average input voltage can be obtained as follows

$$< v_i >= L \frac{\mathrm{d} < i_{in} >}{\mathrm{d}t} + (1-d) v_o. \tag{4.12}$$

In the rest of this paper, all the formulations are based on the average values in one switching period. Hence, the notation $< . >$ will be omitted for brevity. To investigate the dynamic behavior of the converter in the CCM, one can utilize (4.9)-(4.12). After performing algebraic manipulations, the nonlinear state-space equations of the system in this mode are obtained as follows

$$\begin{cases} \dot{x}_1 = \frac{v_i}{L} - \frac{u}{L} x_2 \\ \dot{x}_2 = \frac{u}{C_o} x_1 + \frac{u(1-u)T_s}{2LC_o} v_i - \frac{u^2(1-u)T_s}{2LC_o} x_2 - \frac{x_2}{RC_o} \end{cases} \tag{4.13}$$

where $x_1 =< i_{in} >$, $x_2 =< v_o >$, and $u = 1-d$. Using (4.13), the equilibrium point of the system can be found from

$$\begin{cases} x_1^* = \frac{v_i}{u^{*2} R} \\ x_2^* = \frac{v_i}{u^*} \end{cases} \tag{4.14}$$

where the variables with the superscript $*$ indicate equilibrium quantities.

The small signal model of the dynamical system around the equilibrium point can be obtained as follows

$$\begin{cases} \dot{\tilde{x}}_1 = -\frac{u^*}{L}\tilde{x}_2 - \frac{x_2^*}{L}\tilde{u} \\ \dot{\tilde{x}}_2 = \frac{u^*}{C_o}\tilde{x}_1 + \left(\frac{{u^*}^2(u^*-1)T_s}{2LC_o} - \frac{1}{RC_o}\right)\tilde{x}_2 + \left[\frac{X_1^*}{C_o} + \frac{(1-2u^*)T_s}{2LC_o}v_i - \frac{u^*(2-3u^*)T_s}{2LC_o}X_2^*\right]\tilde{u} \end{cases} \tag{4.15}$$

where $\tilde{x}_1 = x_1 - x_1^*$, $\tilde{x}_2 = x_2 - x_2^*$, and $\tilde{u} = u - u^*$. Equation (4.15) can be further simplified by utilizing (4.14) as follows

$$\begin{bmatrix} \dot{\tilde{x}}_1 \\ \dot{\tilde{x}}_2 \end{bmatrix} = A \begin{bmatrix} \tilde{x}_1 \\ \tilde{x}_2 \end{bmatrix} + B\tilde{u} \tag{4.16}$$

where

$$A = \begin{bmatrix} 0 & -\frac{u^*}{L} \\ \frac{u^*}{C_o} & \frac{{u^*}^2(u^*-1)T_s}{2LC_o} - \frac{1}{RC_o} \end{bmatrix} \tag{4.17}$$

and

$$B = \begin{bmatrix} -\frac{x_2^*}{L} \\ \frac{x_1^*}{C_o} + \frac{(1-2u^*)T_s}{2LC_o}v_i - \frac{u^*(2-3u^*)T_s}{2LC_o}x_2^*. \end{bmatrix} \tag{4.18}$$

The transfer function of the output voltage $\tilde{x}_2$ with respect to the control input $\tilde{u}$ is obtained as follows

$$G_{ou}(s) = \frac{X_2(s)}{U(s)} = \frac{b_2 s + a_{21}b_1}{s^2 - a_{22}s - a_{12}a_{21}} \tag{4.19}$$

where a_{ij} and b_k are the elements of matrices A and B in (4.17) and (4.18), respectively. Since $0 < u^* < 1$, the terms $a_{12} = -\frac{u^*}{L}$, $a_{22} = \frac{{u^*}^2(u^*-1)T_s}{2LC_o} - \frac{1}{RC_o}$, and $b_1 = -\frac{x_2^*}{L}$ are always negative, while $a_{21} = \frac{u^*}{C_o}$ is always positive. Besides, for practical circuit values, $b_2 = \frac{x_1^*}{C_o} + \frac{(1-2u^*)T_s}{2LC_o}v_i - \frac{u^*(2-3u^*)T_s}{2LC_o}x_2^*$ is positive. The sign change in the numerator polynomial coefficients of the output voltage transfer function G_{ou} indicates the existence of a RHP zero, i.e., NMP behavior of the boost converter operating in the CCM. Furthermore, the transfer function between the output current and the control input has a RHP zero.

It is well known that tracking control of a non-minimum phase system may result in instability of its internal dynamics (see [117]-[118]). Output re-definition, utilized in control of flexible structure robotic systems [86, 87], can be used to alleviate the problem. This method relies on re-defining the output of the system to a new output that is close to the

desired output but can render a minimum-phase input-output characteristic. In this work, we extend the concept to control the output of boost converters. To this end, the output of the system is defined as a linear combination of the output current and input current such that the system becomes minimum phase or marginally minimum phase. To this end, let us re-define the output of the system as follows

$$y = (1-\beta)i_{in} + \beta i_o \tag{4.20}$$

where the value of β is used to transform the NMP system into a minimum-phase one. Note that choosing $\beta = 1$ results in the original NMP system, whereas $\beta = 0$ results in a minimum-phase system. A range for β values to yield a minimum-phase characteristic can be obtained by utilizing (4.13) and rewriting (4.20) as follows

$$\begin{aligned} y &= (1+\beta(u-1))x_1 + u(1-u)\beta\frac{T_s}{2L}v_i \\ &- u^2(1-u)\beta\frac{T_s}{2L}x_2. \end{aligned} \tag{4.21}$$

Referring to (4.21), the output is given by

$$\begin{aligned} \tilde{y} &= (1+\beta(u^*-1))\tilde{x_1} - \left(u^{*^2}(1-u^*)\beta\frac{T_s}{2L}\right)\tilde{x_2} \\ &+ \beta v_i\left(\frac{1}{u^{*^2}R} + \frac{T_s(u^*-1)}{2L}\right)\tilde{u} \end{aligned} \tag{4.22}$$

where $\tilde{y} = y - y^*$. Rewriting (4.22), we have

$$\tilde{y} = C\begin{bmatrix}\tilde{x}_1 \\ \tilde{x}_2\end{bmatrix} + D\tilde{u} \tag{4.23}$$

where

$$C = \begin{bmatrix}1+\beta(u^*-1) & -\left(u^{*^2}(1-u^*)\beta\frac{T_s}{2L}\right)\end{bmatrix} \tag{4.24}$$

and

$$D = \beta v_i\left(\frac{1}{u^{*^2}R} + \frac{T_s(u^*-1)}{2L}\right). \tag{4.25}$$

Since matrix A given by (4.17) does not change due to the re-definition, the eigenvalues of the system are in the same place as before. However, the numerator of the transfer function

from u to the output current is changed due to the re-defined output. The zeros of the system are calculated from the roots of the following equation

$$D\,s^2 + (b_1c_1 - Da_{22} + c_2b_2)\,s + (c_1b_2a_{12} - c_1b_1a_{22} + c_2b_1a_{21} - Da_{12}a_{21}) = 0. \tag{4.26}$$

where c_k are the elements of the C matrix in (4.24).

Analysis of the roots of (4.26) using MATLAB software for different values of circuit parameters demonstrates that in CCM operation, the value of β is a key factor in determining whether the system is minimum-phase (MP) or not. In particular, if β is chosen close to zero, the system will be minimum phase. However, the desired values of β should be close to 1 so that the re-defined output is close to the desired output. An analysis of the roots of (4.26) demonstrates that the values of β for which the system changes its characteristics between NMP and MP, is highly dependent on the value of u^*. The analysis suggests that smaller values of u^* would result in smaller values of β. Therefore, to ensure the internal stability of the system, the value of β should be chosen large enough such that the system remains in the minimum phase region. Furthermore, if $\beta \gg 1$, the value of $(1-\beta)i_{in}$ cannot be neglected with respect to βi_o in (4.20). In the steady state CCM operation, the value of inductor current will be approximately $\frac{1}{u}i_o$, for which u is relatively small. Therefore, the effect of $(1-\beta)i_{in}$ would be negligible if u is increased. As a result of increasing u, the NMP region for β is increased and the controller may possibly cross the boundary into the NMP region during a transient process. Utilizing different values of u^* and studying their effect on β shows that the value of $(1-\beta)i_{in}$ cannot be neglected with respect to βi_o in the CCM. This effect will be considered in designing the controller in section 4.2.

4.2 Nonlinear Controller Design

Based on the expression for output current, a controller is presented in this section to track a desired output, i.e., the redefined load current, under CCM and DCM operating conditions. The controller structure is shown in Figure 4.2, consisting of a PI controller to assure convergence of the error to zero. The nonlinear control block is a feedback linearization controller obtained as follows. Referring to Figure 4.2, w is defined as

$$w = k_p(y_d - y) + k_i \int (y_d - y)dt \tag{4.27}$$

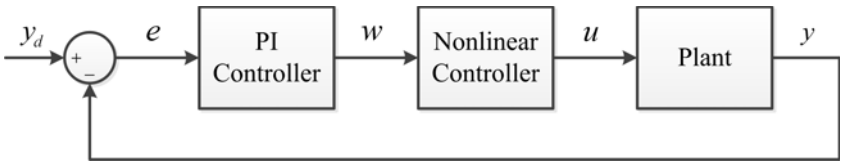

Figure 4.2: System schematic using the nonlinear controller.

where y_d is the desired output of the system.

Let us choose a control input u such that the closed loop relationship is given by

$$y = w + y_d. \tag{4.28}$$

Hence, the closed-loop error, $e = y_d - y$, can be obtained as

$$(k_p + 1)\dot{e} + k_i e = 0 \tag{4.29}$$

which indicates exponential convergence of the error to zero.

To define a proper control input u to enforce (4.28), one needs to individually define the output of the plant under each operating condition. In DCM operation, let us rename the output current of the system to $y = i_o$ in (4.8). Hence the output can be obtained as follows

$$y = \frac{(1-u)^2 T_s}{2L}\left(\frac{v_i^2}{v_o - v_i}\right). \tag{4.30}$$

Referring to (4.30) and choosing the control input u as

$$u = 1 - \sqrt{\frac{2L}{v_i^2 T_s}(w + y_d)(v_o - v_i)} \tag{4.31}$$

will result in the closed loop relationship given by (4.28). Therefore, the error will converge to zero, exponentially.

In the CCM operation, a trade-off should be sought between the value of u^* and β to ensure system stability and small errors. In particular, larger values of β decrease the risk of internal instability, but increase the effect of input current in the redefined output formula (4.20). Since the control objective is to track a desired output current, the effect of input current will appear as an error term in the output current. To solve this issue, one approach is to approximate the desired input current and utilize it to update the desired output. Using

the above approach, the desired output of the system can be re-defined as

$$y_d = \beta i_{od} + (1-\beta) i_{in_d} = \beta i_{od} + (1-\beta)\frac{R i_{od}^2}{\eta v_i} \tag{4.32}$$

where η is a parameter equal to the power conversion efficiency of the converter. Furthermore, it is assumed that η is known and can be tuned, or updated on-line, based on the input and output power, voltage, and current measurements. Furthermore, in (4.32), the subscript d denotes the desired value of a variable.

Using (4.13) and (4.21), the output can be re-written as

$$y \;\; = \;\; (1+\beta(u-1))x_1 + u(1-u)\beta\frac{T_s}{2}\dot{x}_1. \tag{4.33}$$

Since $0 < u \ll 1$ in CCM operation, u^2 is negligible with respect to u. Using the Taylor's series expansion, we have

$$y = (1+\beta(u-1))x_1 + \left(u(1-2u^*) + u^{*^2}\right)\beta\frac{T_s}{2}\dot{x}_1. \tag{4.34}$$

Figure 4.3 demonstrates the approximation error for the term $u(1-u)$. Based on this figure, the value of u^2 can not be completely neglected; hence, a Taylor series expansion is used here, instead.

Referring to (4.28), a control input to ensure the exponential convergence of the closed-loop error to zero is given by

$$u = \frac{w + y_d - \left((1-\beta)x_1 + u^{*^2}\beta\frac{T_s}{2}\dot{x}_1\right)}{\beta\left(x_1 + (1-2u^*)\frac{T_s}{2}\dot{x}_1\right)}. \tag{4.35}$$

It should be noted that utilizing the approximate input (4.35) versus solving the quadratic equation (4.34) provides a trade-off between larger approximation errors and computational cost of the algorithm. Furthermore, the feedback system loop-gain would compensate for the errors in the input including the approximation in (4.34).

4.3 Convergence Analysis for CCM Controller

In section 4.2, it was shown that the proposed controller for CCM, results in exponential convergence of the error to zero. However, zero error between re-defined output and its desired value in steady state may not necessarily guarantee zero error between output current

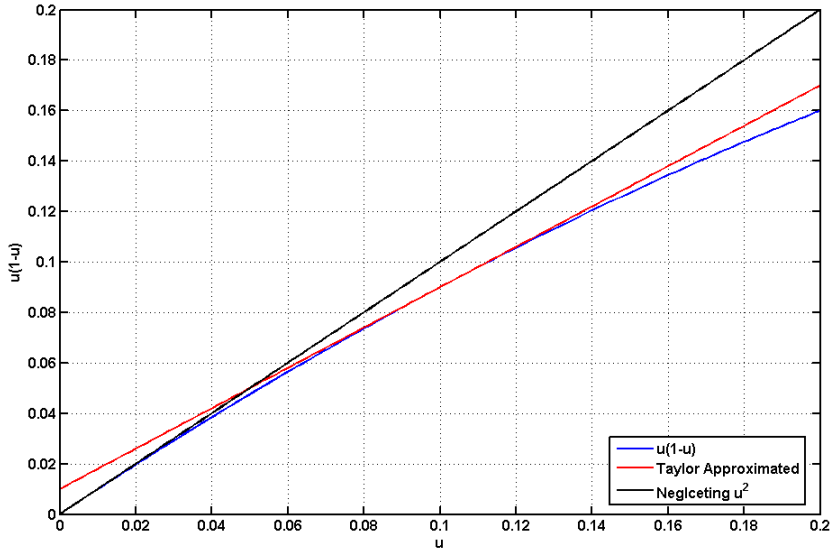

Figure 4.3: Approximation error for $u(1-u)$.

and its desired value. This issue is verified in the following by studying the operational conditions of the boost converter in CCM.

Utilizing (4.20) and (4.32) in the steady state, when $e = 0$, i.e., $y \to y_d$, the relationship between the steady state value of the output current and its desired value can be obtained as

$$(1-\beta)\frac{i_{o_{ss}}}{\eta u_{ss}} + \beta i_{o_{ss}} = \beta i_{od} + (1-\beta)\frac{Ri_{od}^2}{\eta v_i} \tag{4.36}$$

where the subscripts d and ss determine the desired and steady state values, respectively. Also, let us assume that the output current does not converge to its desired value, i.e., $i_{o_{ss}} = i_{od} + \Delta i_o$. Note that as $i_{o_{ss}} = i_{od} + \Delta i_o > 0$, Δi_o is always greater than $-i_{od}$. Therefore, the output voltage can be obtained as

$$v_{o_{ss}} = Ri_{od} + R\Delta i_o. \tag{4.37}$$

Utilizing (4.37) and $v_i = u_{ss} v_{o_{ss}}$, the following relationship can be obtained.

$$\frac{1}{u_{ss}} = \frac{Ri_{od}}{v_i} + \frac{R\Delta i_o}{v_i}. \tag{4.38}$$

Utilizing (4.38) and (4.36), we have

$$R(1-\beta)\Delta i_o^2 + (2R(1-\beta)i_{od} + \beta\eta v_i)\,\Delta i_o = 0. \tag{4.39}$$

The trivial solution of (4.39) is $\Delta i_o = 0$, which leads to $i_{o_{ss}} = i_{od}$, indicating that the output current converges to its desired value in the steady state. However, the second solution of (4.39) is given by

$$\Delta i_o = \frac{\beta\eta v_i}{(\beta-1)R} - 2i_{od}. \tag{4.40}$$

To ensure that $i_{o_{ss}} = i_{od}$ is the only solution under all operating conditions, the parameters of the system should be chosen such that the second solution (4.40) is not feasible. Since $\Delta i_o > -i_{od}$ and referring to (4.40), this condition is met when the following inequality is valid

$$i_{od} > \frac{\beta\eta v_i}{(\beta-1)R}. \tag{4.41}$$

Furthermore, when the converter is operating in CCM, the steady state output voltage should be larger than the input voltage multiplied by $\frac{1}{1-d_B}$, where d_B is the duty cycle of the converter at the DCM/CCM boundary. Therefore, the value of i_{od} should be chosen to satisfy the following inequality

$$\frac{v_i}{R(1-d_B)} < i_{od}. \tag{4.42}$$

Combining inequalities (4.41) and (4.42), the boundary value of β to ensure that (4.40) is not a solution, can be obtained as

$$\frac{1-d_B}{1-d_B-\eta} < \beta \tag{4.43}$$

which is a weaker constraint for β than the constraint to remain in the minimum phase region.

4.4 Combination of the CCM and DCM Controllers

In section 4.2, two different controller structures were presented for operation in DCM and CCM, respectively. To combine the two controllers, a switching algorithm is required based on the desired outputs of the system and the boundary condition between the two modes of

operation. Figure 4.4 depicts the input current waveform at DCM/CCM boundary. Referring to Figure 4.4 and (4.1), when the converter is operating in the boundary point between DCM and CCM, the maximum value of the input current $i_{in_{max}}$, is given by

$$i_{in_{max}} = \frac{v_i d_B T_s}{L} \tag{4.44}$$

where d_B is the duty cycle at the boundary point between DCM and CCM. Utilizing $i_{in_{max}}$, the average value of the input current i_{in_B} in the boundary mode is given by

$$i_{in_B} = \frac{v_i d_B T_s}{2L}. \tag{4.45}$$

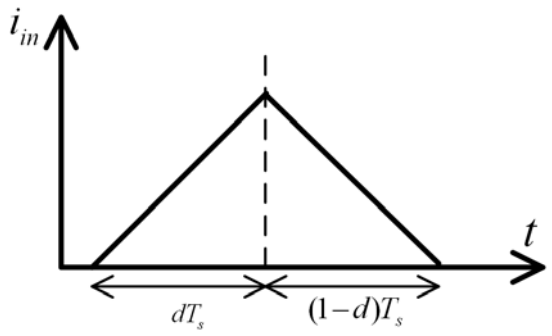

Figure 4.4: Input current at DCM/CCM boundary.

In the steady state, $v_i = v_{o_B}(1 - d_B)$ and $i_{o_B} = i_{in_B}(1 - d_B)$, where i_{o_B} and v_{o_B} are the average values of output current and voltage in the boundary mode, respectively. Therefore, the average value of the output current is given by

$$i_{o_B} = \frac{v_{o_B} d_B (1 - d_B)^2 T_s}{2L}. \tag{4.46}$$

Now using $R = \frac{v_{o_B}}{i_{o_B}}$, the boundary mode duty cycle can be obtained by solving the following constrained equation

$$d_B(1 - d_B)^2 = \frac{2L}{RT_s}, \;\; 0 < d_B < 1. \tag{4.47}$$

Equation (4.47) is utilized in the design of the switching scheme. To this end, let us use the following linearized approximation

$$d_B(1 - d_B)^2 \approx -0.264 d_B + 0.25 \tag{4.48}$$

where the numerical coefficients were found using the Curve Fitting Toolbox of Matlab. Figure 4.5 demonstrates the accuracy of this approximation. Substituting (4.48) into (4.47), and using circuit parameters, the value of boundary duty cycle, d_B, can be obtained.

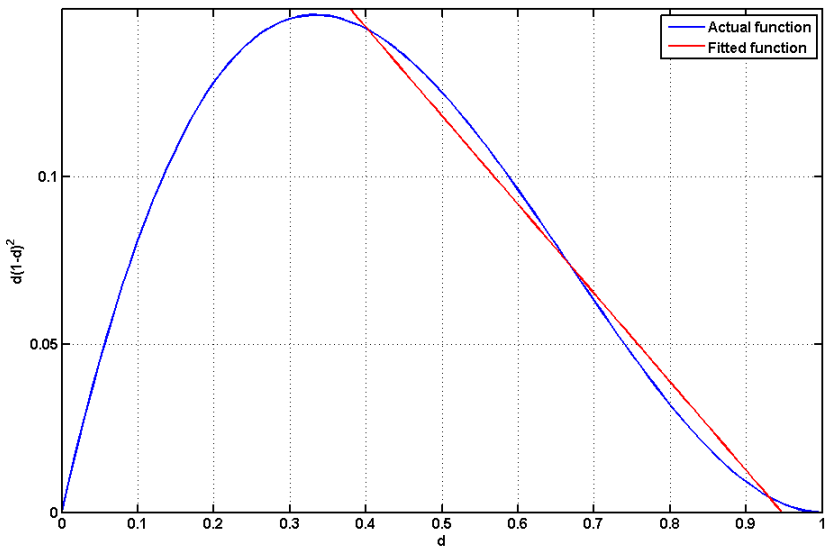

Figure 4.5: Approximation of the boundary duty cycle.

Note that, fitting errors have an effect on the accuracy of the switching function just at the boundary between CCM and DCM, which can be minimized by adding to computational complexity of the system and changing the approximation in (4.48). As one of the issues for designing the control system was to minimize its computational complexity a simple approximation has been proposed (first order polynomial); although, by tolerating an error at the boundary point. However, for increasing the accuracy, the following Gaussian approximation can be used as well, which decreases the mean error by %50, while adding to the complexity of the system. A comparison of the different fitting functions is demonstrated in Figure 4.6.

$$d_B(1-d_B)^2 \approx 0.1387 \exp -(\frac{d_B - 0.4075}{0.3197})^2 \tag{4.49}$$

Using the boundary duty cycle, the value of output voltage is given by

$$v_{o_B} = \frac{v_i}{1-d_B}. \tag{4.50}$$

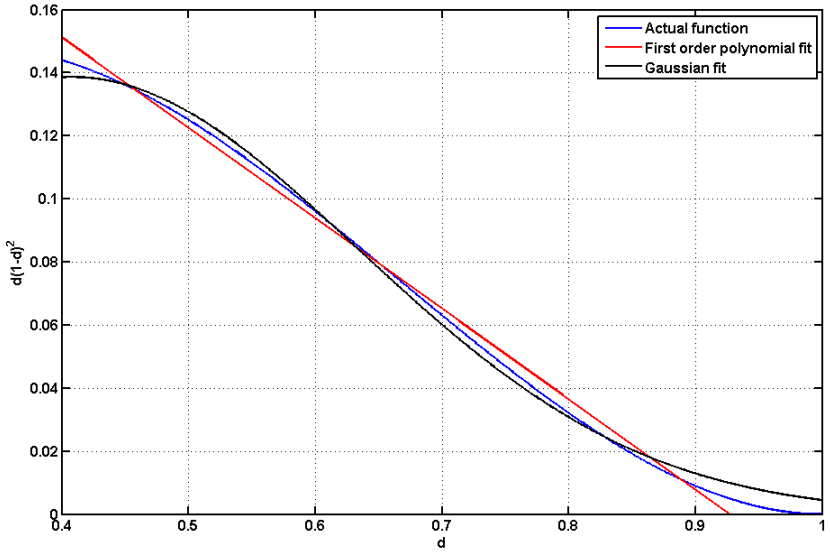

Figure 4.6: Approximation of the third order function and fitting errors.

Furthermore, since the steady state average current of the output capacitor reaches zero, the output voltage can be obtained by a knowledge of the desired output current and load resistance. Hence, the boundary value of the output current can be obtained based on the load resistance and (4.50) as follows

$$i_{o_B} = \frac{v_{o_B}}{R}. \tag{4.51}$$

Utilizing (4.47)-(4.51), the following limit for the desired output current to remain in CCM is obtained

$$i_{o_{min}} \approx \frac{v_i}{0.053R + \frac{7.5758L}{T_s}}. \tag{4.52}$$

Thus, the controller switching scheme is obtained as follows. By utilizing the numerical values of input voltage and load resistance, if the desired input current is more than $i_{o_{min}}$ in (4.52), the CCM controller is selected; otherwise, the DCM controller is selected.

4.5 Simulation and Experimental Results

The parameters of the system used in simulation studies are shown in Table 4.1. In the first step, the root locus of the zeros of the system was utilized to study the system for different values of u^* and β, as shown in Figure 4.7. By increasing β, the zeros move to the left-half plane, mainly because of the dominance of the input current in the corresponding relationship, i.e., (4.20). For instance, in Figure 4.7a, when $u^* = 0.05$, a value of $\beta = 1.02$ is required for operation between the non-minimum and minimum phase boundary. However, $\beta = 1.3$ when $u^* = 0.25$. Based on the discussion in section 4.2, the value of β should be chosen large enough to avoid reaching the non-minimum phase region in order to maintain internal stability of the states.

Table 4.1: Boost converter circuit parameters.

Parameter	**Value**
Input voltage, v_i	2 V
Inductance, L	0.1 mH
Load	100 Ω
Output capacitance	200 μF
Switching frequency	10 kHz

In the next step, the controller was simulated using the SimPower Systems Toolbox in the MATLAB/Simulink environment. Figure 4.8 demonstrates the results of the controller implementation for the converter operating in DCM. Figure 4.8a illustrates the controller performance due to an abrupt change in the desired output current, i.e., a step change from $0.15A$ to $0.3A$ at $t = 0.1s$. Figure 4.8b shows the results due to an instantaneous change in the input voltage at $t = 0.1s$. These and other similar tests demonstrate the robustness of proposed controller and its ability to quickly track a desired output current while achieving small errors in DCM operation. In particular, the settling time of the proposed controller for DCM operation, is less than $3ms$ in response to 50% variations in the desired current or input voltage parameters.

The results of the CCM controller indicate that, as long as the value of β ensures minimum phase conditions, the controller is able to stabilize the system and track the desired output. Similar to DCM operation, the performance of the controller was tested in response to sudden changes in the operating conditions when $\beta = 1.25$. In the first test, the desired

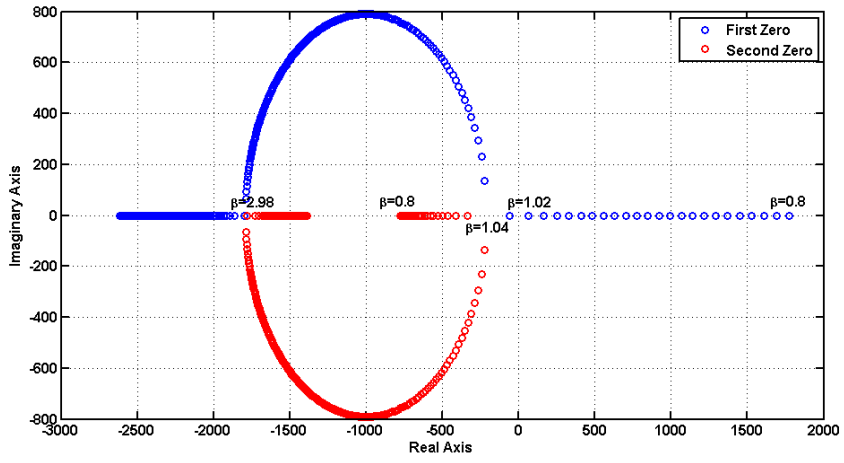

(a)

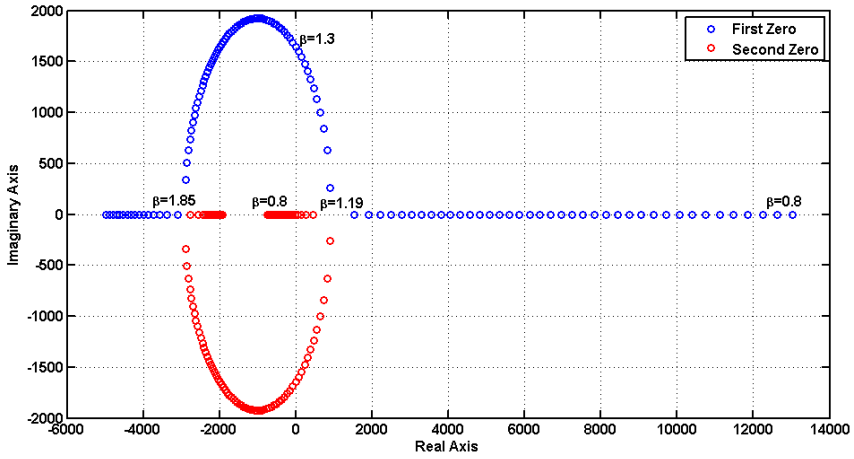

(b)

Figure 4.7: Root locus of system zeros for different values of β: (a) $u^* = 0.05$, (b) $u^* = 0.25$.

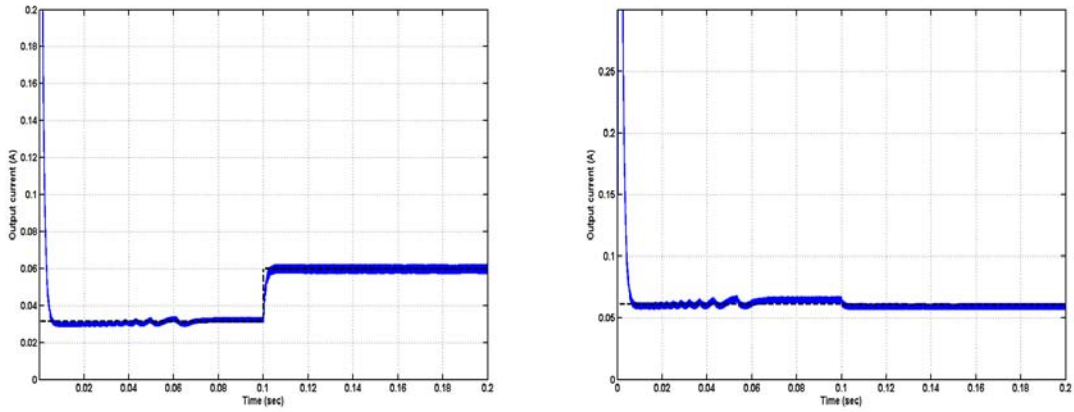

(a) (b)

Figure 4.8: Output current in DCM in response to a sudden change in (a) Desired output current (desired current: – –, circuit current: —), (b) Input voltage.

output current drops to 50% of its initial value. In the second test, the input voltage increases suddenly to 1.5 times of its initial value. Figure 4.9 demonstrates the results of the controller which clearly show that the error converges to zero with a relatively high speed and accuracy. The settling time for the proposed controller in CCM operation is less than 10 milliseconds for sudden 50% change in desired output current or input voltage, which is comparable to other suggested controllers in [73]-[76].

In the final step of simulation, a hybrid algorithm was tested by integrating the CCM and DCM controllers for regulating the desired output current. Figure 4.10 demonstrates the performance of the hybrid controller. In this figure, as well as in Figure 4.9, an overshoot behavior is observed for operation in CCM. As Figure 4.7 illustrates, the system has a dominant pair of complex conjugate poles which results in the overshoot behavior. This behavior is also observable in the experimental results depicted in Fig. 13. The above tests indicate that the switching controller is able to track the desired output current with a reasonable performance regardless of the mode of operation.

To experimentally verify the effectiveness of the proposed controller, the control system was implemented using a dSPACE system (DSP1103). The controller was built in the Matlab/Simulink environment with the C code generated using the Real-Time Workshop Toolbox. The parameters of the implemented boost converter circuit were chosen similar to the ones in Table 4.1. A value of $\eta = 86\%$ was utilized based on off-line measurements prior to

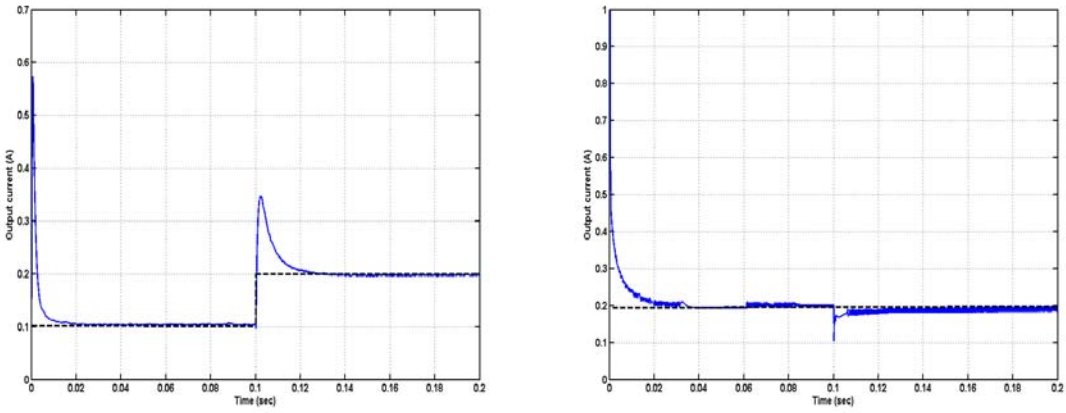

(a) (b)

Figure 4.9: Output current in CCM in response to a sudden change in (a) Desired output current (desired current: – –, circuit current: —), (b) Input voltage.

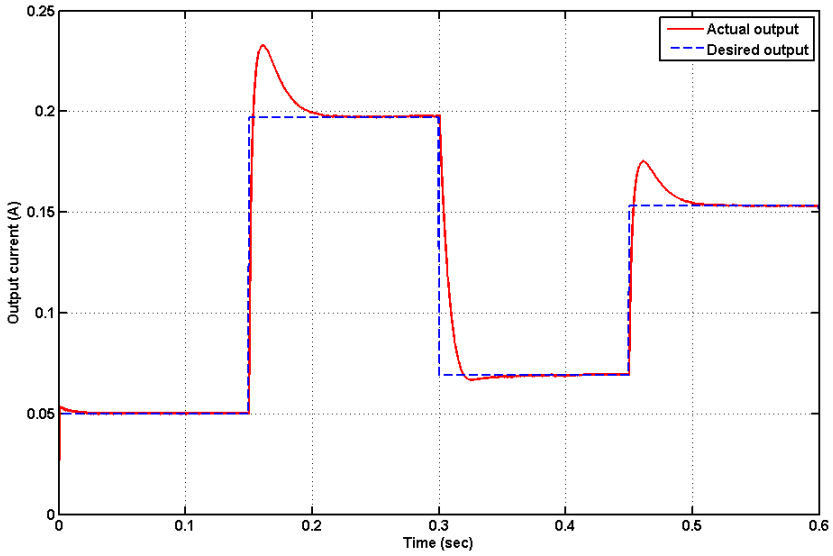

Figure 4.10: Desired and actual output currents using the combination algorithm.

the experiment, by applying 10 different input voltages in the operating range of the converter and measuring input and output currents/voltages and calculating the corresponding power levels. Two sense resistors, 0.1Ω and 0.5Ω, were used to measure input and output currents of the converter, respectively. The dSPACE system used in the experiments had an A/D conversion speed of 800ns which is negligible compared to the control loop period. Also, the PWM signal output was directly generated using the dSPACE system; hence, no D/A was used in the experiments.

Increasing the switching frequency will result in decreasing the ripples in the current. However, increasing the switching frequency can be hampered by other issues when using the averaging technique. This is due to the fact that the controller has to sense the changes in the current waveform at a much higher rate than the input waveform; hence, requiring a relatively high sampling frequency. Due to the limitation of the real-time environment used in our study (dSPACE system DSP1103), the switching frequency was set to 10 kHz. However, increasing the switching frequency is possible if a faster real-time environment is utilized.

In the first step, the DCM and CCM controllers were tested individually, with step changes in the input voltage. Figure 4.11 shows the output current of the boost converter. In both cases, a 30% increase and decrease was applied to the input voltage at two different times. This test demonstrates the ability of the controller to compensate for sudden input variations, while tracking a desired output current. The convergence speed of the controller in both cases is about 0.2 seconds.

To demonstrate the advantage of the output re-definition approach, Figure 4.12 illustrates the control input, i.e., duty cycle, and the output current, utilizing the feedback linearization controller without using the output redefinition technique. Since the system is NMP, the closed-loop system will be unstable as seen by the control input in Figure 4.12a. Furthermore, by utilizing (4.47) the PWM duty cycle is limited to 85% to ensure operation in CCM. Hence, the output current will not become unbounded and will be limited to the boundary value between CCM and DCM. The effect of estimating the desired output as in (4.32), is shown in Figure 4.13. In this experiment, the effect of the second term of (4.32), i.e., the estimated desired input current, was reduced to 80% of its value, while the desired output current remained constant. In this case, the feedback controller can still control the system and avoid instability; however, the steady state error is increased.

In the last experiment, the hybrid controller was implemented and tested by applying

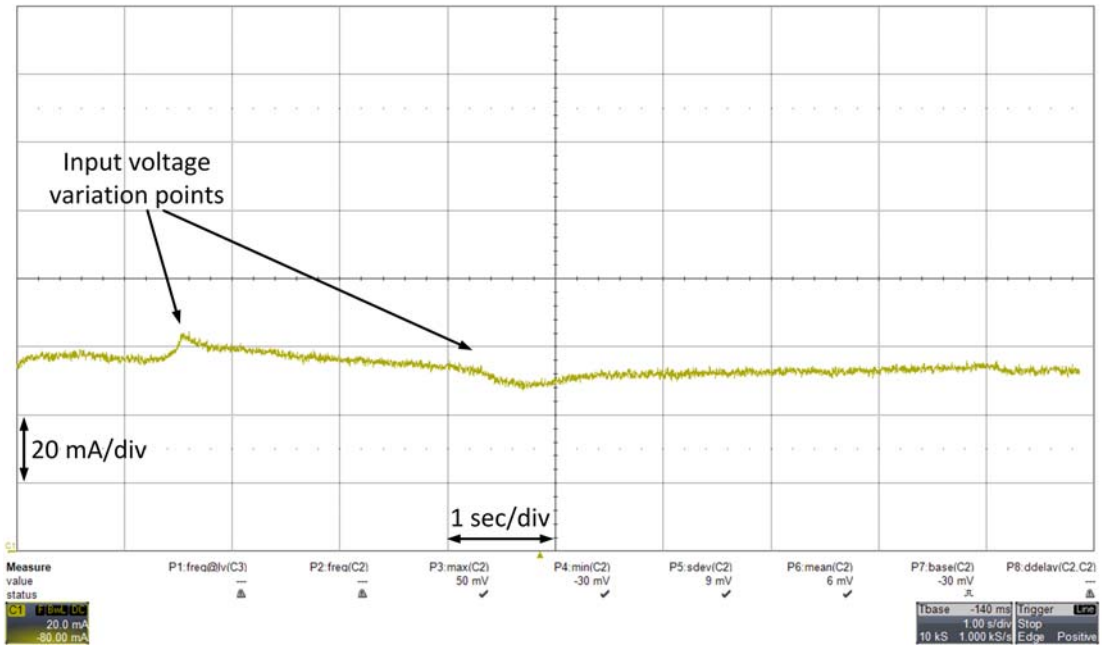

(a)

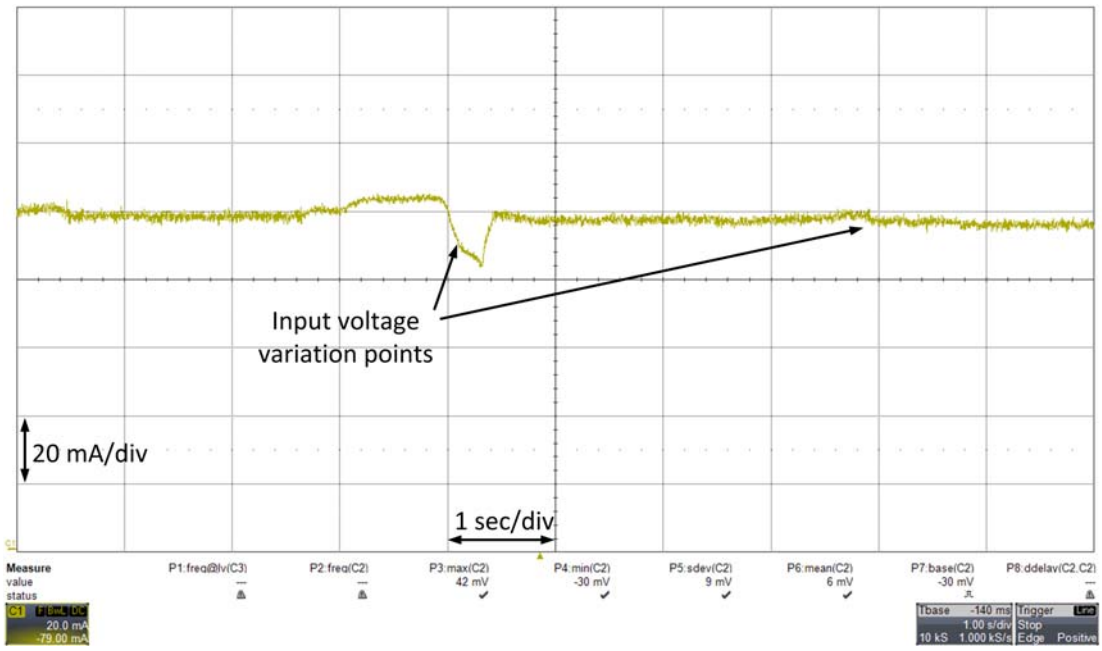

(b)

Figure 4.11: Output current of the converter in the presence of 30% instantaneous change in input voltage. (a) DCM, (b) CCM.

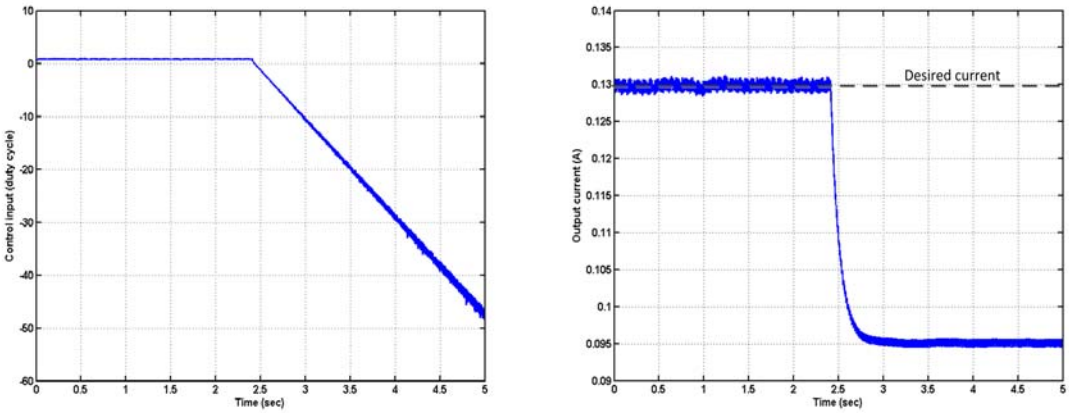

(a) (b)

Figure 4.12: De-stabilization effect when not using the output re-definition technique: (a) Control input (duty cycle), (b) Output current.

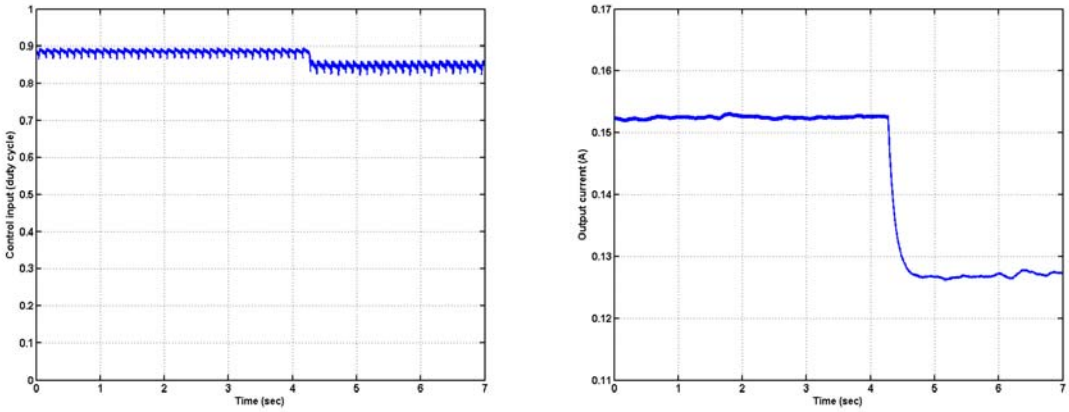

(a) (b)

Figure 4.13: Effect of changing the desired re-defined output on the steady state error: (a) Control input (duty cycle), (b) output current.

instantaneous changes in the reference output current. The above changes were applied such that the system moves from DCM to CCM and then back to DCM operation. The results are shown in Figure 4.14, which indicate that the switching controller can quickly track the reference output current regardless of the conduction mode of the converter.

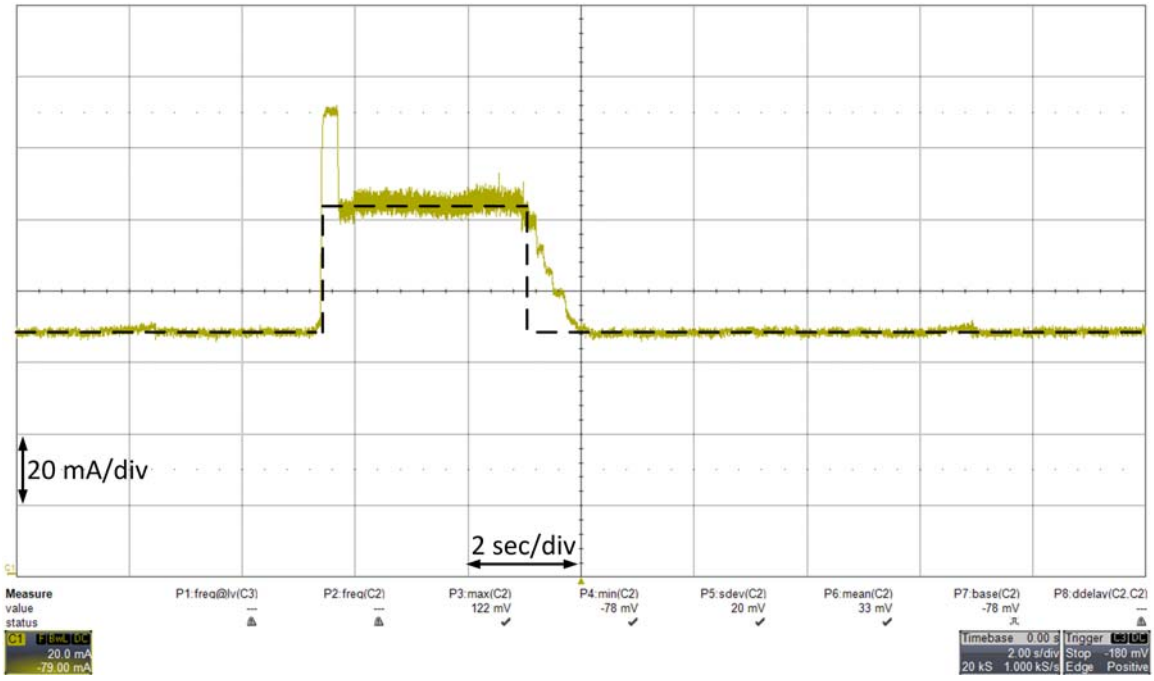

Figure 4.14: Output current of the converter using the switching controller (desired current: – –, circuit current: —).

4.6 Conclusion

In this chapter, a nonlinear model of a boost converter was presented using the circuit averaging method for DCM and CCM operation. The latter method was utilized due to its better accuracy when compared to state-space averaging models. Based on the nonlinear models, two controllers were designed to track a desired output load current. The proposed control scheme is based on a combination of the feedback linearization method and the concept of output re-definition to overcome the non-minimum phase characteristic of the boost converter. The DCM and CCM controllers were further merged to form a hybrid

controller for tracking a desired output regardless of the conduction mode of the converter. Integration of the two controllers enables the circuit to be used in a wide range of input power. Simulation and experimental results were presented to illustrate the performance of the proposed controller and its effectiveness in terms of providing stability and small errors.

Chapter 5

Control of a 3-Phase Bidirectional Converter with Application in Regenerative Suspension

In this chapter, the development of a novel control strategy for a 3-phase bidirectional converter and its application in an energy regenerative suspension mechanism are discussed. The semi-active suspension system consists of a mass-spring unit coupled with a linear permanent magnet machine or a rotary machine cascaded with a 3-phase bidirectional converter connected to a battery. For the case where a linear machine is used, a skyhook controller is developed to provide energy transfer from the suspension system to the battery. For the case where a rotary machine is used, the performance of the controller is verified by connecting the linearly vibrating system to the rotary machine through a linear to rotary conversion mechanism. Enforcing a resistive behavior across the electric machine terminals produces the same effect as controlling the mechanical damping of the suspension system. To this end, a sliding mode control approach is utilized to design a controller for the system. Numerical simulation and experimental results are presented that demonstrate the performance of the proposed control strategy.

5.1 Boost Power Stage Dynamics

The three-phase bridgeless boost converter considered in this work is demonstrated in Figure 5.1. It is assumed that switches Q_1, Q_2, and Q_3 are controlled by u_a, u_b, and u_c, respectively. The other 3 switches, $Q_4 - Q_6$ are switching with the inverse signals. In other words, if switch Q_j is ON, switch Q_{j+3} will be OFF, and vice versa, where $j \in \{1, 2, 3\}$. Based on the conduction state of each switch, the circuit can have eight different modes. Analyzing different modes enables us to derive the analytical model of the circuit as follows.

a) $Q_1 - Q_3$ are OFF: If $Q_1 - Q_3$ are OFF, the circuit is operated as in Figure 5.2a. Utilizing Kirchhoff's circuit laws, the dynamics of the circuit in this mode of operation are as follows

$$\begin{cases} \frac{di_a}{dt} = \frac{1}{3L}(2v_a - v_b - v_c) \\ \frac{di_b}{dt} = \frac{1}{3L}(-v_a + 2v_b - v_c) \\ \frac{di_c}{dt} = \frac{1}{3L}(-v_a - v_b + 2v_c) \end{cases} \tag{5.1}$$

where i_p and v_p are the phase current and voltage, respectively, in which $p \in \{a, b, c\}$, and L is the phase inductance. In this work, we assume that the phase inductances are equal to each other.

If $Q_1 - Q_3$ are ON, the circuit is the same as Figure 5.2a with the difference that the conducting switches are in the upper half, and non-conducting switches are in the lower half of the circuit. Therefore, dynamics of the system will be the same as (5.1).

b) Q_1 and Q_2 are OFF, Q_3 is ON: Figure 5.2b demonstrates the circuit configuration in this mode of operation. Using the Kirchhoff's circuit laws, dynamics of the circuit in this mode are expressed as

$$\begin{cases} \frac{di_a}{dt} = \frac{1}{3L}(2v_a - v_b - v_c) + \frac{1}{3}V_B \\ \frac{di_b}{dt} = \frac{1}{3L}(-v_a + 2v_b - v_c) + \frac{1}{3}V_B \\ \frac{di_c}{dt} = \frac{1}{3L}(-v_a - v_b + 2v_c) - \frac{2}{3}V_B \end{cases} \tag{5.2}$$

where V_B indicates the battery voltage. The diodes forward voltage has been neglected for brevity. Similar to (5.2), one can easily derive the model of the circuit when either Q_1 or Q_2 are ON and the other switches are OFF.

c) Q_1 is OFF, Q_2 and Q_3 are ON: The last modes of operation will be the ones with two switches in ON mode and one switch in OFF mode. Let us assume that Q_1 is OFF, while Q_2 and Q_3 are ON, as show in Figure 5.2c. Dynamics of the circuit in this mode can

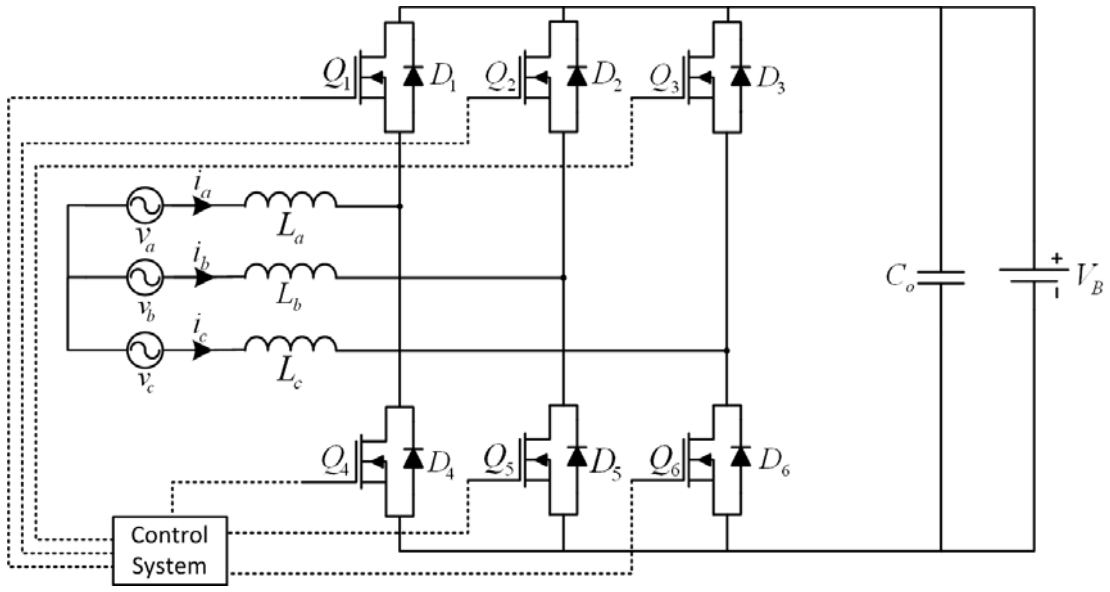

Figure 5.1: Three-phase bridgeless boost converter (dashed lines demonstrate control signals).

be obtained as

$$\begin{cases} \frac{di_a}{dt} = \frac{1}{3L}(2v_a - v_b - v_c) + \frac{2}{3}V_B \\ \frac{di_b}{dt} = \frac{1}{3L}(-v_a + 2v_b - v_c) - \frac{1}{3}V_B \\ \frac{di_c}{dt} = \frac{1}{3L}(-v_a - v_b + 2v_c) - \frac{1}{3}V_B \end{cases} \tag{5.3}$$

By integrating dynamics of the circuit obtained in (5.1), (5.2), and (5.3), individually, one can derive the overall dynamics of the three-phase boost converter as follows

$$\begin{cases} \frac{di_a}{dt} = \frac{1}{3L}(2v_a - v_b - v_c) - \frac{V_B}{6L}(2u_a - u_b - u_c) \\ \frac{di_b}{dt} = \frac{1}{3L}(-v_a + 2v_b - v_c) - \frac{V_B}{6L}(-u_a + 2u_b - u_c) \\ \frac{di_c}{dt} = \frac{1}{3L}(-v_a - v_b + 2v_c) - \frac{V_B}{6L}(-u_a - u_b + 2u_c) \end{cases} \tag{5.4}$$

where u_a, u_b, and u_c can take values from the set $\{-1, 1\}$ (-1 demonstrates the OFF state, while 1 demonstrates the ON state).

By defining $i = [i_a, i_b, i_c]^T$, $v = [v_a, v_b, v_c]^T$, $u = [u_a, u_b, u_c]^T$, and

$$B = \begin{bmatrix} 2 & -1 & -1 \\ -1 & 2 & -1 \\ -1 & -1 & 2 \end{bmatrix} \tag{5.5}$$

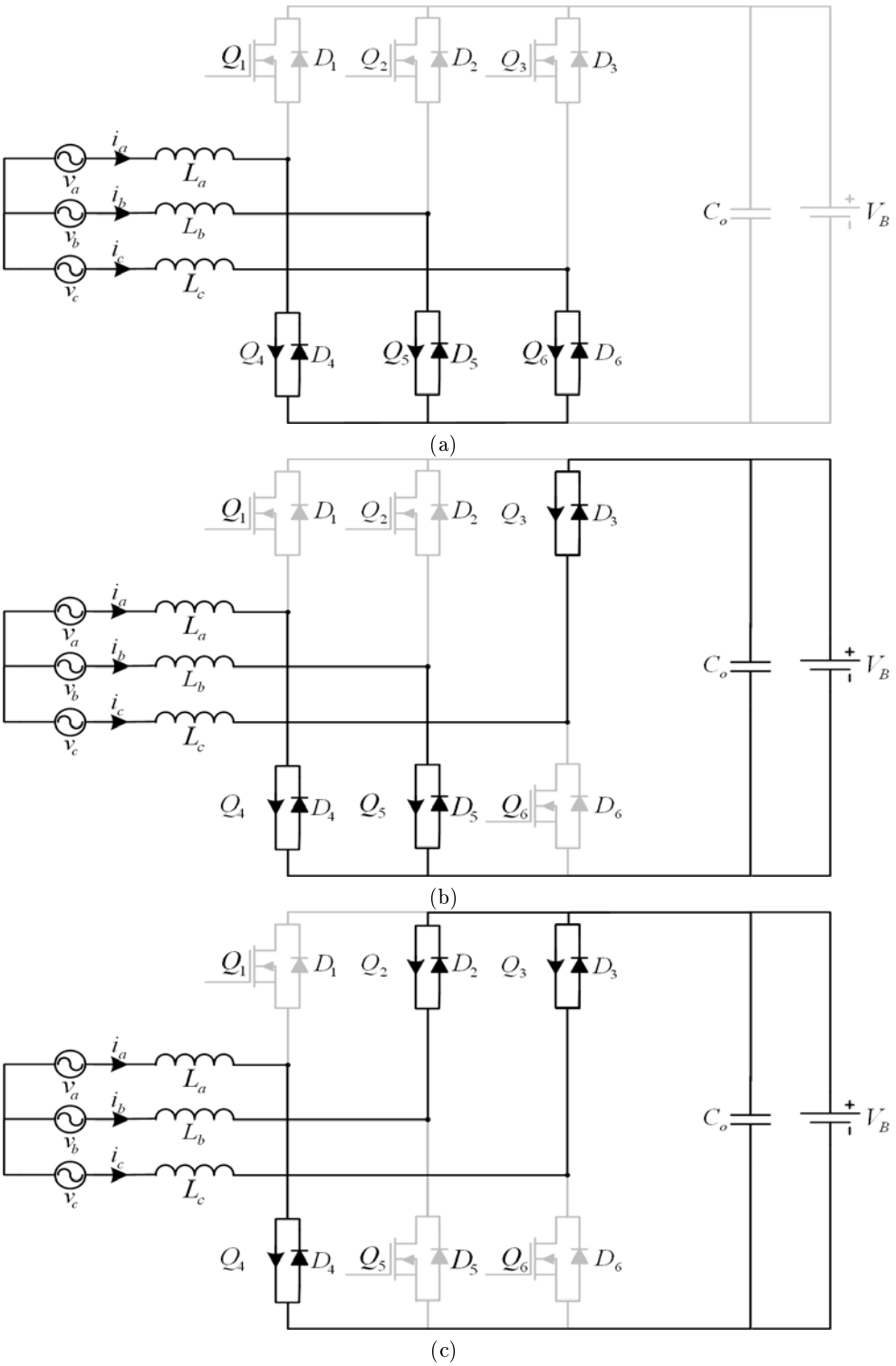

Figure 5.2: Operation modes of the three-phase boost converter when (a) all switches are OFF, (b) two switches are OFF and one switch is ON, (c) one switch is OFF and two switches are ON.

and substituting in (5.4) the following vector model of the circuit can be obtained [119]

$$\frac{di}{dt} = \frac{1}{3L}Bv - \frac{V_B}{6L}Bu. \tag{5.6}$$

Note that, in the overall system the voltage vector v in (5.6) can be replaced by its value from analyzing the input voltage waveform, based on the relative position or angle of the electric machine. This relationship will be further utilized to derive the control strategy for controlling the phase currents of the boost power stage.

5.2 Dynamic Model of a Suspension System Connected to a Linear Permanent Magnet Machine

A single degree-of-freedom suspension system is shown in Figure 5.3. Motion equations of this system are obtained by Newton's second law as follows

$$m\ddot{x}_1 = k(x_2 - x_1) + c(\dot{x}_2 - \dot{x}_1) \tag{5.7}$$

where k, c, and m are the spring coefficient, damping coefficient, and mass, respectively. The base is assumed to be directly connected to tire and road. Hence, x_2 is vibrating based on the road profile changes.

To implement the skyhook semi-active suspension system, the damper in Figure 5.3 is replaced with a three-phase linear permanent magnet synchronous machine, so the damping coefficient can be controlled in real time. This machine enables the energy transfer from mechanical linear vibrations into the energy stored in the battery, which results in damped vibrations. The machine consists of two parts, including a slider with a permanent magnet, and a stator with three-phase windings. The relative motion of these two parts results in generation of voltage across stator windings. In the following, a model of the aforementioned machine is presented to describe the relationship between the relative motion of the slider and the output voltages.

Based on [120] and by calculating the magnetic flux density in the machine, the voltage induced in each phase by the linear motion of slider is described as follows

$$\begin{aligned} v_a &= k_e \cos\left(\frac{\pi}{\tau}(x_1 - x_2)\right)(\dot{x}_1 - \dot{x}_2) \\ v_b &= k_e \cos\left(\frac{\pi}{\tau}(x_1 - x_2) - \frac{2\pi}{3}\right)(\dot{x}_1 - \dot{x}_2) \\ v_c &= k_e \cos\left(\frac{\pi}{\tau}(x_1 - x_2) + \frac{2\pi}{3}\right)(\dot{x}_1 - \dot{x}_2) \end{aligned} \tag{5.8}$$

where k_e and τ are the machine constant and pole pitch, respectively [120]. In (5.8), the induced voltages can be rewritten as multiplication of the magnetic field related coefficient and relative speed of base and mass vibrations as

$$v_p = k_p \dot{x}_\Delta \tag{5.9}$$

where $p \in \{a, b, c\}$, and $k_p = k_e \cos\left(\frac{\pi}{\tau} x_\Delta + \phi_p\right)$. In the latter relationship, ϕ_p denotes the phase shift in each phase, which is equal to 0, $-\frac{2\pi}{3}$, and $\frac{2\pi}{3}$, for phases a, b, and c, respectively. Also, x_Δ denotes the relative displacement of the mass and body, i.e., $x_1 - x_2$.

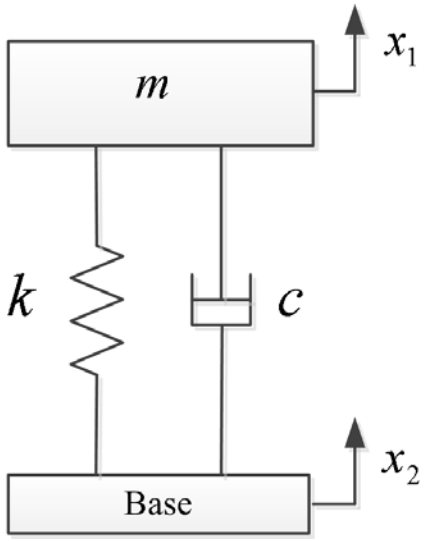

Figure 5.3: A single degree-of-freedom suspension system.

The total thrust force of the machine is proportional to the magnetic field and the phase currents [71] and can be described as the sum of forces produced by each phase as

$$f_{thrust} = \sum_{p \in \{a,b,c\}} k_p i_p. \tag{5.10}$$

The relationship between the thrust force and the phase currents can be further utilized to design a control strategy to provide the damping force needed for semi-active suspension.

To design the suspension system using the skyhook approach, the damper coefficient should be defined as [121]

$$c_{sky} = \begin{cases} c_s \frac{v_1}{v_{12}} & v_1 v_{12} > 0 \\ 0 & v_1 v_{12} < 0 \end{cases} \tag{5.11}$$

where c_s is the constant value of damper, v_1 is the speed, and v_{12} is the relative speed of the mass and base. Utilizing the damper coefficient, the damping force in the suspension system is described as $f_{damping} = c_{sky} v_{12}$, which can be enforced by controlling f_{thrust} from (5.10). Therefore, by controlling the phase currents of the machine, one is able to control the generated force, which results in controlling the damping force of the suspension system. The issue of controlling the phase currents of the linear machine is addressed in the next section.

5.3 Controller Design Strategy for Linear Electric Machine

The control purpose in this work is to provide a controllable resistive behavior across the input terminals of the converter. It can be done by controlling the switching pattern of the switches so the overall circuit acts like the circuit shown in Figure 5.4. By providing a controllable resistive behavior using the boost converter, the output current of the linear permanent magnet machine will be controlled; hence, the damping force will be controlled based on (5.10). Solving the circuit in Fig. 5.4 in general results in (5.12). Therefore, the control goal can be redefined as regulating the input currents of the converter (phase currents) to follow desired currents, as follows

$$\begin{bmatrix} i_a \\ i_b \\ i_c \end{bmatrix} = \frac{1}{R} \begin{bmatrix} v_a \\ v_b \\ v_c \end{bmatrix} \tag{5.12}$$

where

$$R = \frac{1}{R_1R_2 + R_2R_3 + R_3R_1} \begin{bmatrix} 2(R_2+R_3) & R_2 & R3 \\ R_1 & 2(R_1+R_3) & R3 \\ -(R_1+2R_2+2R_3) & -(2R_1+R_2+2R_3) & -2R_3 \end{bmatrix}. \tag{5.13}$$

Considering the application of this controller in an active suspension system, the value of resistances $R_i, i = 1, 2, 3$ are assumed to be equal to R. Based on this assumption and as the input voltage sources have 120 degrees phase difference, the final currents can be simply calculated based on $i_p = \frac{1}{R} v_p$, $p \in \{a, b, c\}$.

To design the controller, an issue of uncontrollability for a set of control signals u_ps exists. Singularity of the gain matrix B yields in loss of controllability of the system in cases where

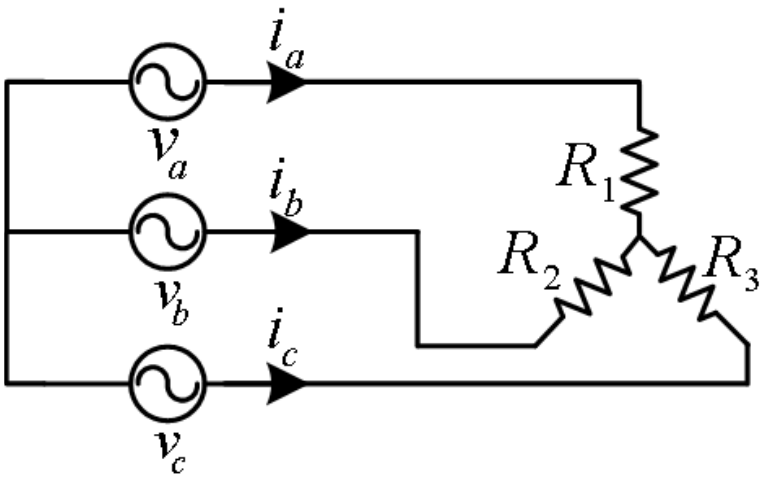

Figure 5.4: Three phase resistive circuit.

$u = [1, 1, 1]^T$ and $u = [-1, -1, -1]^T$. As these conditions will happen for finite times in real time control, the controller design is based on the assumption of avoiding these events to happen [119].

The sliding surface for the controller is defined based on the tracking error as follows

$$\sigma_p = i_p - i_{des_p} \tag{5.14}$$

where $p \in \{a, b, c\}$ and i_{des} denotes the desired current profile. Based on the definition in (5.14), enforcing the system to reach $\sigma_i = 0$ is equivalent to the convergence of the errors to zero.

To demonstrate the stability of the controller in sliding mode, Lyapunov analysis can be used. Let us assume the Lyapunov function $V = \frac{1}{2}\sigma^T\sigma$. Therefore, its derivative is written as

$$\dot{V} = \sigma^T\dot{\sigma} = \sigma^T\left(\frac{1}{3L}Bv - \frac{V_B}{6L}Bu - \frac{1}{R}\dot{v}\right). \tag{5.15}$$

The goal of the Lyapunov analysis is choosing control signal u such that $\dot{V} < 0$. In order

to do so, let us define

$$\begin{aligned}\psi_p &= \left(\frac{k_e\dot{x}_\Delta}{L} - \frac{k_e\ddot{x}_\Delta}{R}\right)\cos\left(\frac{\pi}{\tau}x_\Delta + \phi_p\right) + \frac{V_B}{6L}\sum_k u_k \\ &+ \left(\frac{k_e\pi}{R\tau}\dot{x}_\Delta^2\right)\sin\left(\frac{\pi}{\tau}x_\Delta + \phi_p\right) \end{aligned} \tag{5.16}$$

where $p, k \in \{a, b, c\}$, and ϕ_ps are defined as $\phi_a = 0$, $\phi_b = \frac{-2\pi}{3}$, and $\phi_c = \frac{2\pi}{3}$.

Using (5.16) one can re-write (5.15) as

$$\dot{V} = \sum_p \sigma_p\psi_p - \frac{V_B}{2L}\sum_p \sigma_p u_p. \tag{5.17}$$

The later relationship can be utilized to derive the existence condition of the sliding modes [119].

$$\begin{aligned}\dot{V} &\leq \sum_p |\sigma_p|\,|\psi_p| - \frac{V_B}{2L}\sum_p |\sigma_p|\,u_p sign(\sigma_p) \\ &\leq \bar{\psi}\sum_p |\sigma_p| - \frac{V_B}{2L}\sum_p |\sigma_p| \\ &\leq -\left(\frac{V_B}{2L} - \bar{\psi}\right)\sqrt{\sum_p \sigma_p^2} = -\left(\frac{V_B}{2L} - \bar{\psi}\right)\sqrt{\sigma^T\sigma} \\ &= -\left(\frac{V_B}{2L} - \bar{\psi}\right)\sqrt{2V} \end{aligned} \tag{5.18}$$

where the control signal u_p is defined as $sign(\sigma_p)$ and $\bar{\psi}$ is defined as $max(\bar{\psi_p})$. Also, $\bar{\psi_p}$ is the maximum value of ψ_p. Based on

$$a\cos x + b\sin x = \sqrt{a^2 + b^2}\cos\left(x - \tan^{-1}\frac{b}{a}\right), \tag{5.19}$$

the value of $\bar{\psi}$ can be obtained as

$$\bar{\psi} = \frac{V_B}{6L} + \sqrt{\left(\frac{k_e\pi}{R\tau}\dot{x}_\Delta^2\right)^2 + \left(\frac{k_e\dot{x}_\Delta}{L} - \frac{k_e\ddot{x}_\Delta}{R}\right)^2}. \tag{5.20}$$

Based on the Lyapunov theorem, the existence condition of the sliding mode is given as

$$\frac{V_B}{2L} - \bar{\psi} > 0. \tag{5.21}$$

Utilizing (5.20) in (5.21), the following inequality should exists between the input voltage amplitudes, the desired resistances, and the circuit parameters, so the sliding mode controller

can provide finite time convergence of σ to zero [119].

$$\sqrt{\left(\frac{k_e\pi}{R\tau}\dot{x}_\Delta^2\right)^2 + \left(\frac{k_e\dot{x}_\Delta}{L} - \frac{k_e\ddot{x}_\Delta}{R}\right)^2} < \frac{V_B}{3L}. \tag{5.22}$$

The value of L is relatively small, and if $\dot{x}_\Delta$ is small enough, (5.22) can be simplified to $3k_e\dot{x}_\Delta < V_B$. Thus, based on the knowledge about the nature of the input, selecting a proper battery size is plausible, to ensure the existence condition of the sliding mode.

5.4 Simulation Results for a Linear Electric Machine

To verify the performance of the controller in section 5.3, and the damping system based on skyhook method, a Simulink model of the converter along with the proposed sliding mode controller was developed using the SimPowerSystems toolbox in Matlab/Simulink environment. Figure 5.5 demonstrate the schematics of the feedback control system. After that, the suspension system was simulated along with the linear permanent magnet machine and the power electronics circuit. The results of these two simulations is analyzed in this section.

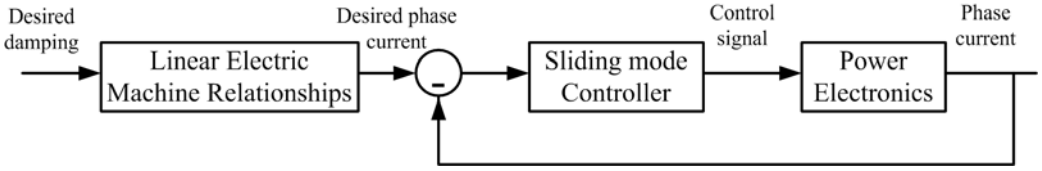

Figure 5.5: Feedback control system schematics.

5.4.1 Controller performance

The parameters of the circuit and controller simulation are shown in Table 5.1. The system was simulated using sinusoidal input voltage sources for different conditions.

In the first test, the source inputs were chosen as $v_a = 12.5\sin(40\pi t)$, $v_b = 12.5sin(40\pi t - \frac{2\pi}{3})$, and $v_c = 12.5\sin(40\pi t + \frac{2\pi}{3})$, while the desired resistances were chosen to be equal to each other and equal to 2Ω. In the second test, the desired resistances were chosen as $R_1 = 2\Omega$, $R_2 = 1\Omega$, and $R_3 = 0.5\Omega$ to demonstrate the effectiveness of the controller when the desired resistances are not equal to each other. Figure 5.6 demonstrates the performance

of the controller in these tests. This figure verifies the perfect performance of the controller to regulate the input currents of the converter.

Table 5.1: Simulation circuit parameters

Item	**Value**
Boost inductor, $L(mH)$	0.1
Inductors resistance (Ω)	0.01
Boost output capacitor, $C(mF)$	0.2
Battery voltage, $V_B(V)$	36
Switching frequency, $f_s(kHz)$	10

5.4.2 Lyapunov existence condition

Equations (5.9) and (5.22) show that increasing the input voltage of the converter more than a certain boundary value, results in the violation of the existence condition. To demonstrate the effect of the Lyapunov existence condition, the control system was re-simulated for larger input voltages. The amplitude of phase voltages were decreasing over time, but they are violating (5.22) in the first period (before $t = 0.02$). Figure 5.7 illustrates the phase currents in this situation, which indicates that the controller is unable to converge to the sliding surface, in the periods that the Lyapunov existence condition has not been satisfied.

5.4.3 Robustness analysis through simulation

In the next step, the robustness of the controller was investigated by changing the desired input resistances, and the input voltage sources. The simulation started with the first set of parameters from Table 5.2. After $t = 0.1$, it is switched to the second set from the table, and again at time $t = 0.2$, the third set is selected. Figure 5.8 illustrates the results of these tests, which show almost no performance deterioration of the controller in terms of keeping the resistive behavior. Also, the changes in the amplitude and frequency of the input voltages and the effect of varying the desired resistances can be verified in this figure.

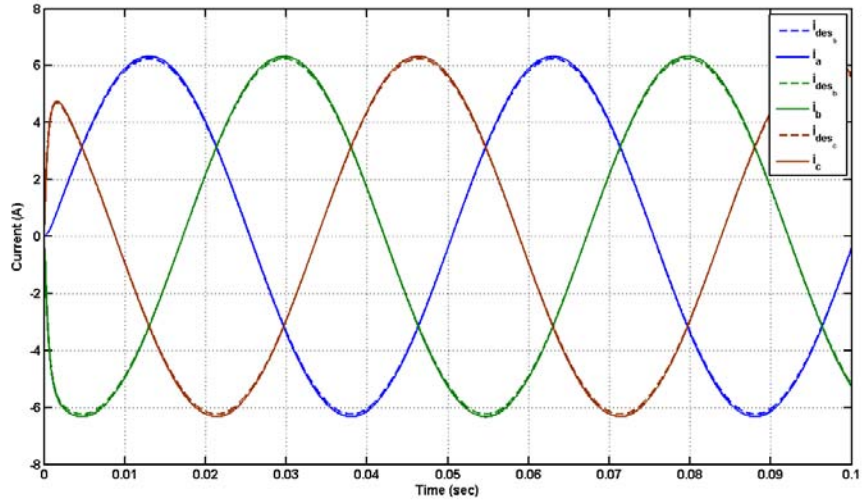

(a)

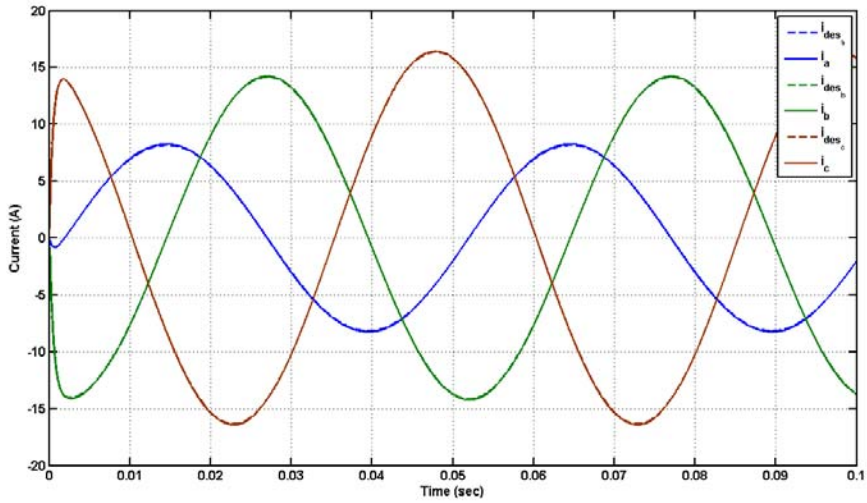

(b)

Figure 5.6: Simulation results for the closed-loop controller in different situations: (a) Sinusoidal inputs and equal desired resistances, (b) Sinusoidal inputs and different desired resistances.

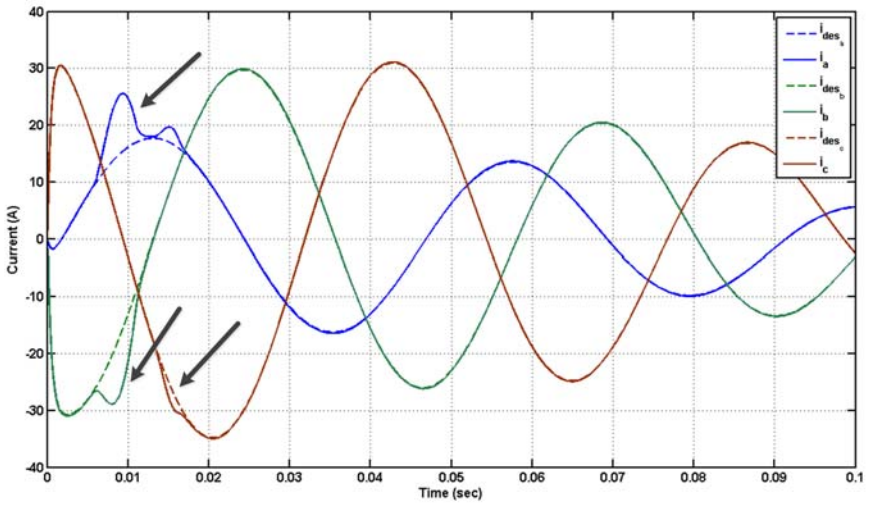

Figure 5.7: Simulation results for the closed-loop controller in the case that Lyapunov existence condition has not been satisfied. Arrows show the inability of the controller to converge to the sliding surface, in this case.

Table 5.2: Robustness analysis parameters

Set	v_a	$[R_1, R_2, R_3]$
1	$6.25sin(40\pi)$	[2,1,0.5]
2	$12.5sin(24\pi)$	[2,1,0.5]
3	$12.5sin(24\pi)$	[1,2,1]

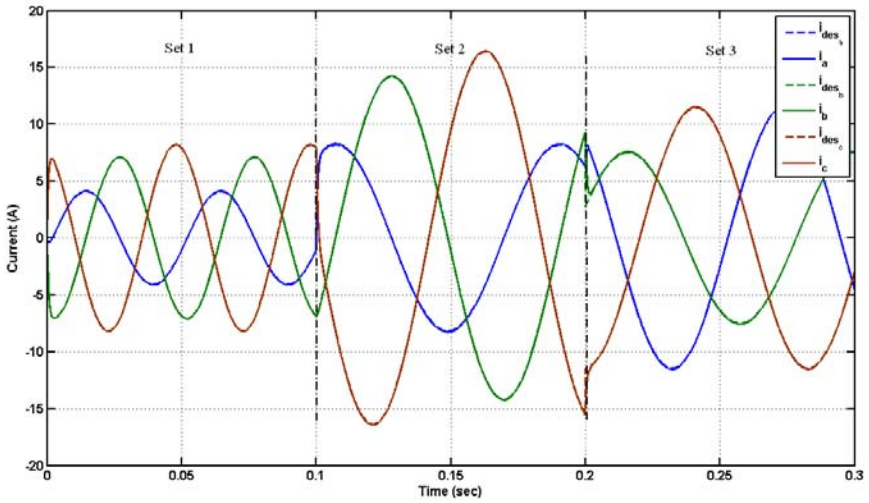

Figure 5.8: Robustness of the controller regarding to instantaneous changes in input voltages, and desired resistances.

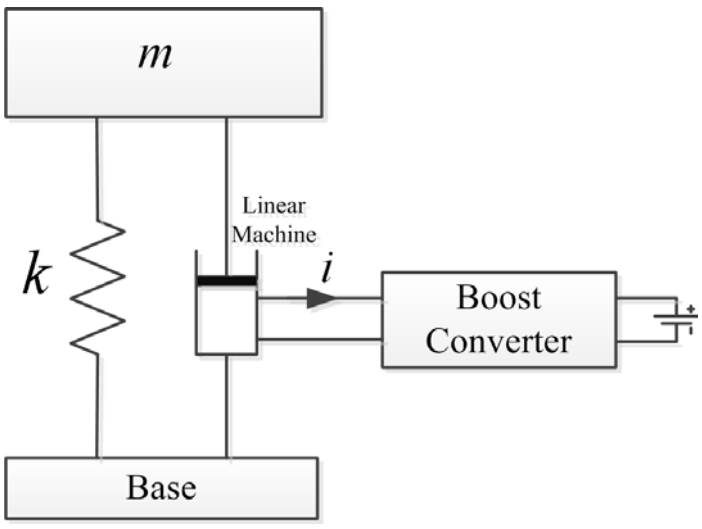

Figure 5.9: Suspension system schematic.

5.4.4 Simulation of the semi-active suspension system

In the last simulation, the performance of the power electronic control system was evaluated on a single degree of freedom suspension system including a skyhook damper. The schematic diagram of the system is shown in Figure 5.9. In this figure, the damping force exerted by the linear machine can be set and controlled through the boost converter input current. The parameters of the suspension system were chosen as $m = 86.4kg$ and $k = 7000N/m$. The results of the suspension system were compared with a simple spring and damper suspension system with a passive damper.

Figure 5.10 demonstrates the displacement transmission ratio between the base and the mass for the two cases as a function of $\frac{\omega}{\omega_n}$, where ω is the excitation frequency and ω_n is the natural frequency of the suspension system. As it is illustrated in this figure, the proposed semi-active suspension system acts better for low and high frequency vibrations. For low frequency vibrations, the transmissibility is lower than the passive system. Regardless of the value of ζ in the high frequency range, the transmissibility would always converge to zero. Also, in the proposed semi-active suspension system, the generated energy from damping, is stored in the battery, rather than wasted as heat in the damping system.

5.5 Dynamic Model of a Regenerative Suspension System Connected to a Rotary Permanent Magnet Machine

The amount of energy dissipated in a conventional suspension system can be stored by utilizing an electric system as indicated by [122], [123], which demonstrate that the dissipated energy of four dampers in a passenger car on a poor roadway with a speed of 13.4 m/s can reach to approximately 200W. In this section, the proposed control method for 3-phase boost converter circuit is utilized to store this energy into the battery. A mechanism to interface road vibrations and the boost converter circuit is a two-leg mechanism developed in the *Motion and Power Electronics Control Laboratory*. This mechanism converts vibrational linear motion into rotary motion, and a rotary permanent magnet machine is used to convert mechanical energy to electrical energy.

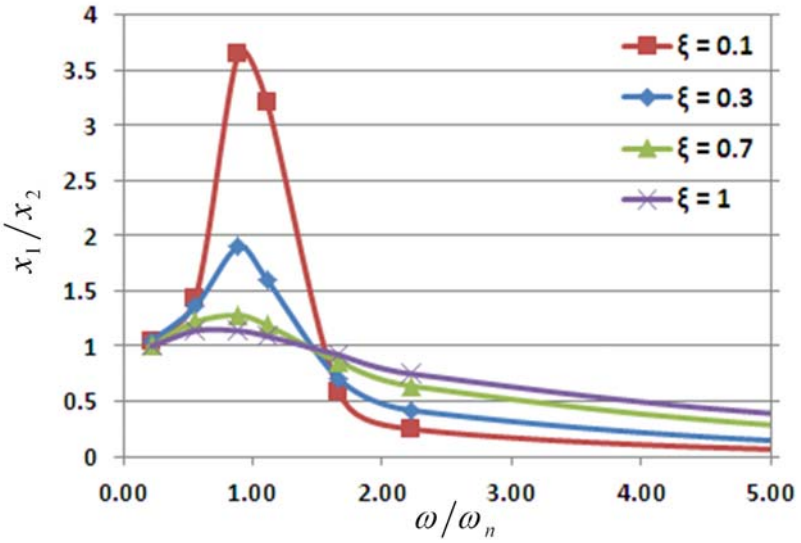

(a)

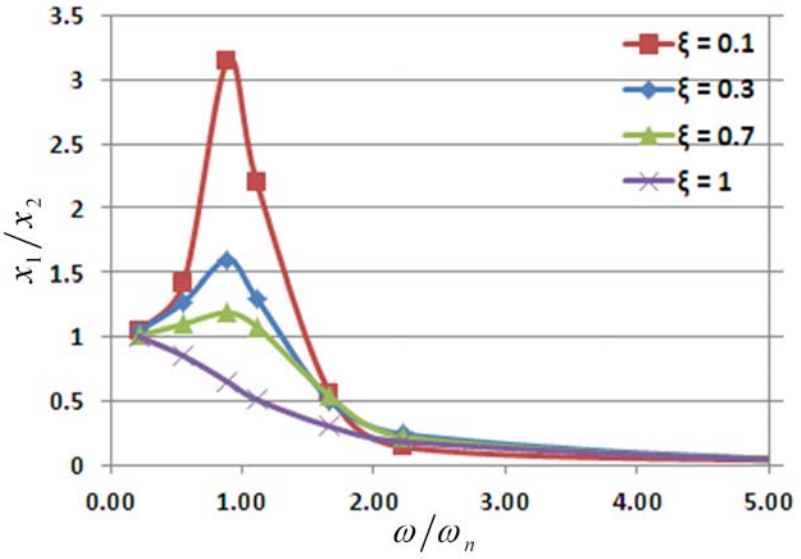

(b)

Figure 5.10: Simulation results for the single degree of freedom suspension system: (a) Passive suspension system, (b) Skyhook semi-active suspension system.

5.5.1 Regenerative Shock Absorber Using a Two-Leg Conversion Mechanism

Mechanical vibrations in a vehicle suspension system produce reciprocating motion. This motion has to be converted into rotary motion to be usable by the rotary machine. Using this system, rather than a linear machine, is more cost-effective and the resulting device would be much smaller in size. The interface between linear vibrations and rotary motion is done using a two-leg conversion mechanism. Figure 5.11 illustrates the designed shock absorber which will damp the vibrations while controlling the damping coefficient. The rotary machine will be introduced in the next section. Figure 5.12 shows the schematic diagram of the two-leg mechanism designed and developed in *Motion and Power Electronics Control Laboratory, Simon Fraser University*, by Mr. Amir Maravandi . This mechanism acts as a converter of the linear vibrational motion to rotary motion. The rotary motion is then translated to the rotary machine utilizing a gear-head system. The relations of the linear motion, rotary motion, and the total damping of the system are described in [124]. In [124] the effect of connecting resistors at the output terminals of the rotary machine is described. Based on the analysis, the relation between the linear damping coefficient of the system, and the resistance values is as follows

$$B_L = \frac{1.5 \times n^2 {k_t}^2}{\eta_{tl}\eta_{gh}\eta_g c^2 (R + r)} \tag{5.23}$$

where B_L is the linear damping coefficient, n is the gear-head ratio, k_t is the torque constant of the rotary machine, c is the linear to rotary motion conversion ratio, R and r are the external and internal resistances of the rotary machine, respectively, and η_{tl}, η_{gh}, and η_g are two-leg mechanism, gear-head and generator efficiencies, respectively.

Utilizing (5.23) and the proposed control strategy in this chapter, the linear damping of the system can be controlled, based on desired needs of the system. To perform the experiments, the whole system has been tested with an actual resistor, and also with the developed power electronic circuit. The results were compared to each other for different amplitudes and frequencies of vibration.

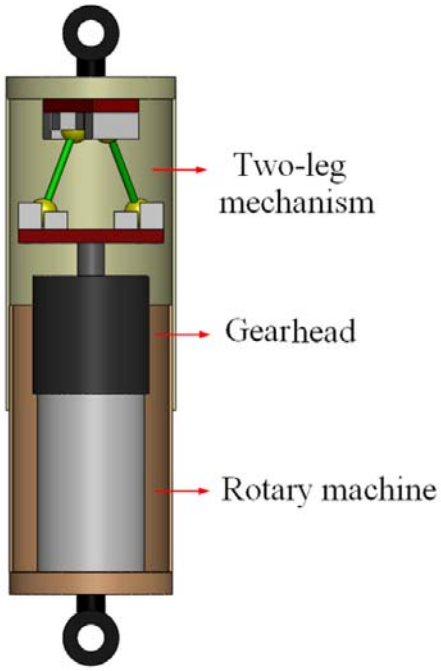

Figure 5.11: Regenerative shock absorber [124].

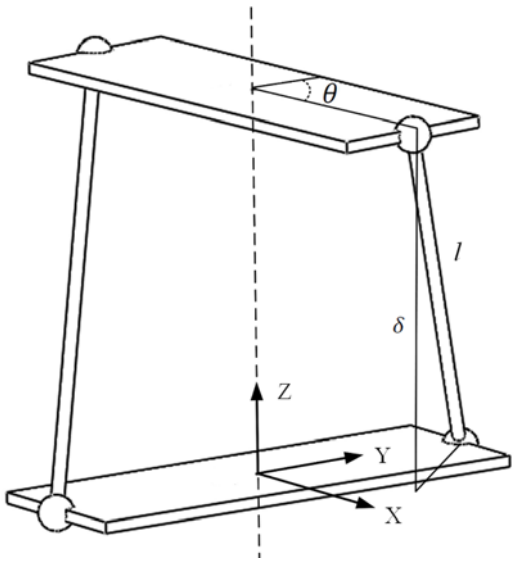

Figure 5.12: Two-leg mechanism schematic diagram [124].

5.5.2 Rotary Permanent Magnet Machine and Controller Design and Considerations

The rotary machine in this work is a brushless permanent magnet synchronous generator. In this machine, the rotor is a permanent magnet, while the stator includes 3-phase windings, spatially apart by 120 degrees. Based on the rotational movement of the motor, a 3-phase voltage waveform will be induced in the stator coils [125]. These voltages are given by

$$\begin{aligned} v_a &= N\Phi\omega(t)\cos\left(\theta(t)\right) \\ v_b &= N\Phi\omega(t)\cos\left(\theta(t)-\frac{2\pi}{3}\right) \\ v_c &= N\Phi\omega(t)\cos\left(\theta(t)+\frac{2\pi}{3}\right). \end{aligned} \tag{5.24}$$

where N is the number of turns in each stator coils, $\theta(t)$ is the rotor angular position, which is time-dependent, and Φ represents the flux passing through each coil given by

$$\Phi = 2rl_C B_M \tag{5.25}$$

in which l_C represents the length of the conductor in the magnetic field, B_M is the maximum magnetic flux density, and r is the radius of the conductor. Rotor angular speed, i.e., $\omega(t)$, can also be defined as

$$\theta(t) = \int_0^t \omega dt + \theta(0) \rightarrow \omega(t) = \frac{d\theta(t)}{dt} \tag{5.26}$$

where $\theta(t)$ is the angular position of rotor, which will be changing based on the road condition.

Using the relations of the 3-phase boost converter and applying similar control strategy, one can design a proper sliding mode control and find the existence conditions of the sliding modes for the case of connecting the 3-phase rotary machine to the circuit.

Based on (5.24), and by defining $\nu(t) = N\phi\omega(t)$ and $Cos_\theta = [\cos\left(\theta(t)\right), \cos\left(\theta(t)-\frac{2\pi}{3}\right)$, $\cos\left(\theta(t)+\frac{2\pi}{3}\right)]^T$, one can re-write (5.6) as

$$\frac{di}{dt} = \frac{1}{3L}B\nu(t)Cos_\theta - \frac{V_B}{6L}Bu. \tag{5.27}$$

By defining similar sliding surface, control signal, and Lyapunov function as before, the control goal is showing that the control signal is chosen such that $\dot{V} < 0$. To do so, let us

define

$$\begin{aligned}\psi_p &= \left(\frac{\nu(t)}{L}+\frac{\nu(t)\dot{\omega}(t)}{R}\right)\sin\left(\theta(t)+\phi_p\right)+\frac{V_B}{6L}\sum_k u_k \\ &- \frac{\dot{\nu}(t)}{R}\cos\left(\theta(t)+\phi_p\right)\end{aligned} \tag{5.28}$$

where $p,k\in\{a,b,c\}$, and ϕ_ps are defined as $\phi_a=0$, $\phi_b=\frac{-2\pi}{3}$, and $\phi_c=\frac{2\pi}{3}$.

Using (5.28) one can re-write (5.15) as

$$\dot{V}=\sum_p \sigma_p\psi_p-\frac{V_B}{2L}\sum_p \sigma_p u_p \tag{5.29}$$

which is similar to (5.17). The rest of the formulations are the same as in section 5.3. The only difference is the value of $\bar{\psi}$, which in this case can be obtained as

$$\bar{\psi}=\frac{V_B}{6L}+\sqrt{\left(\frac{\nu(t)}{L}+\frac{\nu(t)\dot{\omega}(t)}{R}\right)^2+\left(\frac{\dot{\nu}(t)}{R}\right)^2} \tag{5.30}$$

Based on the Lyapunov theorem, the following inequality should exists between the input voltage amplitudes, the desired resistances, and the circuit parameters, so the sliding mode controller can provide finite time convergence of σ to zero [119].

$$\sqrt{\left(\frac{\nu(t)}{L}+\frac{\nu(t)\dot{\omega}(t)}{R}\right)^2+\left(\frac{\dot{\nu}(t)}{R}\right)^2}<\frac{V_B}{3L}. \tag{5.31}$$

Since the value of L is usually small, and if $\dot{\omega}(t)$ is small enough, (5.31) can be simplified to $3\nu(t)<V_B$. Thus, based on the knowledge about the nature of the input sources, selecting a proper battery size is plausible, to ensure the existence condition of the sliding mode.

5.6 Simulation Results for the Rotary Machine Output Control

To verify the performance of the controller, a Simulink model of the converter along with the proposed sliding mode controller is developed using the SimPowerSystems toolbox in the Matlab/Simulink environment. The parameters of the simulation are shown in Table 5.1. The schematics of the control system would be the same as for the linear electric machine, i.e., Figure 5.5, with the difference of having rotary electric machine in the schematics.

Simulation results were obtained for road profiles using Gaussian functions. In these simulations the transfer characteristics between the linear damper movement, and rotary movement of the rotor were assumed to be linear. Also, extra simulations were performed to illustrate the effect of inequality (5.31) in the existence of the solution and to demonstrate the robustness of the controller in response to instantaneous changes in the desired damping.

A combination of four Gaussian functions were chosen to simulate the actual bumps and holes of a sample road profile. Therefore, the rotary angle for each section is defined as follows

$$\theta(t) = ae^{-\frac{(t-b)^2}{2c^2}} \tag{5.32}$$

where a, b, and c are the height, peak position, and the standard deviation of the function, respectively. By changing these constants, different scenarios can be simulated. For the purpose of this simulation, the parameters for four different functions are set as shown in Table 5.3.

Table 5.3: Gaussian functions parameters

Set	a	b	c
1	2.5	0.05	0.01
2	0.6	0.1	0.003
3	2	0.17	0.02
4	-1	0.25	0.005

Using (5.32), the angular speed is given by

$$\omega(t) = \frac{d\theta(t)}{dt} = -a\frac{t-b}{c^2}e^{-\frac{(t-b)^2}{2c^2}}. \tag{5.33}$$

By utilizing (5.33) in (5.24), the input voltage sources are derived as follows

$$\begin{aligned} v_a &= N\Phi(-a\frac{t-b}{c^2}e^{-\frac{(t-b)^2}{2c^2}})\cos\left(ae^{-\frac{(t-b)^2}{2c^2}}\right), \\ v_b &= N\Phi(-a\frac{t-b}{c^2}e^{-\frac{(t-b)^2}{2c^2}})\cos\left(ae^{-\frac{(t-b)^2}{2c^2}} - \frac{2\pi}{3}\right), \\ v_c &= N\Phi(-a\frac{t-b}{c^2}e^{-\frac{(t-b)^2}{2c^2}})\cos\left(ae^{-\frac{(t-b)^2}{2c^2}} + \frac{2\pi}{3}\right) \end{aligned} \tag{5.34}$$

The voltage signal in (5.34) is used with the control algorithm simulated such that the currents of the rotary machine are regulated based on the desired resistance. Figure 5.13a

demonstrates the road profile. Also, Figure 5.13b demonstrates the desired and actual currents of each phase, corresponding to desired values of damping. In this simulation, the value of desired resistance was set to 2Ω. The simulation results demonstrate perfect tracking of the desired currents in each phase.

5.6.1 Lyapunov existence condition

To demonstrate the effect of (5.31), the simulation has been iterated for a larger input voltage which will cause $\nu(t)$ to be larger than the battery voltage divided by 3, in a small period of time. Figure 5.14 illustrates a phase current waveform in this situation, which indicates that the controller is unable to converge to the sliding surface whenever inequality (5.31) is not satisfied (shown by arrows). In this figure, the results have been illustrated for one phase. Similar characteristics are found for the other 2 phases.

5.6.2 Robustness analysis

In the last step of simulation, the robustness of the controller was investigated by changing the desired input resistances, i.e., desired damping. To perform this investigation, the value of desired input resistance is changed from 2Ω to 0.5Ω instantaneously, at $t = 0.15s$. Figure 5.15 illustrates the results of this test, which evidently shows almost no performance deterioration of the controller in terms of maintaining the resistive behavior. Also, in this figure, just one of the phase currents and its desired values are shown.

5.7 Experimental Results for the Regenerative Suspension System

The 3-phase boost converter is implemented and utilized in a shock absorber system including a two-leg mechanism, a planetary gear-head (Maxon GP52C223087), and a rotary permanent magnet brushless machine (Maxon ECmax40-369146) developed in the laboratory. To excite the shock absorber system, a hexapod (Mikrolar P2000) was used. Force and displacement signals were measured with a load cell (L204-200 from Omega) and a displacement sensor (MLT series 101.6 mm from Honeywell), respectively. Also, a dSPACE 1104 real-time board along with a host computer system running Matlab is used for controller implementation and also data acquisition purposes. Figure 5.16 demonstrates the overall experimental system.

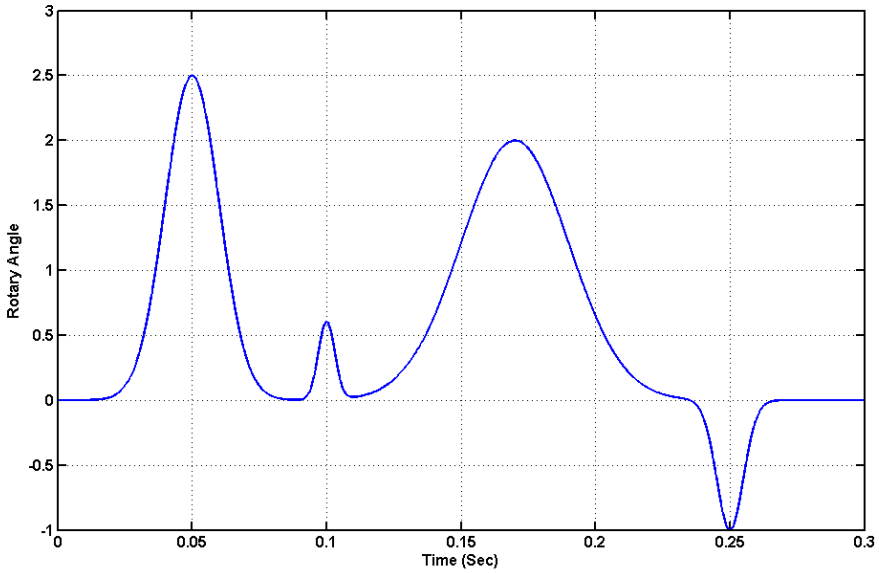

(a)

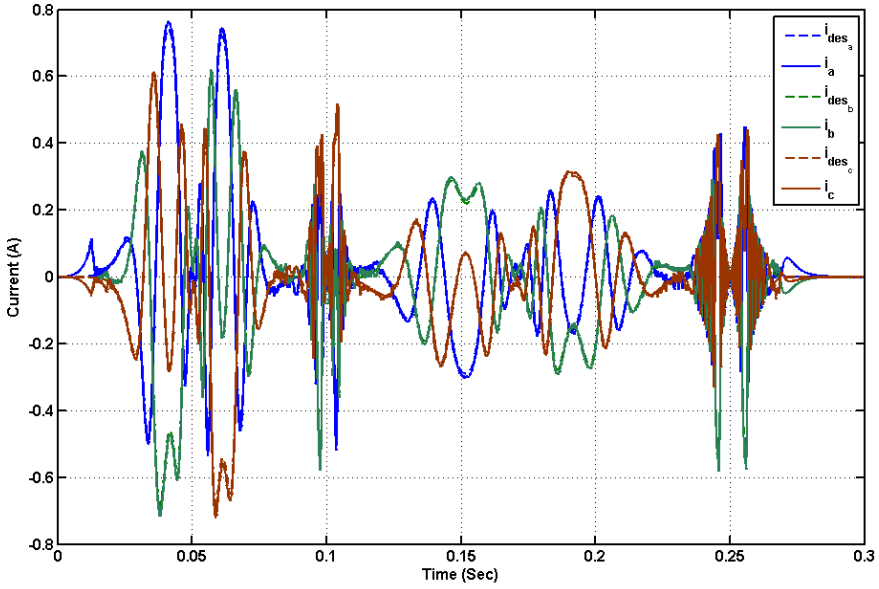

(b)

Figure 5.13: Simulation of a Gausian road profile: (a) Road profile, (b) Phase and desired currents.

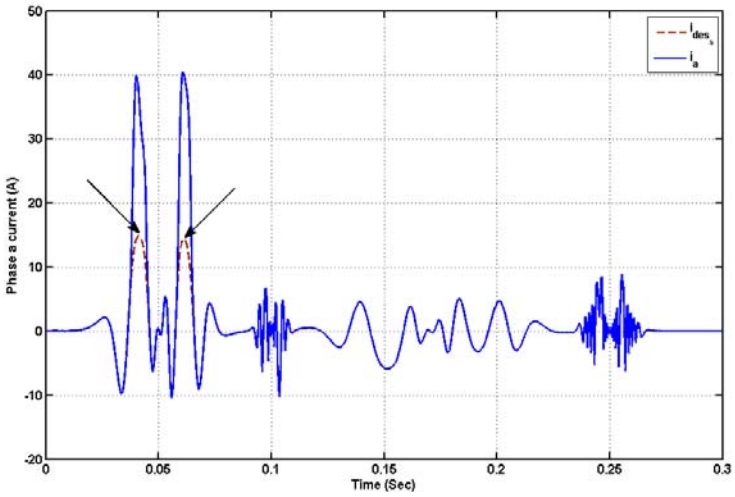

Figure 5.14: Simulation results, when the input voltage sources does not satisfy (5.31). Arrows show the inability of the controller to converge to the sliding surface in this case.

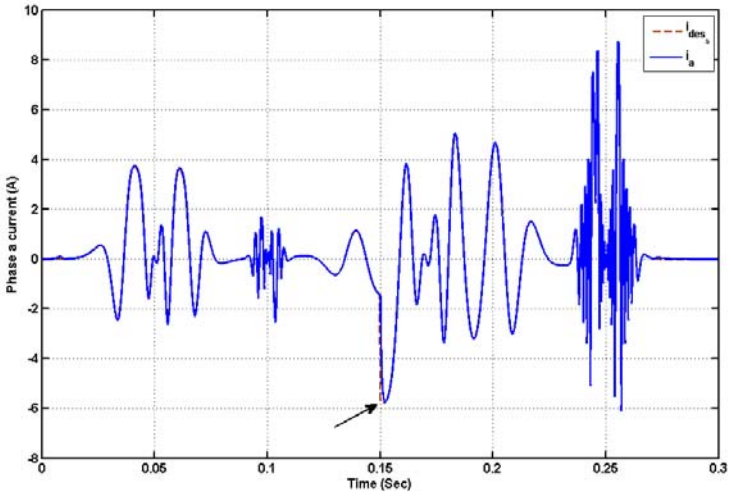

Figure 5.15: Robustness analysis results, for changing the desired input resistance at $t = 0.15s$. Arrow shows the point that the change in the input resistance is applied.

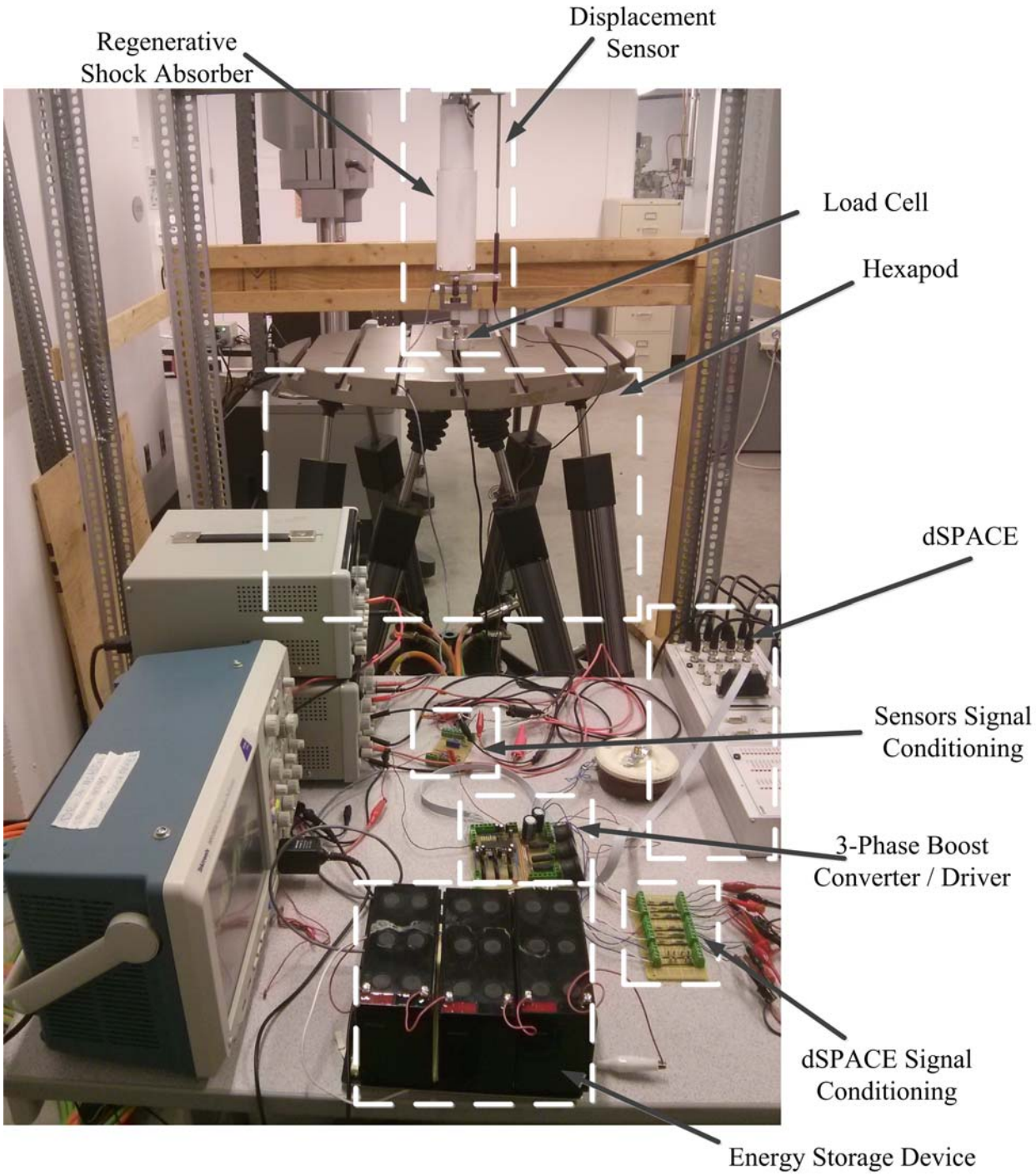

Figure 5.16: Experimental system.

The parameters of this system are introduced in [124]. Also, in [124] the relationship between linear damping coefficient, and the external resistance were verified. The main purpose of this research is to evaluate the performance of the 3-phase boost converter control strategy.

In the first condition, the external resistances were set as 0.5Ω. Then, the system was ran under different emulated vibration profiles, i.e., various amplitudes and frequencies, and force-displacement loops were recorded. In the second experiment, the external terminals of the rotary machine were connected to the 3-phase boost power electronic system, and the desired resistances was set to 0.5Ω. The system was again ran under similar vibrations as before, and the force-displacement loops were recorded. In the second set of experiments, the value of sense resistors, i.e., 0.2Ω, were considered as well.

Figure 5.17 demonstrates the force-displacement curves for different amplitudes and frequencies when a sinusoidal excitation is used. Considering the difference in the values of resistors, the results in Figure 5.17, comply with the results reported in [124] for the value of linear damping coefficient. From this figure, it is also evident that the controller exhibits the system response similar to the case where an external resistor was connected to the circuit. In lower frequencies and/or amplitudes, as the output voltage of the rotary machine is very small, the current is very small, which results in measurement errors. This error can be seen in Figure 5.17 as the difference between controller resistance and constant resistance in lower frequencies and/or amplitudes.

Figure 5.18 demonstrates the force-displacement loops at frequencies of $1Hz$ and $2Hz$, for different amplitudes. Referring to this figure, the amount of damping energy (area inside the graphs) is increasing, based on the increase in linear vibration amplitude, which shows the increasing amount of vibrational energy. In this figure, it is also evident that the system with the controlled power electronic circuit can act similar to the system with constant resistors. Moreover, the fluctuations in the graphs are mainly because of the linear estimation error in the linear-to-rotary conversion relation stated in [124], which can be alleviated by proper control technique to consider the nonlinearities of the system as well.

5.8 Conclusion

In this chapter a sliding mode controller along with a three-phase boost converter were utilized to develop a semi-active regenerative suspension system. Using a proper control

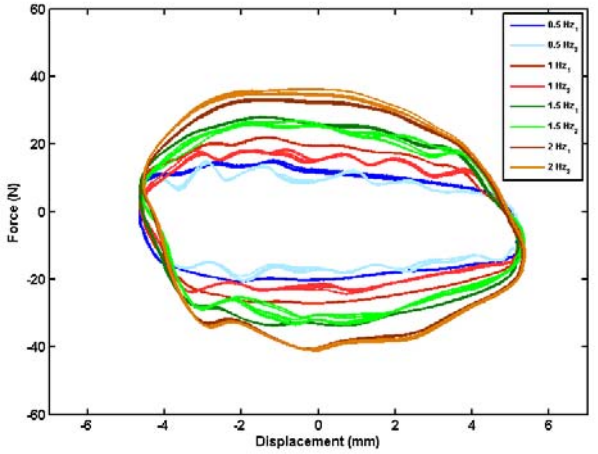

(a)

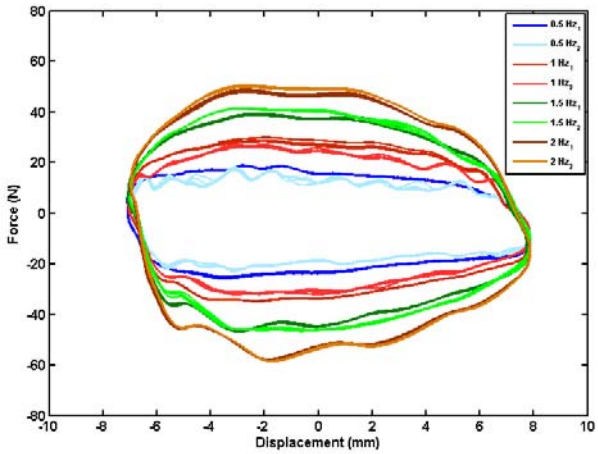

(b)

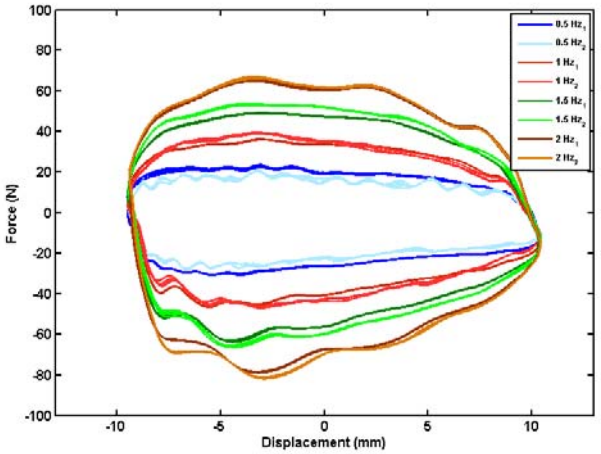

(c)

Figure 5.17: Force-displacement loops for different frequencies and the amplitudes of (a) $5mm$, (b) $7.5mm$, and (c) $10mm$. Subscripts 1 and 2 denote the test with constant resistance and the test with the controlled power electronic circuit, respectively.

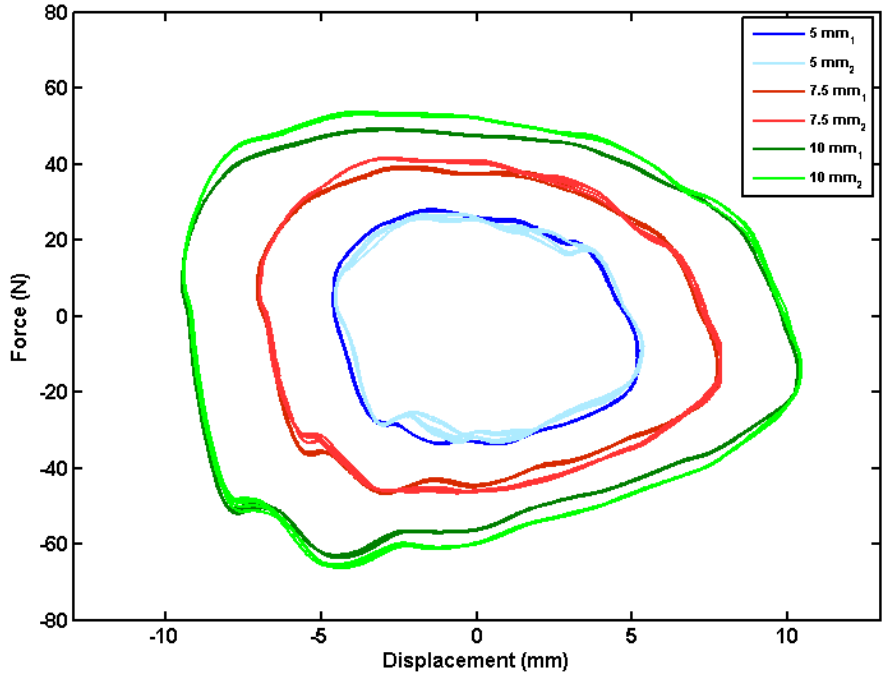

(a)

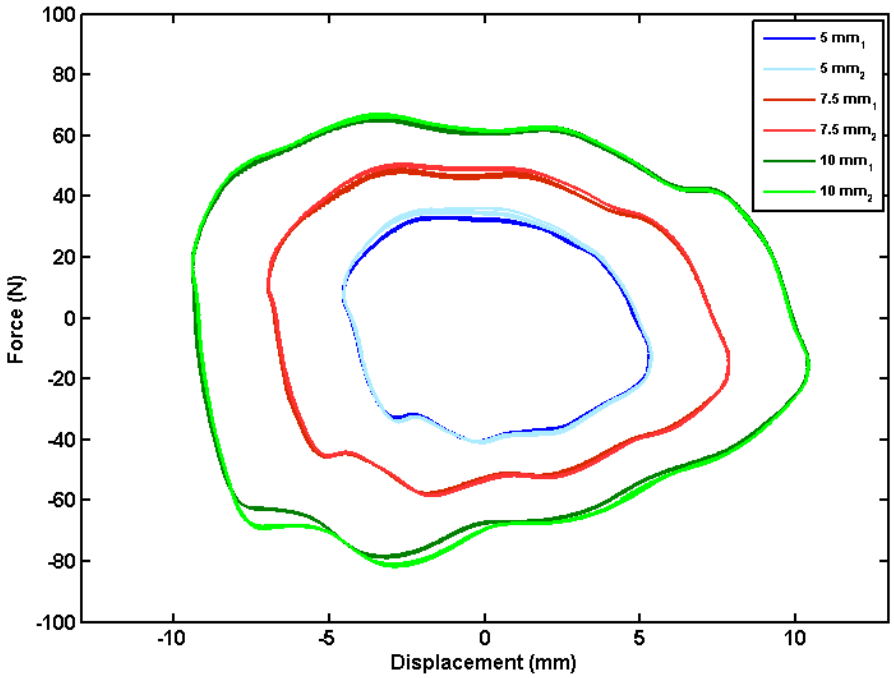

(b)

Figure 5.18: Force-displacement loops for different amplitudes and the frequency of (a) $1.5Hz$ and (b) $5Hz$. Subscripts 1 and 2 denote the test with constant resistance and the test with the controlled power electronic circuit, respectively.

strategy to enforce a resistive behavior across the input terminals of the converter, the required mechanical damping determined by the desired system damping was provided. The performance of the proposed control system and the suspension system were evaluated by simulation in the Matlab environment for a linear permanent magnet machine and by experiment using a two-leg mechanism and a rotary machine. The results demonstrate that not only the proposed nonlinear controller can enforce a resistive behavior and overcome the robustness issues, but also the performance of the semi-active suspension system was enhanced in comparison to a passive damper system.

Chapter 6

Summary, Conclusions, and Suggestions for Future Work

6.1 Summary and Conclusion

In this thesis, the idea of developing control strategies for enhancing the operation of boost converters in different application areas was presented. The applications of boost converter in maximum power point tracking of photovoltaic modules, load current control, and regenerative suspension were studied for single phase, three phase, and continuous or discontinuous conduction. The key contributions of the present dissertation can be summarized as follows:

1. Analytical solution for boost converters in continuous and discontinuous conduction were investigated and used to develop controllers for shaping the input behavior of the converter. The results verify that the proposed controller can provide a resistive behavior between input current and voltage of the boost converter.

2. Novel maximum power point identification techniques for photovoltaic modules were presented and utilized in maximum power point tracking control. Implementation of the proposed technique indicated its high convergence speed and tracking efficiency.

3. Load current non-minimum phase behavior in boost converters was investigated and a nonlinear controller was developed to control the load current regardless of the conduction mode. This controller enables the circuit to be used in a wide range of power.

4. Control of three-phase bidirectional converter to achieve resistive behavior at the input terminals was studied and the developed controller was utilized in regenerative suspension to provide controllable damping coefficient and storing the vibration energy into the battery.

The outcomes of this dissertation provide mathematical framework for analyzing and controlling the behavior of converters based on their applications.

6.2 Suggestions for Future Research

Based on the experience gained and results obtained in the course of this research, the following activities may be considered for future work.

6.2.1 Integrating Boost and Buck Converters

In many cases of renewable energy sources, the source voltage varies based on the operating conditions. A novel DC/DC converter proposed in [126] can be used to switch the converter system to boost or buck, based on the input and output voltage values. This circuit is illustrated in Fig. 6.1 and can be operated in either buck, boost, or pass-through modes. The proposed control strategies in this work can be extended to this converter, to shape its input/output behavior based on the specific application. The result of this study can lead to a global solution for a power electronic device as an interface between energy source and the storage device while addressing the control goals.

6.2.2 Maximum Power Point Tracking Under Partial Shadowing Conditions

In this research, different MPPT methods ware proposed to operate a PV module at its MPP. However, in the case in which either a part of one module, or one or more modules in the string are shaded, the power-voltage characteristics of the PV module exhibits multiple local maxima [127]. Figure 6.2 demonstrates an example of this situation. Multiple local maxima would happen because of the existence of the bypass diode(s), and the current flow in them under partial shadowing situations. Previous works have addressed this issue using different control and MPPT strategies such as modified method of incremental conductance, sequential extremum seeking control, genetic algorithms, and particle swarm

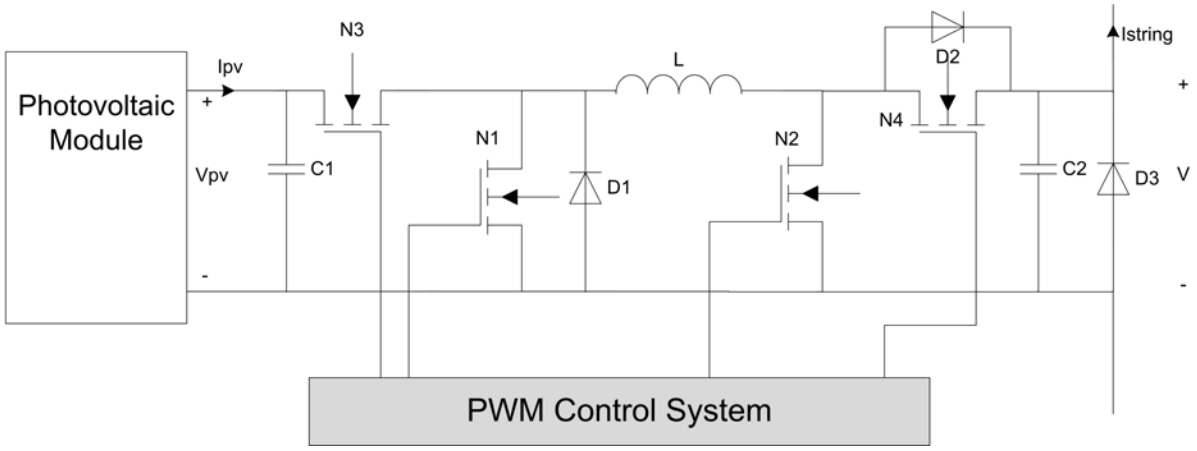

Figure 6.1: Schematics of the DC/DC converter proposed in [126].

optimization [128]-[134]. The real-time identification method and control approach proposed in this research can be extended to overcome the partial shadowing condition of PV modules.

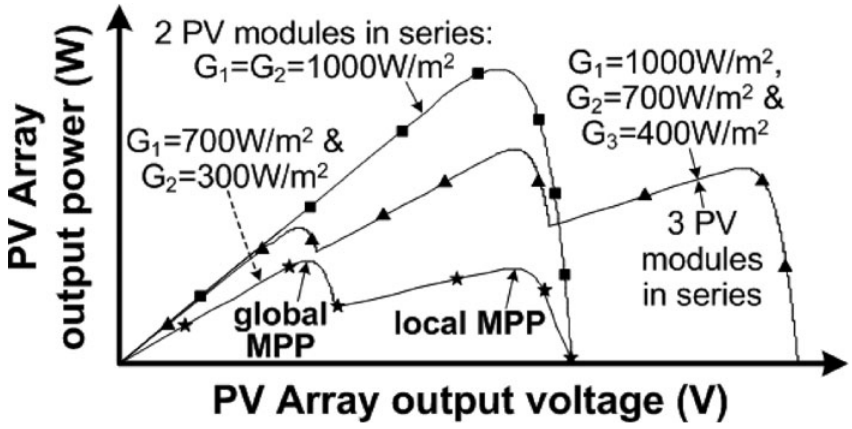

Figure 6.2: PV modules characteristics under different irradiations [127].

6.2.3 Maximum Power Point Tracking of Series Photovoltaic Modules utilizing Module Integrated Converters

Utilizing Module Integrated Converters (MIC) can benefit the control system to achieve autonomous, decoupled MPPT controllers for each PV module in an array, which results in improved robustness and reliability, while regulating the array voltage to a fixed value. This approach effectively decouples each PV module from the array, making the module

insensitive to changes in the array and allowing it to operate at its MPP. The schematic of this system is shown in Figure 6.3. In this figure, the DC-DC converter is modeled by a resistance at the input terminal, and a power transfer device at the output terminal [96]. Therefore, the relationship between the input and output can be written as

$$V_{Pi}I_{Pi} = \eta V_{oi}I_{oi}, \quad i = 1, 2, ..., n \tag{6.1}$$

where η is the converter's power transfer efficiency rate and

$$0 \leq \eta \leq 1 \tag{6.2}$$

Integrating the results of sections 6.2.1 and 6.2.2, and the real time identification and control strategies proposed in this dissertation, the operating conditions of series PV modules can be identified and the modules can be operated in different modes based on their characteristics curves. Finding the optimal operating point for each module, individually, and the whole system together, along with the distributed control strategy is an interesting topic for future research.

6.2.4 Battery Management System Design

In this research, we did not study battery management circuitry and controllers. Pulsating current waveforms at the input terminals of the storage device can affect the battery lifetime, extensively. A battery management strategy is needed to extend the battery lifetime by controlling the charging rate and providing protection against overcharge, while taking care of high frequency changes of the battery current.

6.2.5 Active Suspension System Utilizing 3-Phase Bidirectional Converter

In this research a bidirectional boost converter was utilized and controlled to provide desired damping for the regenerative suspension systems, while retrieving the damped energy in the energy storage element. The bidirectional converter can be also utilized as an active suspension system, where both damping and stiffness characteristics of the system can be controlled. This system allows the suspension system designers to achieve higher levels of ride quality and car handling, while saving vibration energy and releasing it whenever needed.

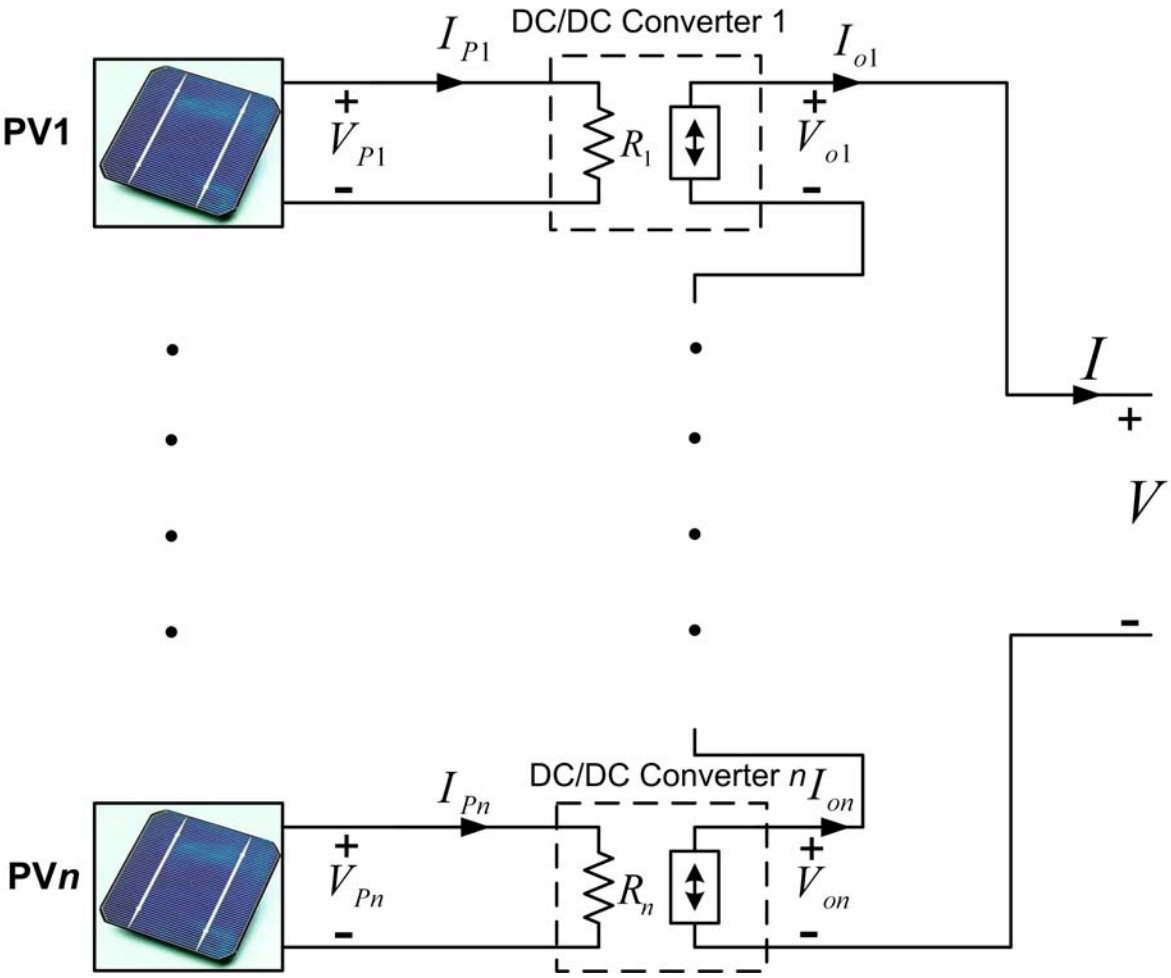

Figure 6.3: Series PV modules with module integrated converters.

Bibliography

[1] C. A. Sanchez, "*Control Design for Electronic Power Converters*", Ph.D. Thesis, Universite De Grenoble, Nov. 2010.

[2] P. Das, M. Pahlevaninezhad, J. Drobnik, G. Moschopoulos, and P. K. Jain, "A Nonlinear Controller Based on a Discrete Energy Function for an AC/DC Boost PFC Converter," *IEEE Transactions on Power Electronics,* Vol. 28, No. 12, pp. 5458s-5476, Dec. 2034.

[3] Y. X. Wang, D. H. Yu, and Y. B. Kim, "Robust Time-Delay Control for the DC-DC Boost Converter," *IEEE Transactions on Industrial Electronics,* Vol. 61, No. 9, pp. 4829-4837, Sept. 2014.

[4] G. W. Wester and R. D. Middlebrook, "Low-Frequency Characterization of Switched dc-dc Converters," *IEEE Transactions on Aerospace and Electronic Systems,* Vol. 9, No. 3, pp. 376-385, May 1973.

[5] T. S. Hwang and S. Y. Park, "Seamless Boost Converter Control Under the Critical Boundary Condition for a Fuel Cell Power Conditioning System," *IEEE Transactions on Power Electronics,* Vol. 27, No. 8, pp. 3616-3626, 2012.

[6] S. Kapat, A. Patra, and S. banerjee, "A Novel Current Controlled Tri-State Boost Converter With Superior Dynamic Performance," *IEEE International Symposium on Circuits and Systems,* May 2008, Seattle, WA, US.

[7] Y. Li and Z. Ji, "An Approach on T-S Fuzzy Model and Control of Buck-boost Converter," *7th World Congress on Intelligent Control and Automation,* June 2008, Chongqing, China.

[8] M. Maldonado, R. Salas-Cabrera, J. C. Rosas-Caro, and J. De Leon-Morales, "Modeling and Control of a DC-DC Multilevel Boost Converter," *IET Power Electronics,* Vol. 4, Iss. 6, pp. 693-700, 2011.

[9] Y. F. Li, M. F. Tsai, C. S. Tseng, and Y. F. Chiang, "Model Reference Adaptive Control Design for the Buck-Boost Converter," *38th Annual Conference on IEEE Industrial Electronics Society (IECON),* October 2012, Montreal, Canada.

[10] C. Yao, X. Ruan, W. Cao, and P. Chen, "A Two-Mode Control Scheme With Input Voltage Feed-Forward for the Two-Switch Buck-Boost DC-DC Converter," *IEEE Transactions on Power Electronics,* Vol. 29, No. 4, pp. 2037-2048, 2014.

[11] R. J. Wai and L. C. Shih, "Adaptive Fuzzy-Neural-Network Design for Voltage Tracking Control of a DC-DC Boost Converter," *IEEE Transactions on Power Electronics,* Vol. 27, No. 4, pp. 2104-2115, 2012.

[12] C. Restrepo, T. Konjedic, J. Calvente, M. Milanovic, and R. Giral, "Fast Transitions Between Current Control Loops of the Coupled-Inductor Buck-Boost DC-DC Switching Converter," *IEEE Transactions on Power Electronics,* Vol. 28, No. 8, pp. 3648-3652, 2013.

[13] W. Ma, M. Wang, S. Liu, S. Li, and P. Yu, "Stabilizing the Average-Current-Mode-Controlled Boost PFC Converter via Washout-Filter-Aided Method," *IEEE Transactions on Circuits and Systems – II: Express Briefs,* Vol. 58, No. 9, pp. 595-599, 2011.

[14] K. D. Gusseme, D. M. Van de Sype, A. P. M. Van den Bossche, and J. A. Melkebeek, "Input-Current distortion of CCM boost PFC converters operated in DCM," *IEEE Transactions on Industrial Electronics,* Vol. 54, No. 2, pp. 858-865, 2007.

[15] K. I. Hwu and Y. T. Yau, "High step-up converter based on charge pump and boost converter," *IEEE Transactions on Power Electronics,* Vol. 27, No. 5, pp. 2484-2494, 2012.

[16] G. Petrone, G. Spagnuolo, and M. Vitelli, "An Analog Technique for Distributed MPPT PV Applications," *IEEE Transactions on Industrial Electronics,* Vol. 59, No. 12, pp. 4713-4722, 2012.

[17] A. Al Nabulsi and R. Dhaouadi, "Efficiency Optimization of a DSP-Based Standalone PV System Using Fuzzy Logic and Dual-MPPT Control," *IEEE Transactions on Industrial Informatics,* Vol. 8, No. 3, pp. 573-584, 2012.

[18] K. Ishaque, Z. Salam, M. Amjad, and S. Mekhilef, "An Improved Particle Swarm Optimization (PSO)-Based MPPT for PV With Reduced Steady-State Oscillation," *IEEE Transactions on Power Electronics,* Vol. 27, No. 8, pp. 3627-3638, 2012.

[19] E. Mamarelis, G. Petrone, and G. Spagnuolo, "Design of a Sliding-Mode-Controlled SEPIC for PV MPPT Applications," *IEEE Transactions on Industrial Electronics,* Vol. 61, No. 7, pp. 3387-3398, 2014.

[20] D. Sera, L. Mathe, T. Kerekes, S. V. Spataru, and R. Teodorescu, "On the Perturb-and-Observe and Incremental Conductance MPPT Methods for PV Systems," *IEEE Journal on Photovoltaics,* Vol. 3, No. 3, pp. 1070-1078, 2013.

[21] N. Mutoh, M. Ohno, and T. Inoue, "A Method for MPPT Control While Searching for Parameters Corresponding to Weather Conditions for PV Generation Systems," *IEEE Transactions on Industrial Electronics,* Vol. 53, No. 4, pp. 1055-1065, 2006.

[22] M. A. G. de Brito, L. Galotto, L. P. Sampaio, G. A. Melo, and C. A. Canesin, "Evaluation of the Main MPPT Techniques for Photovoltaic Applications," *IEEE Transactions on Industrial Electronics,* Vol. 60, No. 3, pp. 1156-1167, 2013.

[23] W. D. Jones, "Easy Ride: Bose Corp. Uses Speaker Technology to Give Cars Adaptive Suspension," *IEEE Spectrum,* Vol. 42, No. 5, pp. 12-14, 2005.

[24] S. B. Choi, M. S. Seong, and K. S. Kim, "Vibration Control of an Electrorheological Fluid-Based Suspension System with an Energy Regenerative Mechanism," *Journal of Automobile Engineering,* Vol. 223, Part. D, pp. 459-469, 2009.

[25] J. Zhang, H. Zeng, and T. Jiang, "A primary-side control scheme for high-power-factor LED driver with TRIAC dimming capability," *IEEE Transactions on Power Electronics,* Vol. 27, No. 11, pp. 4619-4629, 2012.

[26] Y. Li, K. R. Vannorsdel, A. J. Zirger, M. Norris, and D. Maksimovic, "Current Mode Control for Boost Converters With Constant Power Loads," *IEEE Transactions on Circuits and Systems–I: Regular Papers,* Vol. 59, No. 1, pp. 198-206, 2012.

[27] K. Raggl, T. Nussbaumer, G. Doerig, J. Biela, and J. W. Kolar, "Comprehensive Design and Optimization of a High-Power-Density Single-Phase Boost PFC," *IEEE Transactions on Industrial Electronics*, Vol. 56, No. 7, pp. 2574-2587, July 2009.

[28] N. Vazquez, J. Lopez, J. Doerig, J. Arau, C. Hernandez, and E. Rodriguez, "A Different Approach to Implement an Active Current Shaper," *IEEE Transactions on Industrial Electronics*, Vol. 52, No. 1, pp. 132-138, February 2005.

[29] Y. M. Liu, and L. K. Chang, "Single-Stage Soft-Switching AC-DC Converter with Input-Current Shaping for Universal Line Applications," *IEEE Transactions on Industrial Electronics*, Vol. 56, No. 2, pp. 467-479, February 2009.

[30] M. Narimani, and G. Moschopoulos, "A New Single-Phase Single-Stage Three-Level Power Factor Correction AC-DC Converter with Phase-Shift Modulation," *IEEE Transactions on Industrial Electronics*, Vol. 60, No. 9, pp. 3731-3735, Sept. 2013.

[31] M. Narimani, and G. Moschopoulos, "A Three-Level Integrated AC-DC Converter," *IEEE Transactions on Power Electronics*, Vol. 29, No. 4, pp. 1813-1820, April 2014.

[32] D. S. Wijeratne, and G. Moschopoulos, "A Novel Three-Phase Buck-Boost AC-DC Converter," *IEEE Transactions on Power Electronics*, Vol. 29, No. 3, pp. 1331-1343, March 2014.

[33] F. Zhang, and J. Xu, "A Novel PCCM Boost PFC Converter with Fast Dynamic Response," *IEEE Transactions on Industrial Electronics*, Vol. 58, No. 9, pp. 4207-4216, September 2011.

[34] R. Martinez, and P. N. Enjeti, "A High-Performance Single-Phase Rectifier with Input Power Factor Correction," *IEEE Transactions on Power Electronics*, Vol. 11, No. 2, pp. 311-317, March 1996.

[35] C. Sreekumar, and V. Agrawal, "Comparison of Mode Switched Controllers for a Pseudo Continuous Current Mode Boost Converter," *IEEE International Conference on Power Electronics, Drivers, and Energy Systems (PEDES 2006)*, December 2006, New Delhi, India.

[36] M. M. Jovanovic, and Y. Jang, "State-of-the-Art, Single-Phase, Active Power-Factor-Correction Techniques for High-Power Applications–An Overview," *IEEE Transactions on Industrial Electronics*, Vol. 52, No. 3, pp. 701-708, June 2005.

[37] C. P. Ku, D. Chen, and S. H. Lin, "A New Control Scheme for Boost PFC Converters for Both CCM and DCM Operations," *Proceedings of 2011 IEEE Energy Conversion Congress and Exposition (ECCE)*, September 2011, pp. 1334-1338, Phoenix, AZ, US.

[38] K. D. Gusseme, D. M. Van de Sype, A. P. M. Van den Bossche, and J. A. Melkebeek, "Digitally Controlled Boost Power-Factor Correction Converter Operating in Both Continuous and Discontinuous Conduction Mode," *IEEE Transactions on Industrial Electronics*, Vol. 52, No. 1, pp. 88-99, February 2005.

[39] S. F. Lim, and A. M. Khambadkone, "A Simple Digital DCM Control Scheme for Boost PFC Operating in Both CCM and DCM," *IEEE Transactions on Industry Applications*, Vol. 47, No. 4, pp. 1802-1812, July/August 2011.

[40] Y. M. Roshan and M. Moallem, "Dynamic Analysis and Load Current Control of Boost Converters using Output Redefinition," *IEEE Transactions on Power Electronics*, Vol. 29, No. 9, pp. 5054-5062, September 2014.

[41] Y. M. Roshan and M. Moallem, "Maximum Power Point Estimation and Tracking Using Power Converter Input Resistance Control," *Journal of Solar Energy*, No. 96, pp. 177-186, 2013.

[42] Y. M. Roshan and M. Moallem, "Load Current Control of a Boost Converter using Output Redefinition," *39th Annual Conference on the IEEE Industrial Control Society*, Vienna, Austria, October 2013.

[43] R. Kadri, J. P. Gaubert and G. Champenois, "An Improved Maximum Power Point Tracking for Photovoltaic Grid-Connected Inverter Based on Voltage-Oriented Control," *IEEE Transactions on Industrial Electronics*, Vol. 58, No. 1, pp. 66-75, January 2011.

[44] T. Esram and P. L. Chapman, "Comparison of Photovoltaic Array Maximum Power Point Tracking Techniques," *IEEE Transactions on Energy Conversion*, Vol. 22, No. 2, pp. 66-75, June 2007.

[45] S. Chun and A. Kwasinski, "Analysis of Classical Root-Finding Methods Applied to Digital Maximum Power Point Tracking for Sustainable Photovoltaic Energy Generation," *IEEE Transactions on Power Electronics*, Vol. 26, No. 12, pp. 3730-3743, December 2011.

[46] W. M. Lin, C. M. Hong, and C. H. Chen, "Neural-Network-Based MPPT Control of a Stand-Alone Hybrid Power Generation System," *IEEE Transactions on Power Electronics*, Vol. 26, No. 12, pp. 3571-3581, December 2011.

[47] G. W. Hart, H. M. Branz, and C. H. Cox, "Experimental Tests of Open-Loop Maximum-Power-Point Tracking Techniques," *Solar Cells*, Vol. 13, Iss. 2, pp. 185-195, December 1984.

[48] M. A. S. Masoum, H. Dehbonei, and E. F. Fuchs, "Theoretical and Experimental Analysis of Photovoltaic Systems with Voltage and Current Based Maximum Power-Point Tracking," *IEEE Transactions on Energy Conversion*, Vol. 17, No. 4, pp. 514-522, December 2002.

[49] Y. M. Roshan and M. Moallem, "Maximum Power Point Tracking Using Boost Converter Input Resistance Control," *21st IEEE International Symposium on Industrial Electronics*, Hangzhou, China, 2012.

[50] B. Bekker and H. J. Beukes, "Finding an Optimal PV Panel Maximum Power Point Tracking Method," *7th AFRICON Conference in Africa*, pp. 1125-1129, Botswana, 2004.

[51] O. Wasynczuk, "Dynamic Behavior of a Class of Photovoltaic Power Systems," *IEEE Transactions on Power Apparatus and Systems*, Vol. 10, Iss. 9, pp. 3031-3037, September 1983.

[52] A. K. Abdelsalam, A. M. Massoud, S. Ahmed, and P. N. Enjeti, "High-Performance Adaptive Perturb and Observe MPPT Technique for Photovoltaic-Based Microgrids," *IEEE Transactions on Power Electronics*, Vol. 26, No. 4, pp. 1010-1021, April 2011.

[53] W. Xiao and W. G. Dunford, "A Modified Adaptive Hill Climbing MPPT Method for Photovoltaic Power Systems," *35th Annual IEEE Power Electronics Specialists Conference*, Aachen, Germany, 2004.

[54] E. Koutroulis, K. Kalaitzakis, and N. C. Voulgaris, "Development of a Microcontroller-Based Photovoltaic Maximum Power Point Tracking Control System," *IEEE Transactions on Power Electronics*, Vol. 16, No. 1, pp. 46-54, January 2001.

[55] Y. M. Roshan and M. Moallem, "Maximum Power Point Tracking Control Using Resistive Input Behavior of the Power Converter," *37th Annual IEEE Photovoltaic Specialists Conference*, Seattle, USA, 2011.

[56] D. Menniti, A. Burgio, N. Sorrentino, A. Pinnarelli, and G. Brusco, "An Incremental Conductance Method with Variable Step Size for MPPT: Design and Implementation," *10th International Conference on Electrical Power Quality and Utilization*, Lodz, Poland, September 2009.

[57] T. Hiyama, S. Kouzuma, and T. Imakubo, "Identification of Optimal Operating Point of PV Modules Using Neural Network for Real Time Maximum Power Tracking Control," *IEEE Transactions on Energy Conversion*, Vol. 10, Iss. 2, pp. 360-367, June 1995.

[58] C. Y. Won, D. H. Kim, S. C. Kim, W. S. Kim, and H. S. Kim, "A New Maximum Power Point Tracker of Photovoltaic Arrays Using Fuzzy Controller," *25th Annual IEEE Power Electronic Specialists Conference (PESC)*, Taipei, Taiwan, 1994.

[59] A. Unger, F. Schimmack, B. Lohmann, and R. Schwarz, "Application of LQ-Based Semi-Active Suspension Control in a Vehicle," *Control Engineering Practice*, Article in Press, 2013.

[60] M. S. Fallah, R. B. Bhat, and W. F. Xie, "Optimized Control of Semiactive Suspension Systems Using H_∞ Robust Control Theory and Current Signal Estimation," *IEEE/ASME Transactions on Mechatronics*, Vol. 17, No. 4, pp. 767-778, 2012.

[61] M. Canale, M. Milanese, and C. Novara, "Semi-Active Suspension Control Using "Fast" Model-Predictive Techniques," *IEEE Transactions on Control Systems Technology*, Vol. 14, No. 6, pp. 1034-1046, 2006.

[62] Y. Liu, T. P. Waters, and M. J. Brennan, "A Comparison of Semi-Active Damping Control Strategies for Vibration Isolation of Harmonic Disturbances," *Journal of Sound and Vibration*, Vol. 280, pp. 21-39, 2005.

[63] M. Zapateiro, F. Pozo, H. R. Karimi, and N. Luo, "Semiactive Control Methodologies for Suspension Control with Magnetotheological Dampers," *IEEE/ASME Transactions on Mechatronics*, Vol. 17, No. 2, pp. 370-380, 2012.

[64] V. Sankaranarayanan, M. E. Emekli, B. A. Guvenc, L. Guvenc, E. S. Ozturk, S. S. Ersolmaz, I. E. Eyol, and M. Sinal, "Semiactive Suspension Control of a Light Commercial Vehicle," *IEEE Transactions on Mechatronics*, Vol. 13, No. 5, pp. 598-604, 2008.

[65] X. Song, "*Design of Adaptive Vibration Control Systems with Application of Magneto-Rheological Dampers*," Doctoral Dissertation submitted to Virginia Polytechnic Institute and State University, Virginia, USA, February 1999.

[66] J. Prudell, M. Stoddard, E. Amon, T. K. A. Brekken, and A. von Jouanne, "A Permanent-Magnet Tubular Linear Generator for Ocean Wave Energy Conversion," *IEEE Transactions on Industrial Applications*, Vol. 46, No. 6, pp. 2392-2400, 2010.

[67] R. Caponetto, O. Diamante, G. Fargione, A. Risitano, and D. Tringali, "A Soft Computing Approach to Fuzzy Sky-Hook Control of Semiactive Suspension," *IEEE Transactions on Control Systems Technology*, Vol. 11, No. 6, pp. 786-798, 2003.

[68] K. S. Hong, H. C. Sohn, and J. K. Hedrick, "Modified Skyhook Control of Semi-Active Suspensions: A New Model, Gain Scheduling, and Hardware-in-the-Loop Tuning," *ASME Journal of Dynamic Systems, Measurement, and Control*, Vol. 124, pp. 158-167, 2002.

[69] I. Martins, J. Esteves, G. D. Marques, and F. P. da Silva, "Permanent-Magnets Linear Actuators Applicability in Automobile Active Suspensions," *IEEE Transactions on Vehicular Technology*, Vol. 55, No. 1, pp. 86-94, 2006.

[70] J. J. H. Paulides, L. Encica, E. A. Lomonova, and A. J. A. Vandenput, "Active Roll Compensation for Automotive Applications Using a Brushless Direct-Drive Linear Permanent Magnet Actuator," *37th IEEE Power Electronics Specialists Conference*, Jeju, South Korea, June 2006.

[71] S. S. Kim, and Y. Okada, "Variable Resistance Type Energy Regenerative Damper Using Pulse Width Modulated Step-Up Chopper," *ASME Journal of Vibration and Acoustics*, Vol. 124, Issue 1, pp. 110-115, 2002.

[72] R. Sabzehgar, A. Maravandi and M. Moallem, "Energy Regenerative Suspension Using an Algebraic Screw Linkage Mechanism," *IEEE/ASME Transactions on Mechatronics*, Early Access, 2014.

[73] Z. Chen, W. Gao, J. Hu, and X. Ye, "Closed-Loop Analysis and Cascade Control of a Nonminimum Phase Boost Converter," *IEEE Transactions on Power Electronics,* Vol. 26, No. 4, pp. 1237-1252, 2011.

[74] S. Gopalswamy and J. K. Hedrick, "Tracking Non-Linear Non-Minimum Phase Systems Using Sliding Control," *International Journal of Control,* Vol. 57, pp. 1141-1158, 1993.

[75] F. Zhang and J. Xu, "A Novel PCCM Boost PFC Converter with Fast Dynamic Response," *IEEE Transactions on Industrial Electronics,* Vol. 58, No. 9, pp. 4207-4216, 2011.

[76] Y. I. Son and I. H. Kim, "Complementary PID Controller to Passivity-Based Nonlinear Control of Boost Converters with Inductor Resistance," *IEEE Transactions on Control Systems Technology,* Vol. 20, No. 3, pp. 826-834, 2012.

[77] D. M. Sable, B. H. Cho, and R. B. Ridley, "Use of Leading-Edge Modulation to Transform Boost and Flyback Converters into Minimum-Phase-Zero Systems," *IEEE Transactions on Power Electronics,* Vol. 6, No. 4, pp. 704-711, 1991.

[78] K. I. Hwu and T. J. Peng, "A Novel Buck-Boost Converter Combining KY and Buck Converters," *IEEE Transactions on Power Electronics,* Vol. 27, No. 5, pp. 2236-2241, 2012.

[79] H. H. Huang, C. L. Chen, D. R. Wu, and K. H. Chen, "Solid-Duty-Control Technique for Alleviating the Right-Half-Plane Zero Effect in Continuous Conduction Mode Boost Converters," *IEEE Transactions on Power Electronics,* Vol. 27, No. 1, pp. 354-361, 2012.

[80] A. Isidori, "*Nonlinear Control Systems,*" Springer, Third Edition, London, 1995.

[81] A. Isidori, "*Nonlinear Control Systems II,*" London, 1999.

[82] S. Kapat, A. Patra, and S. Banerjee, "A Current-Controlled Tristate Boost Converter with Improved Performance Through RHP Zero Elimination," *IEEE Transactions on Power Electronics,* Vol. 24, No. 3, pp. 776-786, 2009.

[83] R. Naim, G. Weiss, and S. Ben-Yaakov, "H_∞ Control Applied to Boost Power Converters," *IEEE Transactions on Power Electronics,* Vol. 12, No. 4, pp. 677-683, 1993.

[84] R. Giral and L. Martinez-Salamero, "Sliding-Mode Control of Interleaved Boost Converters," *IEEE Transactions on Circuits Systems I,* Vol. 47, No. 9, pp. 1330-1339, 2000.

[85] E. Santi, A. Monti, D. H. Li, K. Proddutur, and R. A. Dougal, "Synergetic Control for DC-DC Boost Converter: Implementation Options," *IEEE Transactions on Industry Applications,* Vol. 39, No. 6, pp. 1803-1813, 2003.

[86] M. Moallem, R. V. Patel, and K. Khorasani, "Nonlinear Tip-Position Tracking Control of a Flexible-Link Manipulator: Theory and Experiments," *Automatica,* Vol. 37, Issue 11, pp. 1825-1834, 2001.

[87] A. Bazaei and M. Moallem, "Improving Force Control Bandwidth of Flexible-Link Arms Through Output Re-Definition," *IEEE/ASME Transactions on Mechatronics,* Vol. 16, No. 2, pp. 380-386, 2011.

[88] M. Malekzadeh, A. Naghash, and H. A. Talebi, "A Robust Nonlinear Control Approach for Tip Position Tracking of Flexible Spacecraft," *IEEE Transactions on Aerospace and Electronic Systems,* Vol. 47, No. 4, pp. 2423-2434, 2011.

[89] Y. M. Roshan and M. Moallem, "Control of a Boost Converter for Resistive Input Behavior in the Continuous Conduction Mode ," *38th Annual Conference of the IEEE Industrial Control Society,* Montreal, Canada, 2012.

[90] Y. M. Roshan and M. Moallem, "Maximum Power Point Tracking Using Boost Converter Input Resistance Control by Means of Lambert W-Function," *3rd IEEE International Symposium on Power Electronics for Distributed Generation Systems,* Aalborg, Denmark, 2012.

[91] Y. M. Roshan, A. Maravandi, and M. Moallem, "Energy Regenerative Suspension System Using 3-Phase Bidirectional Converter Control and a Linear-to-Rotary Conversion Mechanism," *IEEE Transactions on Industrial Electronics,* Submitted, 2014.

[92] Y. M. Roshan and M. Moallem, "Control of a Regenerative Suspension System Utilizing a Three-Phase Bidirectional Converter," *40th Annual Conference on the IEEE Industrial Control Society,* Submitted, Texas, US, 2014.

[93] P. Tricoli, "Analytical Closed-Form Solution for Transient Analysis of Boost DC-DC Converters," *The International Journal for Computation and Mathematics in Electrical Engineering*, Vol. 30, No. 2, 2011.

[94] C. J. Zhan, X. G. Wu,S. Kromlidis, V. K. Ramachandaramurthy, M. Barnes, N. Jenkins, and A. J. Ruddell,, "Two Electrical Models of the Lead-Acid Battery Used in a Dynamic Voltage Restorer," *IEEE Proceedings of Generation, Transmission and Distrbutionn*, Vol. 150, Issue 2, pp. 175-182, 2003.

[95] R. Sabzehgar, and M. Moallem, "Modeling and Control of a Boost Converter for Pseudo-Resistive Input Behavior," *IET Conference on Renewable Power Generation*, Edinburgh, UK, 2011

[96] R. W. Erickson, "*Fundamentals of Power Electronics*", Chapman and Hall, New York, 1997.

[97] R. Sabzehgar and M. Moallem,"A Boost-Type Power Converter for Energy-Regenerative Damping," *IEEE/ASME Transactions on Mechatronics*, Vol. 18, Iss. 2, pp. 725-732, 2013.

[98] L. Castaner and S. Silvestre, "*Modeling Photovoltaic Systems Using PSpice*", John Wiley & Sons Ltd., England, 2002.

[99] L. Zhou, Y. Chen, K. Kou, and F. Jia,"New Approach for MPP Control of Photovoltaic System with Mutative-Scale Dual-Carrier Chaotic Search," *IEEE Transactions on Power Electronics*, Vol. 26, No. 4, pp. 1038-1048, 2011.

[100] Y. Chang and C. Chang, "A Maximum Power Point Tracking of PV System by Scaling Fuzzy Control," *Proceedings of the International Multi-Conference of Engineers and Computer Scientists*, Vol. 2, Hong Kong, March 2010.

[101] F. Liu, S. Duan, F. Liu, B. Liu and Y. Kong, "A Variable Step Size INC MPPT Method for PV Systems," *IEEE Transactions on Industrial Electronics*, Vol. 55, No. 7, pp. 2622-2628, July 2008.

[102] C. C. Chu and C. L. Chen, "Robust Maximum Power Point Tracking Method for Photovoltaic Cells: A Sliding Mode Control Approach," *Solar Energy*, Vol. 83, pp. 1370-1378, 2009.

[103] Q. Mei, M. Shan, L. Liu, and J. M. Guerrero, "A Novel Improved Variable Step-Size Incremental Resistance (INR) MPPT Method for PV Systems," *IEEE Transactions on Industrial Electronics*, Vol. 58, No. 6, pp. 2427-2434, June 2011.

[104] C. S. Chiu,"T-S Fuzzy Maximum Power Point Tracking Control of Solar Power Generation Systems," *IEEE Transactions on Energy Conversion*, Vol. 25, No. 4, pp. 1123-1132, December 2010.

[105] A. Chatterjee, A. Keyhani, and D. Kapoor, "Identification of Photovoltaic Source Models," *IEEE Transactions on Energy Conversion*, Vol. 26, No. 3, pp. 883-889, 2011.

[106] A. Abete, F. Scapino, F. Spertino, and R. Tommasini, "Aging Effect on the Performance of A-SI Photovoltaic Modules in a Grid Connected System: Experimental Data and Simulation Results," *IEEE Photovoltaic Specialists Conference*, Anchorage, USA, 2000.

[107] G. Petrone, G. Spagnoulo, and M. Vitelli, "Analytical Model of Mismatched Photovoltaic Fields by Means of Lambert W-Function," *Solar Energy Materials and Solar Cells*, Vol. 91, Issue 18, pp. 1652-1657, 2007.

[108] J. A. Gow, and C. D. Manning, "Development of a Photovoltaic Array Model for Use in Power-Electronics Simulation Studies," *Proceeding of IEE Electric Power Applications*, Vol. 146, Issue 2, pp. 193-200, 1999.

[109] A. Garrigos, J. M. Blanes, J. A. Carrasco, and J. B. Ejea, "Real Time Estimation of Photovoltaic Modules Characteristics and Its Application to Maximum Power Point Operation," *Renewable Energy*, Vol. 32, pp. 1059- 1076, 2007.

[110] F. J. Toledo, J. M. Blanes, A. Garrigos, and J. A. Martinez, "Analytical Resolution of the Electrical Four-Parameters Model of a Photovoltaic Module Using Small Perturbation Around the Operating Point," *Renewable Energy*, Vol. 43, pp. 83-89, 2012.

[111] B. N. Alajmi, K. H. Ahmed, S. J. Finney, and B. W. Williams, "Fuzzy-Logic-Control Approach of a Modified Hill-Climbing Method for Maximum Power Point in Microgrid Standalone Photovoltaic System," *IEEE Transactions on Power Electronics*, Vol. 26, No. 4, pp. 1022-1030, April 2011.

[112] F. Liu, S. Duan, F. Liu, B. Lie, and Y. Kang, "A Variable Step Size INC MPPT Method for PV Systems," *IEEE Transactions on Industrial Electronics*, Vol. 55, No. 7, pp. 2622-2628, July 2008.

[113] Q. Mei, M. Shan, L. Liu, and J. M. Guerrero, "A Novel Improved Variable Step-Size Incremental-Resistance MPPT Method for PV Systems," *IEEE Transactions on Industrial Electronics*, Vol. 58, No. 6, pp. 2427-2434, June 2011.

[114] T. Tafticht, K. Agbossou, M. L. Doumbia, and A. Cheritin, "An Improved Maximum Power Point Tracking Method for Photovoltaic Systems," *Renewable Energy*, Vol. 33, pp. 1508-1516, 2008.

[115] C. S. Chiu, "T-S Fuzzy Maximum Power Point Tracking Control of Solar Power generation Systems," *IEEE Transactions on Energy Conversion*, Vol. 25, No. 4, pp. 1123-1132, December 2010.

[116] Marian. K. Kazimierczuk, "*Pulse-Width Modulated DC-DC Power Converters,*" Wiley and Sons, LTD, UK, 2008.

[117] C. I. Byrnes and A. Isidori, "Output Regulation for Nonlinear Systems: An Overview," *Proceedings of the 37th COnference on Decision & Control,* Tampa, FL, 1998.

[118] H. Sira-Ramirez, "Sliding Regimes in General Non-Linear Systems: A Relative Degree Approach," *International Journal of Control,* Vol. 50, No. 4, pp. 1487-1506, 1989.

[119] Y. Shtessel, S. Baev, and H. Biglari, "Unity Power Factor Control in 3-phase AC/DC boost converter using Sliding Modes," *IEEE Transactions on Industrial Electronics*, Vol. 55, No. 11, pp. 3874-3882, 2008.

[120] J. F. Gieras, Z. J. Piech, B. Tomczuk, "*Linear Synchronous Motors*," CRC Press, New York, 2nd edition, 2011.

[121] E. Guglielmino, T. Sireteanu, C. W. Stammers, G. Ghita, and M. Giuclea, "*Semi-active Suspension Control*," Springer, London, 2008.

[122] L. Segal, and L. Xiao-Pei, "Vehicular Resistance to Motion as Influenced by Road Roughness and Highway Alignment," *Australian Road Research*, Vol. 12, No. 4, pp. 211-222, 1982.

[123] M. G. Fodor, and R. Redfield, "The Variable Linear Transmission for Regenerative Damping in Vehicle Suspension Control," *Vehicle System Dynamics*, Vol. 22, pp. 1-20, 1993.

[124] A. Maravandi and M. Moallem, "Regenerative Shock Absorber using a Two-Leg Motion Conversion Mechanism," *IEEE/ASME Transactions on Mechatronics*, Submitted, 2014.

[125] S. J. Chapman, "*Electric Machinery Fundamentals*," Fourth Second Edition, McGrawHill, 2005.

[126] L. Linares, R. W. Erickson, S. MacAlpine, and M. Brandemuehl, "Improved Energy Capture in Series String Photovoltaics via Smart Distributed Power Electronics," *Applied Power Electronics Conference and Exposition (APEC)*, Washington, US, 2009.

[127] E. Koutroulis and F. Blaabjerg, "A New Technique for Tracking the Global Maximum Power Point of PV Arrays Operating Under Partial-Shading Conditions," *IEEE Journal of Photovoltaics*, Vol. 2, No. 2, pp. 184-191, April 2012.

[128] L. Gao, R. A. Dougal, S. Liu,and A. Lotova, "Parallel-Connected Solar PV System to Address Partial and Rapidly Fluctuating Shadow Conditions," *IEEE Transactions on Industrial Electronics*, Vol. 56, No. 5, pp. 1548-1556, May 2009.

[129] H. Patel and V. Agarwal, "Maximum Power Point Tracking Scheme for PV Systems Operating Under Partially Shaded Conditions," *IEEE Transactions on Industrial Electronics*, Vol. 55, Iss. 4, pp. 1689-1698, April 2008.

[130] Y. H. Ji, D. Y. Jung, J. G. Kim, T. W. Lee, and C. Y. Won, "A Real Maximum Power Point Tracking Method for Mismatching Compensation in PV Array Under Partially Shaded Conditions," *IEEE Transactions on Power Electronics*, Vol. 26, No. 4, pp. 1001-1010, April 2011.

[131] P. Lei, Y. Li, and J. E. Seem, "Sequential ESC-Based Global MPPT Control for Photovoltaic Array with Variable Shading," *IEEE Transactions on Sustainable Energy*, Vol. 2, Iss. 3, pp. 348-358, July 2011.

[132] M. Miyatake, M. Veerachary, F. Toriumu, N. Fujii, and H. Ko, "Maximum Power Point Tracking of Multiple Photovoltaic Arrays: A PSO Approach," *IEEE Transactions on Aerospace Electronic Systems*, Vol. 47, No. 1, pp. 367-380, January 2011.

[133] K. Odagaki, Y. Li, and J. E. Seem, "Practical Study on 5.2 MWPV System in Sharp's Kameyama Plant," *Power Conversion Conference*, Nagoya, Japan, 2007.

[134] H. Taheri, Z. Salam, K. Ishaque, and Syafaruddin, "A Novel Maximum Power Point Tracking Control of Photovoltaic System Under Partial and Rapidly Fluctuating Shadow Conditions Using Differential Evolution," *IEEE Symposium on Industrial Electronic & Applications (ISIEA)*, Penang, Malaysia, October 2010.